eXPRESS Polymer Letters Vol.1, No.5 (2007) 252
Available online at www.expresspolymlett.com
DOI: 10.3144/expresspolymlett.2007.38

Editorial corner – a personal view

Emerging nanostructured polymeric materials

J. Seppälä[*]

Department of Chemical Technology, Helsinki University of Technology, P.O. Box 6100, FI-02015 TKK, Finland

In polymer science and technology just the control of molecular weight and composition is not enough. In addition, and simultaneously, molecular weight distributions, compositional distributions, stereo structures and interactions between molecules need to be understood and controlled. The overall control of these various parameters offers tremendous possibilities in materials science and engineering. Nature is master in synthesizing specific polymers and tailoring their properties. Weak interactions between polymeric molecules and organised structures can produce complicated functionalities in natural polymers. In the field of synthetic polymers we still have huge potential ahead to study and make usable.

The control of materials structures in different hierarchical levels is of prime importance in nanomaterials. The length of a covalent bond is around 0.1nm which means that polymerization catalysts can be considered as 'nanoplants' with a diameter of around one nanometre, thicknesses of polymer crystalline lamellas are typically some tens of nanometres, lengths of polymeric molecules are in the range of tens or hundreds of nanometres or more.

The concept of nanotechnology in polymers can comprise the production of controlled nanostructures on the materials surface, of large specific surface areas through production of nanofibers and nanosize porous structures, of in nano level organised supramolecular structures through self assembling, and of nanocomposites by combining nanoparticles and nanofibers with polymeric matrices.

In aiming to tailor materials properties on every level, the control of the structures should start already in the synthesis stage. Here the progress in polymerization catalysis and polymer reaction engineering are of key importance. The advance in organometallic chemistry has enabled progress in stereospecific synthesis, today especially in olefin polymerizations. 'Living' free radical or atomic transfer polymerizations have offered us novel possibilities to prepare various molecular architectures and block copolymers, like amphiphilic polymers or highly branched functionalised polymers, hyperbranched and dendritic polymers being the extreme results.

To fully exploit the progress in the new polymers, one needs to be able and willing to network and collaborate over the borders of different fields of science. Innovations are created at the interfaces!

Prof. Dr. Jukka Seppälä
Member of International Advisory Board

---

[*]Corresponding author, e-mail: jukka.seppala@tkk.fi

eXPRESS Polymer Letters Vol.1, No.5 (2007) 253–273
Available online at www.expresspolymlett.com
DOI: 10.3144/expresspolymlett.2007.39

The present status and key problems of carbon nanotube based polymer composites

J-H. Du[1], *J. Bai*[2], *H-M. Cheng*[1*]

[1]Shenyang National Laboratory for Materials Science, Institute of Metal Research, Chinese Academy of Sciences, 72 Wenhua Road, Shenyang 110016, P.R. China
[2]Lab. MSS/MAT, CNRS UMR 8579, Ecole Centrale Paris, 92295 Châtenay Malabry CEDEX, France

Received 5 February 2007; accepted in revised form 6 April 2007

Abstract. The state-of-art and key problems of carbon nanotube (CNT) based polymer composites (CNT/polymer composites) including CNT/polymer structural composites and CNT/polymer functional composites are reviewed. Based on the results reported up to now, CNTs can be an effective reinforcement for polymer matrices, and the tensile strength and elastic modulus of CNT/polymer composites can reach as high as 3600 MPa and 80 GPa, respectively. CNT/polymer composites are also promising functional composite materials with improved electrical and thermal conductivity, etc. Due to their multi-functional properties, CNT/polymer composites are expected to be used as low weight structural materials, optical devices, thermal interface materials, electric components, electromagnetic absorption materials, etc. However, the full potential of CNT/polymer composites still remains to be realized. A few key problems, such as how to prepare structure-controllable CNTs with high purity and consistently dependable high performance, how to break up entangled or bundled CNTs and then uniformly disperse and align them within a polymer matrix, how to improve the load transfer from matrix to CNT reinforcement, etc, still exist and need to be solved in order to realize the wide applications of these advanced composites.

Keywords: *polymer composites, carbon nanotubes, mechanical properties, electrical properties, thermal properties*

1. Introduction

Since Iijima's report on CNTs in 1991 [1], scientists have been attracted by CNT's unique atomic structure and properties, such as high aspect ratio, high strength-to-weight ratio, extraordinary mechanical properties (their axial elastic modulus and tensile strength were theoretically predicted to be as high as 1–2 TPa and 200 GPa [2–6], respectively), superior thermal and electrical properties (thermally stable up to 2800°C in a vacuum or inert atmosphere, thermal conductivity about twice as high as diamond [7], and electric-current-carrying capacity 1000 times higher than copper wires [8]). These properties of CNTs endow themselves with new scientific and technological opportunities as an ideal filler material in composites. To date, various composite materials have been prepared by incorporating SWNTs or MWNTs into a metal matrix [9–12], a ceramic matrix [13–16] or a polymer matrix [17–33]. Polymers can be easily processed and fabricated into intricately shaped components without damaging CNTs during processing using conventional methods, and hence the manufacturing cost can be certainly reduced. Therefore, CNT based polymer composites (CNT/polymer composites) stimulate great interests and have been extensively investigated.

According to the different application purposes, CNT/polymer composites can be classified as structural composites and functional composites,

---

[*]Corresponding author, e-mail: cheng@imr.ac.cn

respectively. CNTs play a different role in the two kinds of composites. For CNT/polymer structural composites, the unique mechanical properties of CNTs, such as the high elastic modulus, tensile strength and strain to fracture, the ability to withstand cross-sectional and twisting distortions and compression without fracture, are generally explored to obtain structural materials with lightweight, high elastic modulus, high tensile and compressive strength and stiffness, etc. While for CNT/polymer functional composites, many other interesting properties of CNTs, such as the high electrical and thermal conductivity, are used to develop functional materials possessing heat resistance, chemical sensing, electrical conducting, thermal conducting, photoemission, electromagnetic absorbing or energy storage performances, etc.

In recent years, many polymers, such as epoxy [17–19], PMMA [20–22], PVA [23], PVC [24, 25], PP [26–28], PE [29, 30], PA12 [31], and PS [32, 33], have been employed as matrices to prepare CNT/polymer composites. The mechanical properties combining with electrical, thermal, optical and many other properties have been extensively investigated by many research groups for a wide range of applications. However, the reported results about these properties are scattered and still far from satisfactory. Analyses of these research results show that the performance of these composites depends on many factors, such as the types of CNTs (SWNTs or MWNTs) and their morphology and structure (diameter, length and chirality, for example) [34], the processing method, the choice of matrix [34, 35], the CNT dispersion within matrix [36], the interfacial interaction between CNTs and matrix, and so on.

In this article, we will present a comprehensive review about the preparation and processing, the properties and application of CNT/polymer composites. Some fundamental challenges, which have to be overcome in order to enable the wide applications of these advanced composites, are discussed.

2. Preparation of CNT/polymer composites

In the published reports, the common fabricating methods of CNT/polymer composites are solution mixing, melt blending and *in situ* polymerization. In solution mixing, CNTs are generally dispersed in solvent and then mixed with polymer solution by mechanical mixing, magnetic agitation or high-energy sonication. Subsequently, the CNT/polymer composites can be obtained by vaporizing the solvent at a certain temperature. This method is considered as an effective measure to prepare composites with a homogenous CNT distribution and often used to prepare composite films. Epoxy is a kind of thermosetting resins and is usually employed in CNT/epoxy composites by solution mixing. Many researchers, such as Xu *et al.* [37] and Lau *et al.* [38], have fabricated the CNT/epoxy composite using this method and reported their properties. Beside the epoxy resin, other polymers such as PS, PVA, PMMA and PVC can also be processed into CNT/polymer composites by solution mixing. Mamedov *et al.* [39] applied a new deposition technique called LBL assembly to make SWNT/polyelectrolyte multilayer composites, which can be considered as an improved solution mixing method. The resulting SWNT/polyelectrolyte membranes were very strong and the ultimate tensile strength was found to be 220±40 MPa with some readings as high as 325 MPa.

Melt blending is a versatile and commonly used method to fabricate polymeric materials, especially for thermoplastic polymers. CNTs are dispersed within the polymer matrix by rheological shear stress generated from the blending of CNTs with melt polymer. Its well-known disadvantage is that CNTs can easily be damaged to a certain extent or broken in some cases [40, 41]. All the CNT/polymer composites using thermoplastic polymers as matrix can be processed in this manner. Jin *et al.* [42] fabricated MWNT/PMMA composite using this method and studied its dynamic mechanical behavior. The results indicate that CNTs were well dispersed in the polymer matrix with no apparent damage or breakage. The storage modulus of the polymer was significantly increased by the incorporation of CNTs particularly at high temperatures. The melt blending method is frequently used to prepare CNT/polymer composite fibers. Haggenmuller *et al.* [22] and Kumar *et al.* [26] prepared SWNT/PMMA composite fibers and CNF/PP composite fibers using melt spinning process and the obtained fibers showed improved mechanical properties.

In situ polymerization is considered as a very efficient method to significantly improve the CNT dispersion and the interaction between CNTs and polymer matrix. Generally, CNTs are firstly mixed with monomers and then CNT/polymer composites can be obtained by polymerizing the monomers under certain conditions. Jia *et al.* [20] initially reported the fabrication of CNT/PMMA composites by in situ polymerization. The results showed that a strong binding interface was formed between the CNTs and PMMA because the CNTs could be initiated by AIBN to open their π bonds and participate in the PMMA polymerization. It was reported that for a surface modified CNT/PMMA composite fabricated by an improved in situ process, not only was the dispersion ratio of CNTs in the PMMA matrix improved, but also the mechanical properties of the composites were enhanced when the CNT content was lower than 10 wt%. Ying *et al.* prepared surfactant-coated CNT/epoxy composites by in situ polymerizing epoxy resin with polyamide curing agent, and then their mechanical properties were studied [43–45]. The results showed that the tensile strength and ultimate strain of the composites were increased by 20% and 70%, respectively. Li *et al.* [46] reported the fabrication and characterization of SWNT/PANI composites by *in situ* polymerization of an aniline solution containing different SWNT contents. Electron microscopy and conductive analysis showed that they had uniform CNT dispersion and high electric conductivity.

In order to bring out the anisotropic nature of CNTs, it is important to align CNTs in a polymer matrix during processing of CNT/polymer composites. This has been done by several groups [47–57] based on slicing the composite [51], mechanical stretching [52, 53], filtrating the CNT dispersion under a high magnetic field [54], melt-processing and electrospinning [55], etc. Gao *et al.* [56] described that aligned conducting CNTs can be used to make novel CP-NT coaxial nanowires by electrochemically depositing a concentric layer of an appropriate conducting polymer uniformly onto each of the constituent aligned CNTs. For a conducting-polymer sheathed CNT with an outer diameter of 221 nm, inner diameter of 94.7 nm and length 9.3 μm, its elastic modulus was determined to be 13.6 GPa, much higher than that of the polymer. Li *et al.* [24] first reported to successfully synthesize long ropes of SWNT bundles with rope lengths up to 30 mm. These ropes consist of roughly aligned SWNT bundles, which consist of well-aligned SWNTs. Then such aligned SWNT ropes were impregnated with PVC resin to form composite ropes. These ropes showed significantly improved mechanical properties with the average tensile strength as high as 3.6 GPa. Dalton *et al.* [25] used a modified coagulation-based CNT spinning method to spin a reel of nanotube gel fiber and then convert it into 100 m long solid CNT composite fiber in a continuous process, at a rate of more than 70 cm·min^{-1}. The obtained composite fibers were about 50 μm in diameter and contained around 60 wt% SWNTs. They had a tensile strength of 1.8 GPa and tougher than most natural or synthetic organic fibers described so far.

3. Present status of CNT/polymer composites

3.1. CNT/polymer structural composites

CNTs are considered to be the ultimate mechanical filler material [58] and open the way for a new generation of high performance structural composites. In recent years, many studies with different focuses on mechanical properties of CNT/polymer structural composites have been published. However, the most impressive themes seem to be enhancement of elastic modulus and tensile strength. Another important property–fracture toughness has also been reported to be significantly improved in many works. We therefore will focus on the elastic modulus, tensile strength and toughness enhancement below.

Table 1 and 2 show some representative mechanical properties of randomly oriented and aligned CNT/polymer composites, respectively. From these two tables, it can be found that the elastic modulus of CNT/polymer composites can always be obviously increased comparing with those of pure polymer matrices. However, most of randomly oriented CNT/polymer composites show only a moderate or no strength enhancement, especially for CNT/polymer composites using untreated CNTs as reinforcements, mainly attributed to poor CNT dispersion within the matrix and poor load transfer between CNTs and polymer matrix. Homogeneous dispersion of CNTs throughout a matrix without destroying their integrity is essential for CNT reinforced polymer composites. Moreover, good interfacial bonding is required to achieve effective load transfer across CNT/matrix interface, a necessary condition for improving the mechanical properties of polymer composites [59–64]. From Table 1, it can be seen that the strength of nearly all CNT/polymer composites using modified CNTs as reinforce-

Table 1. Representative mechanical properties of randomly oriented CNT/polymer composites

Author	Sample	Tensile strength [MPa]	Elastic modulus [GPa]	Remarks
Gong *et al.* [65]	Epoxy+1wt% MWNTs		Increased by more than 30%	
Ying *et al.* [44]	Pure Epoxy	52	1.18	
	Epoxy + 2wt% MWNTs	46	1.18	Untreated MWNTs
	Epoxy + 2wt% MWNTs	55	1.35	MWNTs were treated with PVA
	Epoxy + 2wt% MWNTs	62	1.39	MWNTs were treated with poly-oxyethylene-9-alkyl ether
	Epoxy + 2wt% MWNTs	58	1.34	MWNTs were treated with poly-oxyethylene-7-alkyl ether
Andrews *et al.* [66]	PS + 0.05 to 0.5 vol.% MWNTs	Significant reduction	Little change	MWNTs were heated in an inert atmosphere to a high temperature in the range 1800 to 2600°C
	PS + 2.5 to 25 vol.% MWNTs		1.9~4.5	
	High impact PS & ABS + 0.05 to 0.5 vol.% MWNTs	Little effect on tensile strength of either	Small increase	
Zhang *et al.* [67]	HDPE + 2 wt% SDS	~14.5	~0.47	SWNT aqueous solution prepared at the aid of SDS was sprayed onto the surface of HDPE. The composites were obtained by melt processing
	HDPE + 2 wt% SDS + 0.5 wt% SWNT	~19	~0.57	
	HDPE + 2 wt% SDS + 2.6 wt% SWNT	~23	~0.7	
Qian *et al.* [68]	PS	~12.8	~1.19	
	PS + 1 wt% MWNTs	~16	~1.62	CNT with 15 µm average length
	PS + 1 wt% MWNTs	~16	~1.69	CNT with 50 µm average length
Jia *et al.* [20]	PMMA + 0.08 wt% AIBN	54.9		
	PMMA + 0.24 wt% AIBN + 1 wt% CNTs	21.2		Untreated CNTs
	PMMA + 0.28 wt% AIBN + 3 wt% CNTs	20.3		
	PMMA + 0.1 wt% AIBN + 1 wt% CNTs	58.7		CNTs were ground in a ball mill and the improved *in situ* process was used to fabricate the composites
	PMMA + 0.1 wt% AIBN + 3 wt% CNTs	66.8		
	PMMA + 0.1 wt% AIBN + 5 wt% CNTs	71.7		
Jin *et al.* [42]	PMMA + MWNTs	The storage modulus was significantly increased, particularly at high temperature		
Jin *et al.* [69]	PMMA + MWNTs	The storage modulus of composite containing 0.5 wt% PVDF was almost twice as that of MWNT/PMMA without PVDF at 50°C		
Geng *et al.* [70]	PEO		0.06	
	PEO + 1 wt% fluorinated SWNTs		0.15	
Tong *et al.*[29]	Pure PE	34.1	0.81	
	PE + 0.5 wt% SWNTs	28.9	0.64	Untreated SWNTs
	PE + 0.5 wt% SWNTs	33.3	0.8	SWNTs were modified with PE prepared by in situ Ziegler-Natta polymerization
Paiva *et al.* [71]	PVA		~4	
	PVA + 2.5 wt% SWNTs		~5.6	CNTs were functionalized with low molecular weight PVA
	PVA + 5 wt% SWNTs		~6.2	
	PVA + 2.5 wt% SWNTs		~5.4	Untreated SWNTs

ments can be increased to some extent. It means that the surface modification of CNTs plays an important role in improving the mechanical reinforcement of the composites.

Compared to randomly oriented CNT/polymer composites, aligned configuration has a higher efficiency of reinforcement. In most cases, both tensile strength and elastic modulus of aligned CNT/polymer composites are significantly improved. In Figure 1, the tensile strength (Figure 1a) and elastic modulus (Figure 1b) of randomly oriented and aligned CNT/polymer composites are summarized. It can be seen that the tensile strength and elastic modulus of randomly oriented CNT/polymer composites are generally less than 100 MPa and 6 GPa, respectively. They are much lower than those of aligned CNT/polymer composites, which can even reach as high as 3600 MPa and 80 GPa, respec-

Table 2. Representative mechanical properties of aligned CNT/polymer composites

Author	Sample	Tensile strength [MPa]	Elastic modulus [GPa]	Remarks
Gao *et al.* [56]	PANI + MWNTs		13.6	Prepared by electrochemical deposition
Andrew *et al.* [48]	Isotropic petroleum pitch macrofiber	~450	~33	Produced by extrusion. The average diameter of fibers was ~18 µm
	Isotropic petroleum pitch + 1% SWNT macrofiber	~620	~42	
	Isotropic petroleum pitch + 5% SWNT macrofiber	~850	~78	
Haggenmuelle *et al.* [22]	Pure PMMA fiber		~3.1	Produced by the melt spinning process
	PMMA + 1 wt% SWNT nanocomposite fiber		~3.3	
	PMMA + 5 wt% SWNT nanocomposite fiber		~5	
Kumar *et al.* [26]	PP macrofiber	490	4.6	Spun using conventional melt spinning technique
	PP + 5 wt% MWNT macrofiber	570	7.1	
Bhattacharyya *et al.* [50]	PP	430	4.2	Significant CNT aggregation
	PP + 0.8 wt% SWNTs	420	4	
Li *et al.* [24]	PVC + SWNTs	3600		
Vigolo *et al.* [49]	PVA + SWNT composite fibers		9~15	
Dalton *et al.* [25]	PVA + 60 wt% SWNT composite fiber	1800	80	Produced by modified coagulation-based CNT spinning method
Siochi *et al.* [72]	PI	105	2.2	SWNT alignment in the composite fiber direction was induced by shear force present during the melt extrusion and fiber drawing processes
	PI + 0.1 wt% SWNTs	105	2.6	
	PI + 0.3 wt% SWNTs	105	2.8	
	PI + 1 wt% SWNTs	105	3.2	
Chen and Tao [73]	TPU	~12.4	~7.7	Prepared by a solution process
	TPU + 0.5 wt% SWNTs	~13.3	~14.5	
Ruan *et al.* [74]	UHMWPE	~3510	~122.6	Gel-spun composite fibers were drawn at draw ratio of 30
	UHWMPE + 5 wt% MWNTs	~4170	~136.8	

tively. Moreover, the tensile strength and elastic modulus are always higher for aligned CNT/polymer composites containing higher CNT content, while this is not the case for randomly oriented CNT/polymer composites.

In many reports, a critical CNT content in matrix can be found when the CNT strengthening effect on randomly oriented CNT/polymer composites are investigated. Below this content, the strengthening effect for randomly oriented CNT/polymer composites increases with increasing CNT content. Above this content, the strength of CNT/polymer composites decreases, and in some cases, even lower than that of the polymer matrix. The work of Bai *et al.* [34] shows that the critical CNT loading percentage was about 0.5 wt% for CNT/epoxy composites. This ratio is also very close to the percolation threshold for electrical conductivity. The same tendency was reported by Meguid and Sun [75] in their work on the tensile and shear strength of nano-reinforced composite interfaces. The excess CNTs increase the viscosity of polymers, and can also cause some surface of the CNTs not be completely covered by polymer matrix due to the large specific surface area of CNTs. This makes uniform dispersion and load transfer more difficult. Moreover, it is very difficult for high quantity of polymers to intercalate among CNTs when the CNT content becomes high. Shaffer *et al.* [76] reported that, by trivial estimation, even a 1 vol% loading of SWNTs ensures that all of the polymer molecules are within one radius of gyration (say 5 nm) of a nanotube. This result implies that complete wetting of high loading fraction of SWNTs will be difficult, at least by conventional means.

Although much higher than those of randomly oriented CNT/polymer composites and, in some cases, representing the highest mechanical properties amongst all ultra-strong fibers reported so far, the obtained tensile strength and elastic modulus of aligned CNT/polymer composites are still far from satisfactory as far as the mechanical properties of

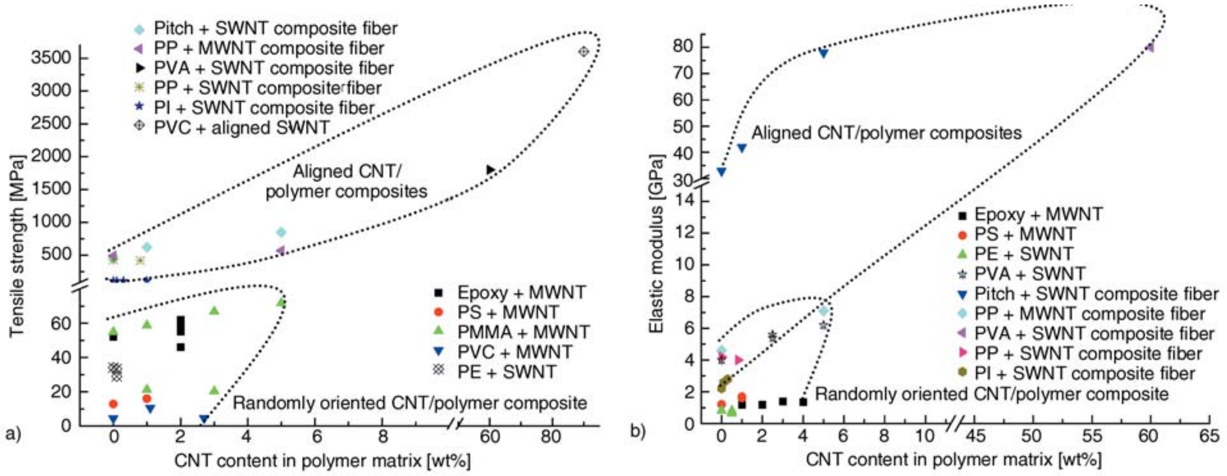

Figure 1. Tensile strength (a) and elastic modulus (b) of CNT/polymer composites

CNTs are considered. The main possible reason is sliding between CNTs under macroscopic tensile loading and between CNT and matrix.

Figure 2 shows several representative stress-strain curves of CNT/polymer composites with different polymers as matrices. It can be found that the curvilinear trend of CNT/polymer composites strongly depends on the matrix nature. Most of the reported stress-strain curves show improvement in strength and loss of strain to failure (Figure 2a, c, d). The strain to failure usually decreases with the increase of CNT content. However, CNT/polymer composites using PE and PEO as matrices show a substantial enhancement in strain to failure and toughness (Figure 2b). This indicates that significant toughening of some polymer matrices through the incorpo-

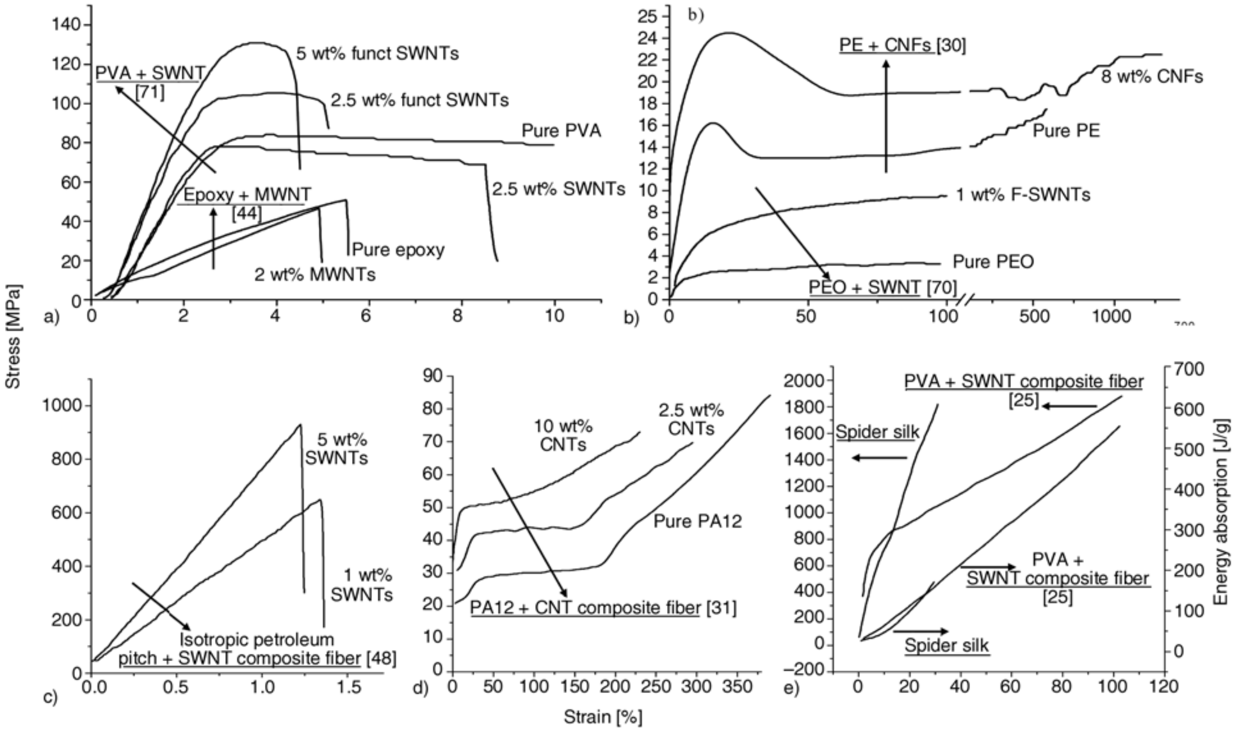

Figure 2. Representative strain-stress curves of CNT/polymer composites using different polymers as matrix. a, b) randomly oriented CNT/polymer composites [30, 44, 70, 71] and c, d, e) aligned CNT/polymer composites [25, 31, 48]

[25] Reused with permission from NPG

[30, 31, 71] Reused with permission from Elsevier

[48] Reused with permission from American Institute of Physics

[70] Reused with permission from Wiley-VCH

ration of CNTs can be obtained. In such instances, the commonly used polymers including PE, PEO and PVA, are semi-crystalline thermoplastic polymers. Certain conditions, such as the presence of modified CNTs, preparation temperature of composites, pre-drawing treatment of CNT/polymer composite fibers at the temperature above the T_g of polymer matrix generally can influence their crystallization behaviour, and hence significantly affect the toughness characteristics of the composites. Ruan *et al.* [77] first reported that MWNT/PE composite films with high pre-drawing ratios showed an up to 150% increase in strain energy density together with a simultaneous increase of tensile strength of ~25% and an increase of ductility up to 140% in comparison with the pure PE film at similar pre-drawing ratio. Secondary crystallites, which were nucleated from the MWNTs and might grow during hot drawing, were much more mobile than the extended PE crystals and led to a significantly enhanced ductility and hence an increase in strain energy of the composite film [78]. Lozano *et al.* [30] reported that CNFs, which can also be considered as MWNTs since the diameter of fibers ranging between 40 and 150 nm, and PE could act in a synergistic manner to increase both strength and strain to failure of CNF/polymer composites (Figure 2b). They prepared the composite by mixing the functionalized CNFs and PE at 180°C and then pressed at 200°C. Dalton *et al.* [25] reported that their pre-drawn 60 wt% SWNT/PVA composite fibers matched the energy absorption of spider silk up to the breaking strain of the toughest silk (30%), and continued absorbing energy until reaching an energy-to-break (570 J/g) which is much higher than that of spider dragline silk (165 J/g [79]) (Figure 2e). While SWNT/PVA composite film, which was prepared by wet-casting [71] and no pre-drawing treatment and crystallinity, shows no increase in toughness (Figure 2a).

Since CNTs can enable polymer matrix to obtain a stronger and more lightweight composite due to their superior mechanical properties and small size, the obvious application of CNT/polymer composite can be as structural materials in several fields including aerospace, sports, automotive, infrastructure and defense. For example, super strong CNT/polymer composite fibers will have many applications including body and vehicle armor, transmission line cables, woven fabrics and textiles, etc. CNTs' high strength and toughness-to-weight characteristics may also prove valuable as part of composite components in fuel cells that are deployed in transport applications, where durability is extremely important. Inspired partly by science fiction, NASA scientists are seriously considering space elevators as a mass-transit system. The material of choice for a space elevator is a super-strong CNT/polymer composite fiber, which is the only known substance at present that can successfully be used and make a space elevator possible. Several manufacturers of sports equipment have advertised CNTs as reinforcements of some of their top sports products. Easton Sports, the leading manufacturer of sporting goods, manufactured the world's first CNT two-piece all-composite bats, which represents the best bats Easton Sports has ever made [80].

3.2. CNT/polymer functional composites

3.2.1. Electrical properties and application of CNT/polymer composites

Many experimental results have shown that the combination of CNTs with polymers offers an attractive route to introduce new electrical properties [17, 23, 66, 81], and conductive composites can be constructed at low loading of CNTs due to low percolation thresholds originated from the high aspect ratio and conductivity of CNTs. Figure 3 and Table 3 summarize some reported electrical properties of CNT/polymer composites. It can be found in Figure 3 that all CNT/polymer composites exhibit a typical percolation behavior and introduction of CNTs to polymers can increase the conductivity of the resulting composites to several orders of magnitude or even higher than ten orders of magnitude. However, very different percolation thresholds (from 0.0025 wt% for CNT/epoxy composite to 11 wt% for SWNT/P3OT composite) have been obtained by different research groups (see Table 3). Sandler *et al.* [17] measured the electrical conductivity of untreated CNT/epoxy composites, and found that the percolation threshold was between 0.0225 and 0.04 wt% CNTs. Subsequently, they further presented the lowest threshold (0.0025 wt% for aligned SWNT/epoxy composites) observed for CNT/polymer composites yet reported [83]. Allaoui *et al.* [84] also studied the electrical performance of MWNT/epoxy composites and revealed that the presence of a percolation thresh-

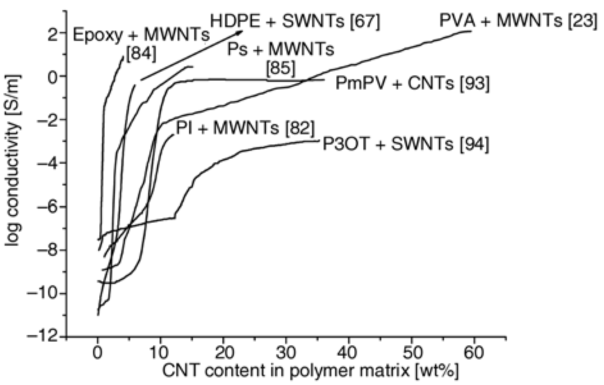

Figure 3. Representative semilogarithmic plot of the electrical conductivity of CNT/polymer composites with various weight percents of CNTs in different polymer matrices [23, 67, 82, 84, 85, 93, 94].
[23] Reused with permission from Wiley-VCH
[67, 82, 84, 94] Reused with permission from Elsevier
[85] Reused with permission from Springer
[93] Reused with permission from Dr. J. N. Coleman

old between 0.5 and 1 wt% CNTs. When adding 1 wt% CNTs into epoxy matrix, the composite became conductive with a conductivity as high as 10^{-3} S/cm. Shaffer *et al.* [23] fabricated CNT/PVA composites and measured their electrical conductivity using impedance spectroscopy in a four-point configuration. The percolation threshold for these composites lay between 5 and 10 wt%. At the CNT concentration of 10 wt%, the electrical conductivity of the composite was about 1 S/cm, an increase by about seven orders of magnitude. Kymakis *et al.* [94] presented a percolation threshold of approximately 11 wt% SWNTs in a P3OT polymer. As the CNT concentration increased from 0 to 20 wt%, the conductivity of the composites was increased by five orders of magnitude.

Table 3. Representative percolation threshold of CNT/polymer composites

Author	Sample	Percolation threshold [wt%]
Sandler *et al.* [17]	Epoxy + CNTs	0.0225~0.04
Sandler *et al.* [83]	Epoxy + aligned MWNTs	0.0025
Allaoui *et al.* [84]	Epoxy + CNTs	0.5~1
Shaffer *et al.* [23]	PVA + MWNTs	5~10
Dufresne *et al.* [85]	PS + MWNTs	≤3
Andrews *et al.* [66]	PS + MWNTs	0.25 vol.%
Barraza *et al.* [86]	PS + SWNTs	8.5
Zhang *et al.* [67]	HDPE + SWNTs	4
McNally *et al.* [87]	PE + MWNTs	7.5
Hu *et al.* [88]	PET + MWNTs	0.9
Seo *et al.* [89]	PP + CNTs	1~2
Seo *et al.* [90]	PP + CNTs	2
Tchmutin *et al.* [91]	PP + SWNTs	4.5 vol.%
Meincke *et al.* [92]	PA6 + CNTs	4~6
Coleman *et al.* [93]	PmPV + CNTs	8.5
Kymakis *et al.* [94]	P3OT + SWNTs	11

Based on the reported results up to now, CNT/epoxy composites show a much lower percolation threshold, although the reported values are very different. For CNT/PS composites, the percolation threshold was reported ranging from 0.25 vol% to 8.5 wt% by different groups. These differences can be attributed to many factors. The electrical properties of CNTs used by different research groups are generally significantly different depending on their purity, morphology, aspect ratio, etc. In addition, the interaction between matrix and CNTs influences the quality and quantity of electrical contacts between the CNTs. As reported by Shaffer *et al.* [23], it seems that the P3OT is easier to form an adsorbed layer on the surface of CNTs than epoxy resin, which reduces the quality and quantity of electrical contacts, thus the percolation threshold of CNT/P3OT composite cannot be reached at a relatively lower CNT loading. In Table 3, it can also be found that the electrical percolation threshold of CNT/polymer composites with semicrystalline thermoplastic matrices (PP, PE, PEO, PA) is always higher than those of CNT/epoxy composites. Hu *et al.* [88] first used coagulation method to prepare MWNT/PET composites and found that the percolation threshold of the composite was 0.9 wt%. Seo *et al.* [89, 90] presented that the conductivity of CNT/PP composites was increased with increasing the CNT content and the electrical percolation threshold was formed between 1 and 2 wt% CNTs. Meincke *et al.* reported that percolation threshold of CNT/PA6 composite at CNT loading 4~6 wt%. Additional complexity arises in case of semi-crystalline matrices, where it is envisaged that the dispersion of CNT is significantly affected due to the crystallization induced phase separation and subsequent rejection of CNTs by the advancing crystalline fronts [95]. On the other hand, purity and defect concentration of CNTs, dispersion and alignment of CNTs within a matrix, are also the main factors influencing the electrical properties of CNT/polymer composites.

Nevertheless, compared with CB and carbon fiber based composites, whose electrical percolation threshold are usually up to 15–20 wt% and 9–

18 wt%, respectively, CNT/polymer composites still have much lower electrical percolation threshold due to their high aspect ratio and small diameter. Therefore, in many fields, CNTs are expected to substitute CB as conductive fillers. In 2005, He *et al.* [96] reported the temperature-resistivity characteristics of MWNT/HDPE composites. They found that when temperature was between 120 and 130°C, the electrical resistivity of the 5.4 wt% MWNT-filled HDPE composite increased sharply with the increase of temperature, showing a strong PTC effect. While for CB/HDPE composite, the loading concentration of CB was nearly three times as high as that of MWNTs to obtain the PTC effect. Moreover, when temperature was above T_m of HDPE, the CB/HDPE composite exhibited obvious NTC effect. However, the NTC effect in MWNT/HDPE composites was quite small. So, CNT instead of CB based polymer composites are expected to be used in self-controlled heaters, overcurrent protectors, sensors, etc.

Besides, given high conductivity and super mechanical properties of CNT/polymer composite, they can also be exploited as EMI shielding composites, coatings for enclosures, ESD composites, antistatic materials, conductive coatings, electromagnetic absorption materials for low-observable applications, electrode materials for supercapacitor and fuel cell, etc.

3.2.2. Thermal properties and application of CNT/polymer composites

Many researches indicate that CNTs may be the best heat-conducting material that has ever been known. Scientists predict that the thermal conductivity can reach as high as 6600 W/mK at room temperature for a SWNT [97] and experimental value is 3000 W/mK for an isolated MWNT at room temperature [98]. It is expected, therefore, that CNTs can significantly enhance the thermal conductivity and thermal stability of some polymers at high temperature [99–102]. Wei *et al.* [101] carried out classical molecular dynamics simulations employing Brenner potential for intra-nanotube interactions and van der Waals force for polymer-nanotube interface to investigate the thermal expansion and diffusion characteristics of CNT/PE composites. The addition of CNTs was found to increase T_g and thermal expansion and diffusion coefficients in the composite above T_g. Xu *et al.* [103] fabricated SWNT/PVDF composites by dispersion of SWNTs in an aqueous surfactant solution, followed by mixing with PVDF powder, filtration and hot pressing. The measured thermal diffusivity of the composites increased with increase of the SWNT content, but decreased with increasing temperature because the phonon scattering was enhanced with increasing temperature for polymers. Kashiwagi *et al.* [99] fabricated MWNT/PP composites with good dispersion, and CNTs were found to significantly enhance the thermal stability of PP in nitrogen at high temperatures. Especially, the CNT addition significantly reduced the heat release rate of PP and they were found to be at least as effective as clay/PP composite for flame-retardance.

Many efforts have also been devoted to the use of CNTs as thermal conducting fillers in polymer composites and some enhancements in the thermal conductivity are usually observed. Thostenson *et al.* [104] found that the thermal conductivity of CNT/epoxy composites increased linearly with CNT concentration to a maximum increase of 60% at 5 wt% CNTs. Liu *et al.* [105] reported an enhancement of 65% in thermal conductivity with 4 wt% CNT loading in silicone elastomer. Biercuk *et al.* [102] used SWNTs to augment the thermal transport properties of epoxy and found that epoxy loaded with 1 wt% SWNTs exhibited a 70% increase in thermal conductivity at 40 K and 125% at room temperature. But these enhanced values are still far below those predicted using the ‘rule of mixtures’ and unlike electrical conductivity, which is based on a percolation mechanism, the increase in thermal conductivity with increasing CNT concentration is nearly linear in many cases, while in practice this has been observed to be nonlinear in certain cases. The important reasons probably rest in lower intrinsic thermal conductivity of the CNTs used, scattering of phonons by interactions with the surroundings or with defects. An alternative or probably main reason is that high resistance at the CNT-matrix or CNT-CNT interfaces limits thermal transport along percolating networks of CNTs and this leads to a rapid increase in the overall thermal resistance.

In order to investigate the effect of interface thermal resistance at CNT-matrix, which may be due to the weak bonding between polymer matrix and CNT walls, many numerical simulations have been carried out to predict the interfacial heat flow between the CNTs and the matrix. Shenogin *et al.* [106] studied the effect of thermal boundary resistance on the heat flow in CNT composites. They found that the effective thermal conductivity of CNT/polymer composites was limited by interface resistance. A theoretical model was proposed by Huxtable *et al.* [107] to evaluate the thermal conductivity of the composite with interface resistance, and it was found that the interface played an important role in the thermal conduction through CNT composites. Nan *et al.* [108] developed a simple formula for the thermal conductivity enhancement in composites by incorporating the interface thermal resistance with an effective medium approach, and found that a large interface thermal resistance across the CNT-matrix interface caused a significant degradation in the thermal conductivity enhancement, even for the case with ultrahigh intrinsic thermal conductivity and aspect ratio of the CNTs embedded. On the other hand, the relationship between thermal conductivity and functionalization of the surface of CNTs are also be predicted by many groups because surface modification to CNTs is a possible approach to improve the interfacial adhesion and then reduce the interfacial thermal resistance between the CNTs and the matrix. However, many calculations indicate that the interface thermal resistance has a smaller effect on the overall conductivity of the composites, which is especially sensitive to the length and diameter of CNTs [109, 110]. Consequently, some experiments are designed to investigate the functionalized CNTs on the thermal conductivity of composites. Liu *et al.* [111] prepared the composites of the polydimethylsiloxane rubber with 2 wt% chemical-treated CNTs to investigate the influence of chemical modifications and defects on the thermal conductivity of CNT composites. This study reveals that moderate chemical modifications are beneficial to improve the thermal conductivity of CNT composites. However, their negative effects to the thermal conductance are more remarkable than the theoretical anticipation. Figure 4 shows the measured thermal conductivity of epoxy matrix composites with different fillers and content [112]. It can be seen that the largest improvement is non-functionalized CNT composites. These experimental results substantiate the requirement of a weak interfacial adhesion, since the composites containing amino-functionalized CNTs show relatively lower thermal conductivity compared to the corresponding composites with non-functionalized CNTs. Based on these theoretical and experimental results, it is obvious that to reduce interfacial thermal resistance by functionalization of CNTs is not preferable, and some new techniques therefore should be developed.

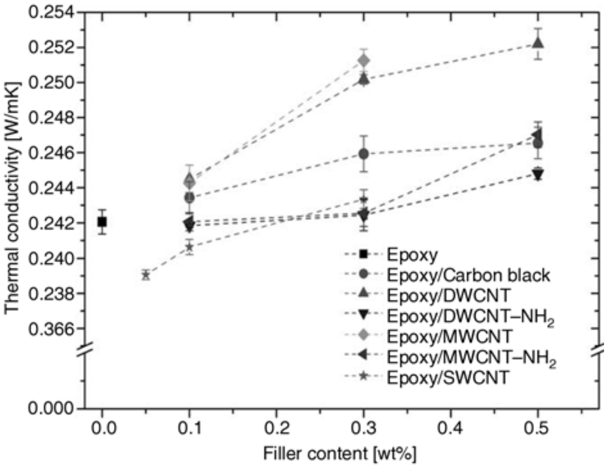

Figure 4. Thermal conductivity as a function of filler content for epoxy composites[112]. Reprinted with permission from elsevier

To avoid the effect of interface thermal resistance between the overlaps in CNT passage, an ideal CNT composite structure (TIM Model) was proposed by Huang *et al.* [113] to take advantage of the high thermal conductivity of CNTs. In their structure, all the CNTs embedded in the matrix were aligned from one surface to the opposite side with all the CNT tips revealed on both surfaces. According to this model, the aligned CNT composite film was prepared by *in situ* injection molding method. The enhanced thermal conductivity as a function of CNT loading for both aligned CNTs and randomly oriented CNTs are plotted in Figure 5. It can be seen that with only a small fraction of aligned CNTs (0.3%), the enhanced value of thermal conductivity is fairly high (0.65 W/mK). However, from the inset of Figure 5, it can be seen that there is only a marginal enhancement using the same loading of randomly oriented MWNTs, and the enhanced value is only 4.6% of that of an aligned CNT array. Obviously, the new structure is very effective to improve the thermal conductivity of CNT composites.

The prominent thermal properties of CNTs make them promising materials for future application as thermal management materials, such as TIMs, which are commonly used to fill air gaps between two surfaces of electronic components and base

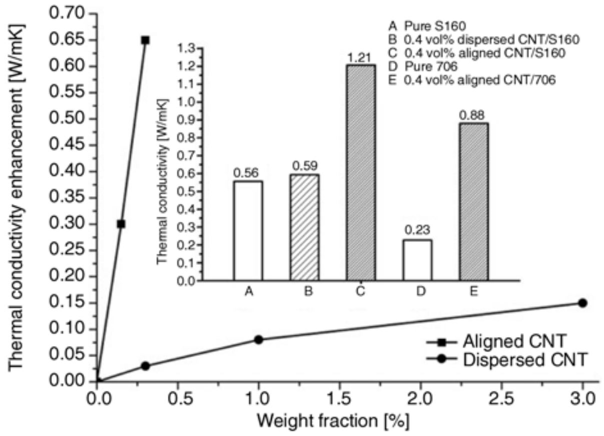

Figure 5. The enhanced values of thermal conductivity of CNT/polymer composites vs. weight fractions of CNTs [113]. Reprinted with permission from Wiley-VCH

plates of heat sinks, and thus minimize the thermal contact resistance between them and dissipate heat efficiently [114]. Based on the ideal TIM model Huang *et al.* [113] predicted that if the volume fraction of CNTs can be as high as 10% in the composites, the value of thermal conductivity would increase to an order of magnitude higher than that of most current commercial materials. They can also be used as temperature sensors, resistance heating and flame-retardance materials, etc.

3.2.3. Other functional properties and application of CNT/polymer composites

Beside electrical and thermal properties, optical and many other functional properties of CNT/polymer composites, are also fascinating. Jin *et al.* [115] studied the nonlinear optical properties of MWNT/PPA-C16TAB composite with 532 nm nanosecond laser pulses and obtained an effective nonlinear refractive index of $6.8\cdot10^{-18}$ m^2/W. Similarly, a value of $1.2\cdot10^{-17}$ m^2/W was obtained for MWNT/PEO composite [116]. They predicted that MWNT/PPA-C16TAB composite could be a potential candidate for solid nonlinear optical devices because of its ease to prepare a cast film. Davey *et al.* [63] prepared MWNT and SWNT/PmPV composites, and found that SWNTs could be used to enhance the luminescent properties of the conjugated polymer PmPV. The enhancement of luminescence and thus an increase in quantum yield opens up the area of luminescent polymers. Davey *et al.* [63] also proposed that the main contribution of CNTs to optical nonlinearity would arise from 1-D polarization of delocalised π-electrons in a fixed lattice configuration. They found that MWNT/PmPV composite showed a strong nonlinear signal, which is very applicable in the area of high performance nonlinear optical devices. Chen *et al.* [117] reported that SWNT/polymer composites, especially SWNT/PI composite, not only had an optical decay time of less than 1 ps, but also a high third-order nonlinear polarizability, which makes the composite a promising material for high-quality subpicosecond all-optical switches.

A few papers have studied the electromagnetic and microwave absorption properties of polymer composites reinforced with CNTs. Fan *et al.* [118] studied electromagnetic and microwave absorption applications of CNT/PET, PP, PE and varnish composites in the range of 2–18 GHz, and found that 4 wt% CNT/PET and 8 wt% CNTs/varnish composites had considerable absorbing peak at 7.6 GHz, 15.3 GHz and achieved maximum absorbing value of 17.61 dB, 24.27 dB, respectively. In addition, the frequency ranges for absorbing values exceeding 5 dB of CNT/(PET, PP, varnish) composites are 13 GHz, 10 GHz and 6 GHz, respectively. The microwave absorption between 2 GHz and 18 GHz can be mainly attributed to the dielectric loss rather than magnetic loss. The results indicate that these composites are good candidates as microwave absorption materials.

Recently, Wei *et al.* [119] synthesized PANI nanotubes doped with MWNT-$(OSO_3H)_n$ through self-assembly method and Zhang *et al.* [120] developed a facile approach to noncovalently functionalize graphitized MWNTs with the water-soluble conducting polymer of SPAN. The functionalization was based on the *in sit*u polymerization of aniline and MWNTs followed by sulfonation with chlorosulfonic acid in an inert solvent and by hydrolysis in water. The lengths and surface structure of MWNTs were not perturbed with the incorporation of SPAN. The SPAN functionalized MWNTs (MWNT/SPAN composite) were highly soluble in water. These reports open many new possibilities for the prospective technological applications of CNT/polymer composites in nanoelectronic and biomedical devices and sensoring, etc. In addition, the addition of CNTs to the polymer matrices can also modify the electromagnetic interference shielding effectiveness, optoelectronic properties [121], thermoelectric energy conversion, etc.

4. Key problems of CNT/polymer composites

Based on the review about the properties and application of CNT/polymer structural composites and functional composites, it is obvious that CNT/polymer composites are muti-functional and are expected to be used as automotive components, sports goods, and electronic products. They also can be used in textile and aerospace industry, etc. In a word, the application of CNT/polymer composites is at an embryonic stage of development but the scope is large and growing. The present status demonstrates that the results of enhancement in performance of CNT/polymer composite are scattered, especially for CNT/polymer structural composites. Many key issues should be addressed to realize the wide applications of these advanced composites in practice.

4.1. Structure control of CNTs

It is well known that the most important factor that determines the ultimate mechanical and other functional properties of CNT/polymer composites should be the inherent properties of CNTs. Presently, a large amount of CNTs can be prepared by electric arc discharge, laser ablation and chemical vapor deposition. But the obtained CNTs are not consistent in their structure, morphology, aspect ratio, crystallinity, crystalline orientation, purity, electric conductivity and mechanical properties, etc. Therefore, the properties of resulting CNT/polymer composites will naturally be very different even if the composites are fabricated by the same method and with the same polymer matrix.

To obtain the CNTs of high purity and uniformity is one of the big issues that still impact the applications of CNT/polymer composites. The as-prepared CNTs are usually not pure and contain a lot of impurities, some of them, such as amorphous carbon and fullerenes, can hardly be completely removed from the raw materials, and the purity is difficult to be quantified. Thus, the measured physical and chemical properties of CNTs are peculiar to different research groups. In addition, the structures of the obtained CNTs always possess surface defects and even are not identical in geometrical structure, which cause the actual mechanical strength, electrical and thermal conductivity as well as other properties far from the theoretical predictions. Furthermore, CNTs are not continuous so that the macroscopic samples will not have the same good performance as the single CNT. Therefore, to start with, the most important problem is to prepare structure-controllable CNTs with high purity, geometrical uniformity and consistently dependable high performance.

In addition, CNTs normally are randomly oriented and entangled with each other. Especially, CNTs prepared by electric arc discharge tend to form bundles. It is very difficult to break up these entangled and bundled CNTs to produce individual ones and then disperse them uniformly in polymer matrices. Therefore, a revolutionary progress of CNT application can only be realized when we know how to break up the entangled and bundled as-prepared CNT products to produce individual CNTs without damaging their properties or to directly produce individual CNTs.

4.2. Dispersion of CNTs within polymer matrix

Uniform dispersion of CNTs in polymers is also a fundamental challenge. In fact, no matter what preparation method is adopted, the main purpose is to uniformly disperse CNTs within a polymer matrix and obtain composites with intrinsic properties [59, 60, 122]. In general, several factors that influence the dispersion of CNTs in a polymer matrix have to be considered in the preparation process of CNT/polymer composites. The entangling of CNTs during growth process and the attraction between CNTs by van der Waals force make CNTs themselves tend to aggregate. So it is difficult for CNTs to be separated from one another within the polymer matrix in mixing stage. These factors prevent CNTs from being well dispersed within polymers. The obtained CNT/polymer composites are poor in their mechanical performance and the intrinsic properties of the composites cannot be achieved.

Presently, there are two main kinds of surface treatment for CNTs to improve their dispersion within a polymer matrix. One is surface functionalization: Some functional groups, which can improve the interaction between CNTs and polymer matrix, are covalently bonded directly to the surface of CNTs. Gojny *et al.* [19] treated MWNTs with oxidizing inorganic acids. The oxidized CNTs were embedded in epoxy resin and the resulting composite was investigated by TEM. The results indicated that through the treatment with oxidizing inorganic acids, the outer shells of CNTs were damaged to some extent and carboxylic groups were formed on the surface, which enables a better dispersion of CNTs. However, surface functionalization may disrupt the bonding between graphene sheets, and thereby reduce the properties of functionalized CNTs in the final composites. Another method is to have CNTs physically coated by some surfactants, which is a non-covalent approach and may be a more facile and practical processing technique. Gong *et al.* [63] added some surfactants in CNT/epoxy composites to assist the dispersion of CNTs. Experimental results showed that CNTs were dispersed more evenly with the aid of the surfactant, and the elastic modulus of the composites was increased by more than 30%. Nevertheless, CNTs treated by different surfactants may decrease the contact between CNTs, and thereby reduce the conductive properties of CNT/polymer composites.

In recent years, an interesting and successful non-covalent measure to obtain well-dispersed CNT/polymer composites was developed by establishing 'π-cation'. Bellayer *et al.* [123] prepared well-dispersed MWNT/PS composites by melt extrusion, using trialkylimidazolium tetrafluoroborate-compatibilized MWNTs. Evidence for a 'π-cation' interaction between the CNT and imidazolium was found. In addition, the use of imidazolium salts in controlling the dispersion of SWNT was also reported [124]. Kodgire *et al.* [95] prepared for the first time CNT/PA6 composites through specific interactions between Na-AHA, which assisted debundling the MWNT and leading to homogeneous dispersion within matrix during melt-mixing. The composite fabricated by this route exhibited low electrical percolation threshold of 0.5 wt% at room temperature, the lowest reported value in this system so far. Reactive coupling was found to be a dominant factor besides 'π-cation' interaction in achieving low electrical percolation in MWNT/PA6 composites.

It is worthy to mention the other efforts of synthesizing hybrid multi-scale reinforcement such as CNTs on carbon fibers [125–131] or on different ceramic particles [132]. In this case, CNTs can be homogeneously dispersed at microscale in the matrix with the help of these microscale carbon fibers or ceramic 'vehicle' because the microscale reinforcements can be much easily handled [132].

4.3. Interfacial interaction between CNTs and polymer matrix

Achieving suitable CNT-matrix interfacial bonding that provides effective stress transfer is another critical challenge for fabrication of CNT based polymer composites, especially for CNT/polymer structural composites. There are three main possible mechanisms of load transfer from a matrix to a reinforcement. The first is the weak van der Waals bonding between the reinforcement and the matrix, which is the main load transfer mechanism for CNT/polymer composites. In this case, interfacial energies normally amount to ~50–350 mJ/m^2 [133]. The second is micromechanical interlocking, which can be marginal in CNT/polymer composites if the CNTs have atomically smooth surface. The third is chemical bonding between CNTs and matrix, which is not guaranteed in many cases.

It is possible to enhance the load transfer from a matrix to a reinforcement by different treatments to improve the mechanical performance of the composite, based on the above three main mechanisms of load transfer. The van der Waals bonding can be increased by using small size reinforcement and close contact at the interface. From this point of view, individual SWNTs well dispersed in a matrix is helpful. In the case of the micromechanical interlocking between CNTs and the matrix's molecular chains, it seems that the ideal situation is that: CNTs are strong enough and inter-connected or long enough to block the movement of the polymer chains [34, 134]. The contribution of this mechanism may reach saturation at a relatively low CNT content [134]. It is unclear at this stage whether or not this critical content depends on the CNT orientation in the matrix. The chemical bonding between CNTs and matrices can be enhanced or created by surface treatments such as controlled oxidization, surface functionalization and physical coating. The question is whether or not such surface modification induces damage to the mechanical properties of the CNTs. The surface modification of the oxidized MWNTs was achieved by refluxing MWNTs with multi-functional amines by Gojny *et al.* [19] The TEM images of functionalized CNTs in the epoxy resin showed that CNTs were completely covered by the matrix. Telescopic pull-outs showed the outermost layer, which was directly bonded to the matrix, remained in the matrix, while the inner-tubes bridged the crack. All these results substantiate the evidence of improved interaction between CNTs and matrix.

Molecular dynamic simulation results given by Frankland *et al.* [135] showed that chemical cross-links between SWNTs and polymer matrix could increase the shear strength of the SWNT-polymer interface by over an order of magnitude in comparison to the weak nonbonded interactions. Wagner *et al.* [136] examined stress-induced fragmentation of MWNTs in a polymer matrix. From the estimated values of CNT axial normal stress and elastic modulus, they concluded that the interfacial shear strength of CNT/polymer composites was at the order of 500 MPa. Wagner also calculated the interfacial shear strength of SWNT/polymer composites using a traditional force balance approach modified for a hollow tube, and examined the effect by varying some of the model parameters [137]. It was shown that high values of the interfacial shear strength (compared to those in current advanced fiber based polymer composites) were attainable. Cooper *et al.* [138] quantified the interfacial interaction between CNTs and epoxy matrix by detaching individual SWNT bundles and MWNTs from the epoxy matrix using a scanning probe microscope tip. The values for the interfacial shear strength were determined varying from 35 to 376 MPa. These results from both experimental measurements and theoretical simulations show that high values (up to several hundreds of MPa under certain conditions) of the interfacial interaction between CNTs and polymer matrices are in principle attainable.

4.4. Contacts between individual CNTs

As mentioned in sections 4.2 and 4.3, surface treatment generally is used to improve CNT dispersion within the matrix and interfacial interaction between CNTs and matrix and it is very efficient to enhance the mechanical properties of the composite. However, surface treatment is adverse to a CNT/polymer functional composite in many cases. As we know, surface functionalization may disrupt the bonding between graphene sheets, and thereby reduce the intrinsic properties of CNTs in the final composites. Also, CNTs treated by different surfactants may decrease the contact between CNTs, and thereby reduce the final conductive properties of CNT/polymer composites. In fact, for a CNT/polymer functional composite, especially for an electric conducting composite, the effective conducting CNT path is primary, and good contact between individual CNTs is more important. An existing CNT conducting path does not guarantee good conductivity if the contact resistance between the individual CNTs is too high. Only when excellent electrical or thermal contact is established between the individual CNTs, the good electrical, thermal, wave or some other signals can be well transmitted. Several main factors may influence the contact resistance between CNTs, which finally determines the transport properties of CNT conducting path. The first is the intrinsic transport properties of CNTs, surface treatment for CNTs, therefore, is not desirable. The second is the orientation of CNTs within the matrix and the way that one CNT contacts with the others, overlap, end to end, one to one or one to more. The third is an insulating layer coating around CNT as well as its possible thickness, which is determined by the type of CNTs or polymers, the surface treatment of CNTs, and the processing method of the composites. Based on these analyses, it is possible to decrease the contact resistivity and improve the transport properties between individual CNTs by some measures. At first, high temperature treatment for CNTs to improve their intrinsic transport properties through improving their structural integrity and reducing the functional groups on their surface is preferable. To design and construct the contact means between CNTs by adjusting the content and orientation of CNTs within a matrix is also an effective measure. For example, to avoid the effect of contact resistance caused by the overlaps of CNTs in CNT passage, Huang *et al.* [113] proposed an ideal CNT composite structure, in which all the CNTs embedded in the matrix are aligned form one surface to the opposite side with all the CNT tips revealed on both surfaces. Another method is to weaken interfacial interaction between CNTs and matrix in order to decrease the interfacial interaction and then the quantity and quality of the polymer coating around CNTs during the processing of the composites [112, 139]. From this view of point, CNT/polymer functional composites may be applied in practice before CNT/polymer structural composites since it is very difficult to improve interfacial interaction between CNTs and matrix but do not damage the intrinsic structure and the mechanical properties of CNTs.

4.5. Other problems

Besides above discussions, a few other problems exist for applied research of CNT/polymer composites. For instance, it is important to avoid interlayer slippage within MWNTs and slippage within SWNT bundles in order to fully take advantage of extra-high mechanical properties of CNTs in composites. Because interlayer slippage is an inherent structural property of MWNTs, no effective method has been found to solve this problem. This becomes even more critical when the outer layers of MWNTs are discontinuous. We know that no interlayer slippage can occur in SWNTs because they only have one shell. However, the slippage within SWNT bundles can also decrease the performance of CNT/polymer composites. Thus, isolation of individual SWNTs may be highly desirable. However, the binding energy of SWNTs in a bundle is high enough so that separation of SWNTs by polymer infiltration in the melt seems unlikely, unless some external force, such as that from ultrasonication for example, is utilized. In addition, the good CNT orientation gives rise to CNT/polymer composites with higher electrical conductivity and mechanical reinforcement, control of the alignment of CNTs towards the pre-determined direction, therefore, becomes another important issue for the design of these composites.

5. Conclusions

This article reviewed the present status of CNT/polymer composites. Based on the results reported up to now, CNTs are promising for fabricating both structural and functional composites which can be widely used in various important fields. However, it is obvious that the potential as reinforcing fillers in polymers especially for CNT/polymer structural composites have not been fully brought into play. The state-of-art indicates that great efforts should be continuously made before widely employing these advanced composites into practical usage. The critical challenges lie in how to prepare structure-controllable CNTs with high purity, geometrical identity and consistently dependable high performance, how to break up CNT products to obtain isolated CNTs, how to fabricate composites with uniformly dispersed CNTs, and then how to enhance load transfer from a matrix to CNT reinforcement, etc. Scientists in different fields are worming their way to improve the status by innovative chemical techniques for CNT treatment and processing techniques for CNTs and CNT/polymer composites. Nevertheless, CNT/polymer composites present significant opportunities to basic science and nanotechnology, and pose significant challenges for future work in nanocomposite field.

Acknowledgements

This work was supported by the National Natural Science Foundation of China (No. 90606008) and by Chinese Academy Sciences. The support of the PICS (Programme International de Coopération Scientifique CNRS No. 3358, J. B. Bai & H. M. Cheng) is also acknowledged. The authors sincerely thank Dr. Xiu-Juan He, Xin Tong, Zhe Ying, You Zeng and Shuo Bai for their valuable discussions.

Glossary of abbreviation and symbols used in this article

CB	carbon black
CNT	carbon nanotube
CP-NT	conducting polymer-carbon nanotube
SWNT	single-walled carbon nanotube
MWNT	multi-walled carbon nanotube
CNF	carbon nanofiber
PA6	polyamide-6
PA12	polyamide-12
PANI	polyaniline
PE	polyethylene
HDPE	high density polyethylene
UHMWPE	Ultrahigh molecular weight polyethylene
PEO	poly(ethylene oxide)
PET	poly(ethylene terephthalate)
PI	Polyimide
PMMA	poly(methyl methacrylate)
PmPV	poly(m-phenylenevinylene-co-2,5-dioctoxy-p-phenylenevinylene)
P3OT	poly(3-octylthiophene)
PP	polypropylene
PPA-C16TAB	poly(acrylic acid)-hexadecyltrimethy-ammonium bromide
PS	polystyrene

PVA	poly(vinyl alcohol)
PVC	polyvinyl chloride
PVDF	poly(vinylidene fluoride)
SPAN	sulfonated polyaniline
TPU	Thermoplastic polyurethane
AIBN	2, 2'-azobisisobutyronitrile
Na-AHA	sodium salt of 6-aminohexanoic acid
EMI	electromagnetic interference
ESD	electrostatic dissipation
NTC	negative temperature coefficient
PTC	positive temperature coefficient
TIM	thermal interface material
K	thermal conductivity
T_g	glass transition temperature
T_m	melting temperature
LBL	layer-by-layer

References

[1] Iijima S.: Heical microtubules of graphitic carbon. Nature, **354**, 56–58 (1991).

[2] Robertson D. H., Brenner D. W., Mintmire J. W.: Energetics of nanoscale graphitic tubules. Physical Review: B, **45**, 12592–12595 (1992).

[3] Yakobson B. I., Brabec C. J., Bernholc J.: Nanomechanics of carbon tubes: instabilities beyond linear response. Physical Review Letters, **76**, 2511–2514 (1996).

[4] Lu J. P.: Elastic properties of carbon nanotubes and nanoropes. Physical Review Letters, **79**, 1297–1300 (1997).

[5] Wong E. W., Sheehan P. E., Lieber C. M.: Nanobeam mechanics: elasticity, strength, and toughness of nanorods and nanotubes. Science, **277**, 1971–1975 (1997).

[6] Cornwell C. F., Wille L. T.: Elastic properties of single-walled carbon nanotubes in compression. Solid State Communications, **101**, 555–558 (1997).

[7] Kim P., Shi L., Majumdar A., McEuen P. L.: Thermal transport measurements of individual multiwalled nanotubes. Physical Review Letters, **87**, 215502 (2001).

[8] Collins P. G., Avouris P.: Nanotubes for electronics. Scientific American, **283**, 62–69 (2000).

[9] Weidenkaff A., Ebbinghaus S. G., Mauron P., Reller A., Zhang Y., Zuttel A.: Metal nanoparticles for the production of carbon nanotube composite materials by decomposition of different carbon sources. Materials Science and Engineering: C-Biomimetic and Supramolecular Systems, **19**, 119–123 (2002).

[10] Chen W. X., Tu J. P., Wang L. Y., Gan H. Y., Xu Z. D., Zhang X. B.: Tribological application of carbon nanotubes in a metal-based composite coating and composites. Carbon, **41**, 215–222 (2003).

[11] Tu J. P., Yang Y. Z., Wang L. Y., Ma X. C., Zhang X. B.: Tribological properties of carbon nanotube reinforced copper composites. Tribology Letters, **10**, 225–228 (2001).

[12] Dong S. R., Tu J. P., Zhang X. B.: An investigation of the sliding wear behavior of Cu-matrix composite reinforced by carbon nanotubes. Materials Science and Engineering: A, **313**, 83–87 (2001).

[13] An J. W., Lim D. S.: Synthesis and characterization of alumina/carbon nanotube composite powders. Journal of Ceramic Processing Research, **3**, 174–177 (2002).

[14] Zhao L. P., Gao L.: Novel in situ synthesis of MWNTs-hydroxyapatite composites. Carbon, **42**, 423–426 (2004).

[15] Xia Z., Riester L., Curtin W. A., Li H., Sheldon B. W., Liang J., Chang B., Xu J. M.: Direct observation of toughening mechanisms in carbon nanotube ceramic matrix composites. Acta Materialia, **52**, 931–944 (2004).

[16] Rul S., Lefevre-Schlick F., Capria E., Laurent C., Peigney A.: Percolation of single-walled carbon nanotubes in ceramic matrix nanocomposites. Acta Materialia, **52**, 1061–1067 (2004).

[17] Sandler J., Shaffer M. S. P., Prasse T., Bauhofer W., Schulte K., Windle A. H.: Development of a dispersion process for carbon nanotubes in an epoxy matrix and the resulting electrical properties. Polymer, **40**, 5967–5971 (1999).

[18] Schadler L. S., Giannaris S. C., Ajayan P. M.: Load transfer in carbon nanotube epoxy composites. Applied Physics Letters, **73**, 3842–3844 (1998).

[19] Gojny F. H., Nastalczyk J., Roslaniec Z., Schulte K.: Surface modified multi-walled carbon nanotubes in CNT/epoxy-composites. Chemical Physics Letters, **370**, 820–824 (2003).

[20] Jia Z. J., Wang Z., Xu C., Liang J., Wei B. Q., Wu D., Zhu S.: Study on poly(methyl methacrylate)/carbon nanotube composites. Materials Science and Engineering: A, **271**, 395–400 (1999).

[21] De le Chapelle M. L., Stéphan C., Nguyen T. P., Lefrant S., Journet C., Bernier P., Munoz E., Benito A., Maser W. K., Martinez M. T., de la Fuente G. F., Guillard T., Flamant G., Alvarez L., Laplaze D.: Raman characterization of single-walled carbon nanotubes-PMMA composites. Synthetic Metals, **103**, 2510–2512 (1999).

[22] Haggenmueller R., Gommans H. H., Rinzler A. G., Fischer J. E., Winey K. I.: Aligned single-wall carbon nanotubes in composites by melt processing methods. Chemical Physics Letters, **330**, 219–225 (2000).

[23] Shaffer M. S. P., Windle A. H.: Fabrication and characterization of carbon nanotubes/poly(vinyl alcohol) composites. Advanced Materials, **11**, 937–941 (1999).

[24] Li F., Cheng H. M., Bai S., Su G., Dresselhaus M. S.: Tensile strength of single-walled carbon nanotubes directly measured from their macroscopic ropes. Applied Physical Letters, **77**, 3161–3163 (2000).

[25] Dalton A. B., Collins S., Munoz E., Razal J. M., Ebron V. H., Ferraris J. P., Coleman J. N., Kim B. G., Baughman R. H.: Super-tough carbon-nanotube fibres. Nature, **423**, 703 (2003).

[26] Kumar S., Doshi H., Srinivasarao M., Park J. O., Schiraldi D. A.: Fiber from polypropylene/nano carbon fiber composites. Polymer, **43**, 1701–1703 (2002).

[27] Valentini L., Biagiotti J., Kenny J.M., Santucci S.: Morphological characterization of single-walled carbon nanotubes-PP composites. Composites Science and Technology, **63**, 1149–1153 (2003).

[28] Tibbetts G. G., McHugh J. J.: Mechanical properties of vapor-grown carbon fiber composites with thermoplastic matrices. Journal of Materials Research, **14**, 2871–2880 (1999).

[29] Tong X., Liu C., Cheng H. M., Zhao H. C., Yang F., Zhang X. Q.: Surface modification of single-walled carbon nanotubes with polyethylene via in situ Ziegler-Natta polymerization. Journal of Applied Polymer Science, **92**, 3697–3700 (2004).

[30] Lozano K., Yang S. Y., Jones R. E.: Nanofiber toughened polyethylene composites. Carbon, **42**, 2329–2331 (2004).

[31] Sandler J. K. W., Pegel S., Cadek M., Gojny F., van Es M., Lohmar J., Blau W. J., Schulte K., Windle A. H., Shaffer M. S. P.: A comparative study of melt spun polyamide-12 fibres reinforced with carbon nanotubes and nanofibres. Polymer, **45**, 2001–2015 (2004).

[32] Hill D. E., Lin Y., Rao A. M., Allard L. F., Sun Y. P.: Functionalization of carbon nanotubes with polystyrene. Macromolecules, **35**, 9466–9471 (2002).

[33] Liao K., Seam L. I.: Interfacial characteristic of a carbon nanotubes-polystyrene composite system. Applied Physics Letters, **79**, 4225–4227 (2001).

[34] Bai J. B., Allaoui A.: Effect of the length and the aggregate size of MWNTs on the improvement efficiency of the mechanical and electrical properties. Compsites: Part A, **34**, 689–694 (2003).

[35] Cadek M., Coleman J. N., Barron V., Hedicke K., Blau W. J.: Morphological and mechanical properties of carbon-nanotube-reinforced semicrystalline and amorphous polymer composites. Applied Physics Letters, **81**, 5123–5125 (2002).

[36] Cooper C. A., Ravich D., Lips D., Mayer J., Wagner H. D.: Distribution and alignment of carbon nanotubes and nanofibrils in a polymer matrix. Composites Science and Technology, **62**, 1105–1112 (2002).

[37] Xu X. J., Thwe M. M., Shearwood C., Liao K.: Mechanical properties and interfacial characteristics of carbon-nanotube-reinforced epoxy thin films. Applied Physics Letters, **81**, 2833–2835 (2002).

[38] Lau K. T., Shi S. Q., Cheng H. M.: Micro-mechanical properties and morphological observation on fracture surfaces of carbon nanotube composites pre-treated at different temperatures. Composites Science and Technology, **63**, 1161–1164 (2003).

[39] Mamedov A. A., Kotov N., Prato M., Guldi D. M., Wicksted J. P., Hirsch A.: Molecular design of strong single-wall carbon nanotube/polyelectrolyte multiplayer composites. Nature Materials, **1**, 190–194 (2002).

[40] Carneiro O. S., Maia J. M.: Rheological behavior of (short) carbon fiber/thermoplastic composites. Part I: The Influence of fiber type, processing conditions and level of incorporation, Polymer Composites, **21**, 960–969 (2000).

[41] Shaffer M. S. P., Sandler J. K. W.: Carbon nanotube/nanofibre polymer composites. in 'Processing and properties of nanocomposites' (ed.: Advani S. G.) World Scientific, New York, 1–60, (2006).

[42] Jin Z. X., Pramoda K. P., Xu G. Q., Goh S. H.: Dynamic mechanical behavior of melt-processed multi-walled carbon nanotube/poly(methyl methacrylate) composites. Chemical Physics Letters, **337**, 43–47 (2001).

[43] Du J. H., Ying Z., Bai S., Li F., Sun C., Cheng H. M.: Microstructure and resistivity of carbon nanotube and nanofiber/epoxy matrix nanocomposites. International Journal of Nanoscience, **1**, 719–723 (2002).

[44] Ying Z., Du J. H., Bai S., Li F., Liu C., Cheng H. M.: Mechanical properties of surfactant-coating carbon nanofiber/epoxy composite. International Journal of Nanoscience, **1**, 425–430 (2002).

[45] Du J. H.: Electromagnetic properties and microwave absorption characteristics of fibrous nano-carbon materials and their composites. PhD Thesis, Institute of Metal Research, Chinese Academy of Sciences, Shenyang, (2003).

[46] Li X. H., Wu B., Huang J., Zhang J., Liu Z. F., Li H. L.: Fabrication and characterization of well-dispersed single-walled carbon nanotube/polyaniline composites. Carbon, **41**, 1670–1673 (2002).

[47] Feng W., Bai X. D., Lian Y. Q., Liang J., Wang X. G., Yoshino K.: Well-aligned polyaniline/carbon-nanotube composite films grown by in-situ aniline polymerization. Carbon, **41**, 1551–1557 (2003).

[48] Andrew R., Jacques D., Rao A. M., Rantell T., Derbyshire F., Chen Y., Chen J., Haddon R. C.: Nanotube composite carbon fibers. Applied Physics Letters, **75**, 1329–1331 (1999).

[49] Vigolo B., Pénicaud A., Coulon C., Sauder C., Pailler R., Journet C., Bernier P., Poulin P.: Macroscopic fibers and ribbons of oriented carbon nanotubes. Science, **290**, 1331–1334 (2000).

[50] Bhattacharyya A. R., Sreekumar T. V., Liu T., Kumar S., Ericson L. M., Hauge R. H., Smalley R. E.: Crystallization and orientation studies in polypropylene/single wall carbon nanotube composite. Polymer, **44**, 2373–2377 (2003).

[51] Ajayan P. M., Stephan O., Colliex C., Trauth D.: Aligned carbon nanotube arrays formed by cutting a polymer resin-nanotube composite. Science, **265**, 1212–1214 (1994).

[52] Jin L., Bower C., Zhou O.: Alignment of carbon nanotubes in a polymer matrix by mechanical stretching. Applied Physics Letters, **73**, 1197–1199 (1998).

[53] Bower C., Rosen R., Jin L., Han J., Zhou O.: Deformation of carbon nanotubes in nanotube-polymer composites. Applied Physics Letters, **74**, 3317–3319 (1999).

[54] Kimura T., Ago H., Tobita M., Ohshima S., Kyotani M., Yumura M.: Polymer composites of carbon nanotubes aligned by a magnetic field. Advanced Materials, **14**, 1380–1383 (2002).

[55] Sen R., Zhao B., Perea D., Itkis M. E., Hu H., Love J., Bekyarova E., Haddon R. C.: Preparation of single-walled carbon nanotube reinforced polystyrene and polyurethane nanofibers and membranes by electrospinning. Nano Letters, **4**, 459–464 (2004).

[56] Gao M., Huang S., Dai L., Wallace G., Gao R., Wang Z. L.: Aligned coaxial nanowires of carbon nanotubes sheathed with conducting polymers. Angewandte Chemie, **39**, 3664–3667 (2000).

[57] Shofner M. L., Rodríguez-Macías F. J., Vaidyanathan R., Barrera E. V.: Single wall nanotube and vapor grown carbon fiber reinforced polymers processed by extrusion freeform fabrication. Composites: Part A, **34**, 1207–1217 (2003).

[58] Coleman J. N., Khan U., Blau W. J., Gun'ko Y. K.: Small but strong: A review of the mechanical properties of carbon nanotube-polymer composites. Carbon, **44**, 1624–1652 (2006).

[59] Baughman R. H., Zakhidov A. A., de Heer W. A.: Carbon nanotubes-the route toward applications. Science, **297**, 787–792 (2002).

[60] Lau K. T., Hui D.: Effectiveness of using carbon nanotubes as nano-reinforcements for advanced composite structures. Carbon, **40**, 1605–1606 (2002).

[61] Lau K. T.: Interfacial bonding characteristics of nanotube/polymer composites. Chemical Physics Letters, **370**, 399–405 (2003).

[62] Calvert P.: A recipe for strength. Nature, **339**, 210–211 (1999).

[63] Davey A. P., Coleman J., Dalton A., Maier S., Drury A., Gray D., Brennan M., Ryder K., Lamy De La Chapelle M., Journet C., Bernier P., Carroll D., Blau W., Byrne H. J., Ajayan P. M., Lefrant S.: Evolution and evaluation of the polymer/nanotube composite. Synthetic Metals, **103**, 2559–2562 (1999).

[64] Ajayan P. M., Schandler L. S., Gianaris C., Rubio A.: Single-walled carbon nanotube-polymer composites: strength and weakness. Advanced Materials, **12**, 750–753 (2000).

[65] Gong X. Y., Liu J., Baskaran S., Voise R. D., Young J. S.: Surfactant-assisted processing of carbon nanotube/polymer composites. Chemistry of Materials, **12**, 1049–1052 (2000).

[66] Andrews R., Jacques D., Minot M., Rantell T.: Fabrication of carbon multiwall nanotube/polymer composites by shear mixing. Macromolecular Materials and Engineering, **287**, 395–403 (2002).

[67] Zhang Q., Rastogi S., Chen D., Lippits D., Lemstra P. J.: Low percolation threshold in single-walled carbon nanotube/high density polyethylene composites prepared by melt processing technique. Carbon, **44**, 778–785 (2006).

[68] Qian D., Dickey E. C., Andrews R., Rantell T.: Load transfer and deformation mechanisms in carbon nanotube-polystyrene composites. Applied Physics Letters, **76**, 2868–2870 (2000).

[69] Jin Z. X., Pramoda K. P., Goh S. H., Xu G. Q.: Poly(vinylidene fluoride)-assisted melt-blending of multi-walled carbon nanotube/poly(methyl methacrylate) composite. Materials Research Bulletin, **37**, 271–278 (2002).

[70] Geng H. Z., Rosen R., Zheng B., Shimoda H., Fleming L., Liu J., Zhou O.: Fabrication and properties of composites of poly(ethylene oxide) and functionalized carbon nanotubes. Advanced Materials, **14**, 1387–1390 (2002).

[71] Paiva M. C., Zhou B., Fernando K. A. S., Lin Y., Kennedy J. M., Sun Y. P., Mechanical and morphological characterization of polymer-carbon nanocomposites from functionalized carbon nanotubes. Carbon, **42**, 2849–2854 (2004).

[72] Siochi E. J., Working D. C., Park C., Lillehei P. T., Rouse J. H., Topping C. C., Bhattacharyya A. R., Kumar S.: Melt processing of SWCNT-polyimide nanocomposite fibers. Composites: Part B, **35**, 439–446 (2004).

[73] Chen W., Tao X. M.: Production and characterization of polymer nanocomposite with aligned single wall carbon nanotubes. Applied Surface Science, **252**, 3547–3552 (2006).

[74] Ruan S., Gao P., Yu T. X.: Ultra-strong gel-spun UHMWPE fibers reinforced using multiwalled carbon nanotubes. Polymer, **47**, 1604–1611 (2006).

[75] Meguid S. A., Sun Y.: On the tensile and shear strength of nano-reinforced composite interfaces. Materials and Design, **25**, 289–296 (2004).

[76] Shaffer M., Kinloch I. A.: Prospects for nanotube and nanofiber composites. Composites Science and Technology, **64**, 2281–2282 (2004).

[77] Ruan S. L., Gao P., Yang X. G., Yu T. X.: Toughening high performance ultrahigh molecular weight polyethylene using multiwalled carbnon nanotubes. Polymer, **44**, 5643–5654 (2003).

[78] Andrews R., Weisenberger M. C.: Carbon nanotube polymer composites. Current Opinion in Solid State & Materials Science , **8**, 31–37 (2004).

[79] Vollrath F. Knight D. P.: Liquid crystalline spinning of spider silk. Nature, **410**, 541–548 (2001).

[80] Ogando J.: Nanotech goes to bat: Carbon nanotubes boost bat performance. Design News, Issue 8: The sport page, June 5 (2006).

[81] Martin C. A., Sandler J. K. W., Shaffer M. S. P., Schwarz M. K., Bauhofer W., Schulte K., Windle A. H.: Formation of percolating networks in multi-wall carbon-nanotube-epoxy composites. Composites Science and Technology, **64**, 2309–2316 (2004).

[82] Zhu B. K., Xie S. H., Xu Z. K., Xu Y. Y.: Preparation and properties of the polyimide/multi-walled carbon nanotubes (MWNTs) nanocomposites. Composites Science and Technology, **66**, 548–554 (2006).

[83] Sandler J. K. W., Kirk J. E., Kinloch I. A., Shaffer M. S. P., Windle A. H.: Ultra-low electrical percolation threshold in carbon-nanotube-epoxy composites. Polymer, **44**, 5893–5899 (2003).

[84] Allaoui A., Bai S., Cheng H. M., Bai J. B.: Mechanical and electrical properties of a MWNT/epoxy composite. Composites Science and Technology, **62**, 1993–1998 (2002).

[85] Dufresne A., Paillet M., Putaux J. L., Canet R., Carmona F., Delhaes P., Cui S.: Processing and characterization of carbon nanotube/poly(styrene-co-butyl acrylate) nanocomposites. Journal of Material Science, **37**, 3915–3923 (2002).

[86] Barraza H. J., Pompeo F., O'Rear E. A., Resasco D. E.: SWNT-Filled Thermoplastic and Elastomeric Composites Prepared by Miniemulsion Polymerization. Nano Letters, **2**, 797–802 (2002).

[87] McNally T., Pötschke P., Halley P., Murphy M., Martin D., Bell S. E. J., Brennan G. P., Bein D., Lemoine P., Quinn J. P: Polyethylene multiwalled carbon nanotube composites. Polymer, **46**, 8222–8232 (2005).

[88] Hu G., Zhao C., Zhang S., Yang M., Wang Z.: Low percolation thresholds of electrical conductivity and rheology in poly(ethylene terephthalate) through the networks of multi-walled carbon nanotubes. Polymer, **47**, 480–488 (2006).

[89] Seo M. K., Park S. J.: Electrical resistivity and rheological behaviors of carbon nanotubes-filled polypropylene composites. Chemical Physics Letters, **395**, 44–48 (2004).

[90] Seo M. K., Lee J. R., Park S. J.: Crystallization kinetics and interfacial behaviors of polypropylene composites reinforced with multi-walled carbon nanotubes. Materials Science and Engineering: A, **404**, 79–84 (2005).

[91] Tchmutin I. A., Ponomarenko A. T., Krinichnaya E. P., Kozub G. I., Efimov O. N.: Electrical properties of composites based on conjugated polymers and conductive fillers. Carbon, **41**, 1391–1395 (2003).

[92] Meincke O., Kaempfer D., Weickmann H., Friedrich C., Vathauer M., Warth H.: Mechanical properties and electrical conductivity of carbon-nanotube filled polyamide-6 and its blends with acrylonitrile/butadiene/styrene. Polymer, **45**, 739–748 (2004).

[93] Coleman J. N., Curran S., Dalton A. B., Davey A. P., McCarthy B., Blau W., Barklie R. C.: Percolation-dominated conductivity in a conjugated-polymer-carbon-nanotube composite. Physical Review B, **58**, 7492–7495 (1998).

[94] Kymakis E., Alexandou I., Amaratunga G. A. J.: Single-walled carbon nanotube-polymer composites: electrical, optical, and structural investigation. Synthetic Metals, **127**, 59–62 (2002).

[95] Kodgire P. V., Bhattacharyya A. R., Bose S., Gupta N., Kulkarni A. R., Misra A.: Control of multiwall carbon nanotubes dispersion in polyamide 6 matrix: An assessment through electrical conductivity. Chemical Physics Letters, **432**, 480–485 (2006).

[96] He X. J., Du J. H., Ying Z., Cheng H. M.: Positive temperature coefficient effect in multiwalled carbon nanotube/high-density polyethylene composites. Applied Physics Letters, **86**, 062112/1–062112/3 (2005).

[97] Berber S., Kwon Y-K., Tománek D.: Unusually high thermal conductivity of carbon nanotubes. Physical Review Letters, **84**, 4613–4616 (2000).

[98] Kim P., Shi L., Majumdar A., McEuen P. L.: Thermal transport measurements of individual multi-walled nanotubes. Physical Review Letters, **87**, 215502–215505 (2000).

[99] Kashiwagi T., Grulke E., Hilding J., Harris R., Awad W., Douglas J. F.: Thermal degradation and flammability properties of poly(prorylene)/carbon nanotube composites. Macromolecular Rapid Communications, **23**, 761–765 (2002).

[100] Du F. M., Fischer J. E., Winey K. I.: Coagulation method for preparing single-walled carbon nanotube/poly(methyl methacrylate) composites and their modulus, electrical conductivity, and thermal stability. Journal of Polymer Science: Part B. Polymer Physics, **41**, 3333–3338 (2003).

[101] Wei C. Y., Srivastava D., Cho K.: Thermal expansion and diffusion coefficients of carbon nanotube-polymer composites. Nano Letters, **2**, 647–650 (2002).

[102] Biercuk M. J., Llaguno M. C., Radosavljevic M., Hyun J. K., Johnson A. T., Fischer J. E.: Carbon nanotube composites for thermal management. Applied Physics Letters, **80**, 2767–2769 (2002).

[103] Xu Y. S., Ray G., Abdel-Magid B.: Thermal behavior of single-walled carbon nanotube polymer-matrix composites. Composites: Part A, **37**, 114–121 (2006).

[104] Thostenson E., Chou T-W.: Processing-structure-multi-functional property relationship in carbon nanotube/epoxy composites. Carbon, **44**, 3022–3029 (2006).

[105] Liu C. H., Huang H., Wu Y., Fan S. S.: Thermal conductivity improvement of silicone elastomer with carbon nanotube loading. Applied Physics Letters, **84**, 4248–4250 (2004).

[106] Shenogin S., Xue L., Ozisik R., Keblinski P., Cahill D. G.: Role of thermal boundary resistance on the heat flow in carbon-nanotube composites. Journal of Applied Physics, **95**, 8136–8144 (2004).

[107] Huxtable S. T., Cahill D. G., Shenogin S., Xue L. P., Ozisik R., Barone P., Usrey M., Strano M. S., Siddons G., Shim M., Keblinski P.: Interfacial heat flow in carbon nanotube suspensions. Nature Materials, **2**, 731–734 (2003).

[108] Nan C. W., Liu G., Lin Y., Li M.: Interface effect on thermal conductivity of carbon nanotube composites. Applied Physics Letters, **85**, 3549–3551 (2004).

[109] Bagchi A., Nomura S.: On the effective thermal conductivity of carbon nanotube reinforced polymer composites. Composites Science and Technology, **66**, 1703–1712 (2006).

[110] Shenogin S., Bodapati A., Xue L., Ozisik R., Keblinski P.: Effect of chemical functionalization on thermal transport of carbon nanotube composites. Applied Physics Letters, **85**, 2229–2231 (2004).

[111] Liu C. H., Fan S. S.: Effects of chemical modifications on the thermal conductivity of carbon nanotube composites. Applied Physics Letters, **86**, 123106/1–123106/3 (2005).

[112] Gojny F. C., Wichmann M. H. G., Fiedler B., Kinloch I. A., Bauhofer W., Windle A. H., Schulte K.: Evaluation and identification of electrical and thermal conduction mechanisms in carbon nanotube/epoxy composites. Polymer, **47**, 2036–2045 (2006).

[113] Huang H., Liu C., Wu Y., Fan S. S.: Alighed carbon nanotube composite films for thermal management. Advanced Materials, **17**, 1652–1656 (2005).

[114] Wu Y., Liu C.H., Huang H., Fan S. S.: Effects of surface metal layer on the thermal contact resistance of carbon nanotube arrays. Applied Physics Letters, **87**, 213108/1–213108/3 (2005).

[115] Jin Z. X., Huang L., Goh S. H., Xu G. Q., Ji W.: Characterization and nonlinear optical properties of a poly(acryli acid)-surfactant-multi-walled carbon nanotube complex. Chemical Physics Letters, **322**, 461–566 (2000).

[116] Jin Z. X., Sun X., Xu G., Goh S. H., Ji W.: Nonlinear optical properties of some polymer/multi-walled carbon nanotube composites. Chemical Physics Letters, **318**, 505–510 (2000).

[117] Chen Y. C., Raravikar N. R., Schadler L. S., Ajayan P. M., Zhao Y. P., Lu T. M., Wang G. C., Zhang X. C.: Ultrafast optical switching properties of single-wall carbon nanotube polymer composites at 1.55 m. Applied Physics Letters, **81**, 975–977 (2002).

[118] Fan Z. J., Luo G. H., Zhang Z. F., Zhou L., Wei F.: Electromagnetic and microwave absorbing properties of multi-walled carbon nanotubes/polymer composites. Materials Science and Engineering: B, **132**, 85–89 (2006).

[119] Wei Z. X., Wan M. X., Lin T., Dai L. M.: Polyaniline nanotubes doped with sulfonated carbon nanotubes made a self-assembly process. Advanced Materials, **15**, 136–139 (2003).

[120] Zhang H., Li H. X., Cheng H. M.: Water-Soluble Multiwalled Carbon Nanotubes Functionalized with Sulfonated Polyaniline. The Journal of Physical Chemistry: B, **110**, 9095–9099 (2006).

[121] Valentini L., Kenny J. M.: Novel approaches to developing carbon nanotube based polymer composites: fundamental studies and nanotech applications. Polymer, **46**, 6715–6718 (2005).

[122] Thostenson E. T., Ren Z. F., Chou T. W.: Advances in the science and technology of carbon nanotubes and their composites: a review. Composites Science and Technology, **61**, 1899–1912 (2001).

[123] Bellayer S., Gilman J. W., Eidelman N., Bourbigot S., Flambard X., Fox D. M., De Long H. C., Trulove P. C.: Preparation of homogeneously dispersed multiwalled carbon nanotube/polystyrene nanocomposites via melt extrusion using trialkyl imidazolium compatibilizer. Advanced Functional Materials, **15**, 910–916 (2005).

[124] Fukushima T., Kosaka A., Ishimura Y., Yamamoto T., Takigawa T., Ishii N., Aida T.: Molecular ordering of organic molten salts triggered by single-walled carbon nanotubes. Science, **300**, 2072–2074 (2003).

[125] Otsuka K., Abe Y., Kanai N., Kobayashi Y., Takenaka S., Tanabe E.: Synthesis of carbon nanotubes on Ni/carbon-fiber catalysts under mild conditions. Carbon, **42**, 727–736 (2004).

[126] Zhu S., Su C. H., Lehoczky S. L., Muntele I., Ila D.: Carbon nanotube growth on carbon fibers. Diamond and Related Materials, **12**, 1825–1828 (2003).

[127] Wei B. Q., Vajtai R., Ajayan P. M.: Sequence growth of carbon fibers and nanotube networks by CVD process. Carbon, **41**, 185–188 (2003).

[128] Smiljanic O., Dellero T., Serventi A., Lebrun G., Stansfield B. L., Dodelet J. P., Trudeau M., Désilets S.: Growth of carbon nanotubes on ohmically heated carbon paper. Chemical Physics Letters, **342**, 503–509 (2001).

[129] Thostenson E. T., Li W. Z., Wang D. Z., Ren Z. F., Chou T. W.: Carbon nanotube/carbon fiber hybrid multiscale composites. Journal of Applied Physics, **91**, 6034–6037 (2002).

[130] Ci L. J., Zhao Z. G., Bai J. B.: Direct growth of aligned carbon nanotubes on the surface of ceramic fibers. Carbon, **43**, 883–886 (2005).

[131] Zhao Z. G., Ci L. J., Cheng H. M., Bai J. B.: Growth of multi-walled carbon nanotube of different morphologies on carbon fibres by floating catalyst method. Carbon, **43**, 663–665 (2004).

[132] Ci L. J. Bai J. B.: Novel micro/nanoscale hybrid reinforcement: multi-walled carbon nanotubes on SiC particles. Advanced Materials, **16**, 2021–2024 (2004).

[133] Nardin M., Schultz J.: Effect of elastic-moduli and interfacial adhesion energy on the critical fiber aspect ratio in single-fiber composites. Journal of Materials Science Letters, **12**, 1245–1247 (1993).

[134] Bai J. B.: Evidence of the reinforcement role of CVD multi-walled carbon nanotubes in a polymer matrix. Carbon, **41**, 1331–1334 (2003).

[135] Frankland S. J. V., Harik V. M.: Analysis of carbon nanotube pull-out from a polymer matrix. Surface Science, **525**, 103–108 (2003).

[136] Wagner H. D., Lourie O., Feldman Y., Tenne R.: Stress-induced fragmentation of multiwall carbon nanotubes in a polymer matrix. Applied Physics Letters, **72**, 188–190 (1998).

[137] Wagner H. D.: Nanotube-polymer adhesion: a mechanics approach. Chemical Physics Letters, **361**, 57–61 (2002).

[138] Cooper C. A., Cohen S. R., Barber A. H., Wagner H. D.: Detachment of nanotubes from a polymer matrix. Applied Physics Letters, **81**, 3873–3875 (2002).

[139] Zhang H.: PhD Thesis, Surface modification of carbon nanotubes and electrical properties of carbon nanotube composites. Institute of Metal Research, Chinese Academy of Sciences (2006).

Appendix: list of published review papers related to CNT/polymer composites

[A1] Gibson R. F., Ayorinde E. O., Wen Y. F.: Vibrations of carbon nanotubes and their composites: A review. Composite Science and Technology, **67**, 1–28, (2007).

[A2] Coleman J. N., Khan U., Blau W. J., Gun'ko Y. K.: Small but strong: A review of the mechanical properties of carbon nanotube-polymer composites. Carbon, **44**, 1624–1652 (2006).

[A3] Moniruzzaman M., Winey K. I.: Polymer nanocomposites containing carbon nanotubes. Macromolecules, **39**, 5194–5205 (2006).

[A4] Lau K. T., Gu C., Hui D.: A critical review on nanotube and nanotube/nanoclay related polymer composite materials. Composites: Part B, **37**, 425–436 (2006).

[A5] Coleman J. N., Khan U., Gun'ko Y. K.: Mechanical reinforcement of polymers using carbon nanotubes. Advanced Materials **18**, 689–706 (2006).

[A6] Liu P.: Modifications of carbon nanotubes with polymers. European Polymer Journal, **41**, 2693–2703 (2005).

[A7] Desai A. V., Haque M. A.: Mechanics of the interface for carbon nanotube-polymer composites. Thin-Walled Structures, **43**, 1787–1803 (2005).

[A8] Xie X. L., Mai Y. W. Zhou X. P.: Dispersion and alignment of carbon nanotubes in polymer matrix: A review. Materials Science and Engineering: R Reports, **49**, 89–112 (2005).

[A9] Chae H. G., Sreekumar T. V., Uchida T., Kumar S.: A comparison of reinforcement efficiency of various types of carbon nanotubes in polyacrylonitrile fiber. Polymer, **46**, 10925–10935 (2005).

[A10] Potschke P, Bhattacharyya A. R., Janke A., Goering H.: Composites of polycarbonate with multiwalled carbon nanotubes produced by melt mixing. ACS Symposium Series, **898**, 148–163 (2005).

[A11] Velasco-Santos C., Martinez-Hernandez A. L., Castano V. M.: Carbon nanotube-polymer nanocomposites: The role of interfaces. Composite Interfaces, **11**, 567–586 (2005).

[A12] Breuer O., Sundararaj U.: Big Returns From Small Fibers: A review of polymer/carbon nanotube composites. Polymer Composites, **25**, 630–645 (2004).

[A13] Andrews R., Weisenberger M. C: Carbon nanotube polymer composites. Current Opinion in Solid State & Materials Science, **8**, 31–37 (2004).

[A14] Harris P. J. F.: Carbon nanotube composites. International Materials Reviews, **49**, 31–43 (2004).

[A15] Li L. X., Li F., Ying Z., Yang Q. H., Cheng H. M.: Carbon nanotube/polymer functional composite. New Carbon Materials, **18**, 69–74 (2003).

[A16] Baughman R. H., Zakhidov A. A., Heer W. A.: Carbon nanotubes-the route toward applications. Science, **297**, 787–792 (2002).

[A17] Thostenson E. T., Ren Z., Chou T. W.: Advances in the science and technology of carbon nanotubes and their composites: a review. Composites Science and Technology, **61**, 1899–1912 (2001).

eXPRESS Polymer Letters Vol.1, No.5 (2007) 274–282
Available online at www.expresspolymlett.com
DOI: 10.3144/expresspolymlett.2007.40

Synthesis and ring-opening metathesis polymerization (ROMP) of new *N*-fluoro-phenylnorbornene dicarboximides by 2nd generation ruthenium alkylidene catalysts

J. Vargas[1], *A. A. Santiago*[1], *R. Gaviño*[2], *A. M. Cerda*[1], *M. A. Tlenkopatchev*[1]*

[1]Instituto de Investigaciones en Materiales, Universidad Nacional Autónoma de México, Apartado Postal 70-360, CU, Coyoacán, México DF 04510
[2]Instituto de Química, Universidad Nacional Autónoma de México, CU, Coyoacán, México DF 04510

Received 29 January 2007; accepted in revised form 9 April 2007

Abstract. The synthesis of new *N*-3,5-bis(trifluoromethyl)phenyl-*endo*-norbornene-5,6-dicarboximide (TFMPhNDI, **2a**), *N*-4-fluorophenyl-*endo*-norbornene-5,6-dicarboximide (FPhNDI, **2b**) and *N*-2,2,6,6-tetramethylpiperidyl-*endo*-norbornene-5,6-dicarboximide (TMPNDI, **2c**) monomers was carried out. Polynorbornene dicarboximides were obtained via ring opening metathesis polymerization (ROMP) using a second generation ruthenium alkylidene catalyst (1,3-dimesityl-4,5-dihydroimidazol-2-ylidene) ($PCy_3Cl_2Ru = CHPh$) (**I**). Poly-TMPNDI which bears a piperidyl moiety showed the highest T_g and T_d compared to the polymers bearing fluoro-aryl moieties. Thermal stability of Poly-TFMPhNDI (**3a**) was enhanced after hydrogenation with Wilkinson's catalyst.

Keywords: *polymer synthesis, molecular engineering, polynorbornene dicarboximide, ROMP, ruthenium alkylidene, hydrogenation*

1. Introduction

Ring-opening metathesis polymerization (ROMP) of norbornene dicarboximides with linear aliphatic and aromatic substituents has been described [1–6]. We recently proceeded with the synthesis of new polynorbornene dicarboximides by ROMP of *exo-N*-(1-adamantyl)-norbornene-5,6-dicarboximide and *exo-endo-N*-cyclohexyl-(cyclopentyl)-norbornene-5,6-dicarboximides using well-defined ruthenium alkylidene (vinylidene) catalysts [7–9]. The carboximide functionalized polynorbornenes showed high T_g's, good mechanical properties and high thermal resistance [4, 7, 8]. The membranes prepared from these polymers exhibit rather high permselectivity for the separation of hydrogen from nitrogen, carbon monoxide, methane and ethylene [10, 11].

Introduction of fluorine atoms into polymer structure can cause significant change in physical and chemical properties of polymers. It is well known that fluorinated polymers are important specialty materials in many applications [12]. Thus, compared to polynorbornene, partially fluorinated polynorbornene membranes exhibit higher gas permeability and selectivity [13, 14]. The ROMP of norbornene derivatives with various fluorine-containing units is well established [15]. For example, a wide range of thermally stable and solvent resistant fluorinated polynorbornenes using the ROMP classical catalysts have been synthesized by Feast *et al*. [16–18].

The development of highly active metal-alkylidene catalysts opens vast opportunities in olefin metathesis and their application to the synthesis of

---

*Corresponding author, e-mail: tma@servidor.unam.mx well-defined products [19, 20]. The resent generation of ruthenium alkylidene catalysts coordinated with N-heterocyclic carbene ligands makes possible to metathesize challenging cyclic and linear olefins with sterically hindered or electronically deactivating groups [21]. *Endo*-isomers of norbornene derivatives are challenging and few examples of their metathesis exist [22–24].

The goal of this study is the synthesis and ROMP of new *N*-3,5-bis(trifluoromethyl)phenyl-*endo*-norbornene-5,6-dicarboximide (TFMPhNDI) (**2a**), *N*-4-fluorophenyl-*endo*-norbornene-5,6-dicarboximide (FPhNDI) (**2b**) and *N*-2,2,6,6-tetramethylpiperidyl-*endo*-norbornene-5,6-dicarboximide (TMPNDI) (**2c**) using a second generation ruthenium alkylidene catalyst (1,3-dimesityl-4,5-dihydroimidazol-2-ylidene) ($PCy_3Cl_2Ru = CHPh$) (**I**). One of the objectives of this work also is the hydrogenation of Poly-TFMPhNDI (**3a**). The transformation of the rigid double bonds into single bonds would increase the conformational mobility of polymer chains and thermo- and photo-oxidative stability of polynorbornenes.

2. Experimental

2.1. Techniques

^{1}H NMR, ^{13}C NMR and ^{19}F NMR spectra were recorded on a Varian spectrometer at 300, 75 and 300 MHz, respectively, in $CDCl_3$ or DMSO. Tetramethylsilane (TMS) and trifluoracetic acid (TFA) were used as internal standards, respectively. Glass transition temperatures, T_g, were determined in a DSC-7 Perkin Elmer Inc., at scanning rate of 10°C/min under nitrogen atmosphere. The samples were encapsulated in standard aluminum DSC pans. Each sample was run twice on the temperature range between 30 and 300°C under nitrogen atmosphere. Onset of decomposition temperature, T_d, was determined using thermogravimetric analysis, TGA, which was performed at a heating rate of 10°C/min under nitrogen atmosphere with a DuPont 2100 instrument. FTIR spectra were obtained on a Nicolet 510 p spectrometer. Molecular weights and molecular weight distributions were determined with reference to polystyrene standards on a Varian 9012 GPC at 30°C, in chloroform for polymers **3a** and **3c** and in dimethylformamide for polymer **3b**, using a universal column and a flow rate of 1 ml/min. Mechanical properties under tension were measured in a Universal Mechanical Testing Machine Instron 1125-5500R using a 50 kg cell at a crosshead speed of 1 mm/min according to the method ASTM D1708 in film samples of 0.5 mm of thickness at room temperature.

2.2. Reagents

3,5-Bis(trifluoromethyl)aniline, 4-fluoroaniline, 2,2,6,6-tetramethylpiperidylamine, *cis*-5-norbornene-*endo*-2,3-dicarboxylic anhydride (***endo*-NDA**) and other chemicals were purchased from Aldrich Chemical Co. and used without further purification. 1,2-dichloroethane and toluene were dried over anhydrous calcium chloride and distilled under nitrogen over CaH_2. Catalyst 1,3-bis(2,4,6-trimethylphenyl)-4,5-dihydroimidazol-2-ylidene ($(PCy_3)Cl_2Ru = CHPh$) (**I**) was purchased from Aldrich Chemical Co. and used as received.

2.3. Synthesis and characterization of monomers

2.3.1. Synthesis of *N*-3,5-bis(trifluoromethyl)phenyl-*endo*-norbornene-5,6-dicarboximide (TFMPhNDI) (2a)

***endo*-NDA** (5 g, 30.5 mmol) was dissolved in 50 ml of toluene. An amount of 7.0 g (30.6 mmol) of 3,5-bis(trifluoromethyl)aniline in 5 ml of toluene is added dropwise to the stirred solution of endo-NDA. The reaction was maintained at 60°C for 2 h and then cooled to room temperature. A precipitate was filtered and dried to give 11.5 g of amic acid **1a**. The obtained amic acid **1a** (11.5 g, 29.2 mmol), anhydrous sodium acetate (2.2 g, 26.8 mmol) and acetic anhydride (34.0 g, 333 mmol) were heated at 90°C for 4 h and then cooled. The solid which crystallized out on cooling was filtered, washed several times with cold water and dried in a vacuum oven at 50°C overnight. Pure monomer **2a** (Figure 1) was obtained after two recrystallizations from hexane (87% yield).

mp 105–108°C.

FT-IR (KBr): 3073 (C=C–H str), 3013, 2977 (C–H asym. str.), 2877 (C–H sym. str.), 1781 (C=O), 1712 (C=O), 1627 (C=C str), 1470 (C–H def), 1405 (C–N), 1337 (C–H def), 1286 (C–H def), 1181,

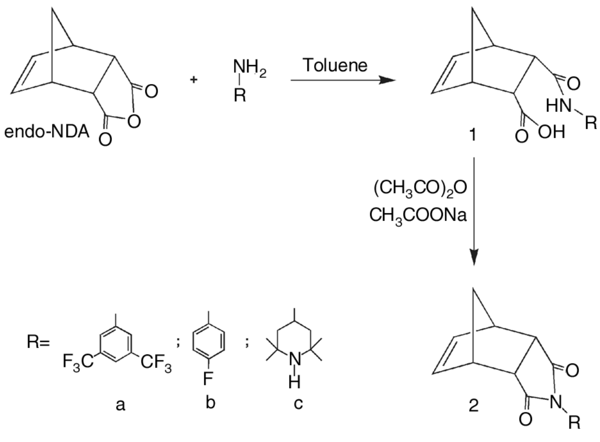

Figure 1. Synthesis route of monomers **2a**, **2b** and **2c**

1129, 922 (C–C), 872, 844, 751 (C=C–H def), 680, 626 cm^{-1}.

^{1}H NMR (300 MHz, CDCl$_3$) (Figure 4) δ (ppm): 7.87 (1H, s), 7.69 (2H, s), 6.29 (2H, s), 3.55–3.48 (4H, m), 1.85–1.63 (2H, m).

^{13}C NMR (75 MHz, CDCl$_3$) δ (ppm): 175.8, 134.7, 132.6, 132.1, 126.7, 124.5, 122.1, 120.9, 52.4, 45.6, 37.6.

^{19}F NMR (300 MHz, CDCl$_3$, ref. TFA [–77 ppm]) δ (ppm): –62.2.

Anal. Calcd. (%) for C$_{17}$H$_{11}$O$_2$F$_6$N: C, 54.40; H, 2.93; O, 8.53; F, 30.40; N, 3.73. Found: C, 54.80; H, 2.70; N, 4.06.

2.3.2. Synthesis of *N*-4-fluorophenyl-*endo*-norbornene-5,6-dicarboximide (FPhNDI) (2b)

***endo*-NDA** (5 g, 30.5 mmol) was dissolved in 50 ml of toluene. An amount of 3.4 g (30.6 mmol) of 4-fluoroaniline in 5 ml of toluene is added dropwise to the stirred solution of ***endo*-NDA**. The reaction was maintained at 90°C for 2 h and then cooled to room temperature. A precipitate was filtered and dried to give 8.1 g of amic acid **1b**. The obtained amic acid **1b** (8.1 g, 29.4 mmol), anhydrous sodium acetate (1.5 g, 18.29 mmol) and acetic anhydride (24 g, 235 mmol) were heated at 90°C for 4 h and then cooled. The solid which crystallized out on cooling was filtered, washed several times with cold water and dried in a vacuum oven at 50°C overnight. Pure monomer **2b** (Figure 1) was obtained after two recrystallizations from toluene (88% yield).

mp 170–173°C.

FT-IR (KBr): 3072.2 (C=C–H asym. str.), 3005 (C–H asym. str.), 2953.2 (C–H sym. str.), 1771.2 (C=O), 1705.8 (C=O), 1602.7 (C=C str), 1496 (C–H), 1387 (C–N), 1317 (C–F), 615 cm^{-1} (C–H).

^{1}H NMR (300 MHz, CDCl$_3$) δ (ppm): 7.12 (4H, m), 6.25 (2H, s), 3.50 (2H, s), 3.43 (2H, s), 1.80–1.6 (2H, m).

^{13}C NMR (75 MHz, CDCl$_3$) δ (ppm): 176.7, 163.7, 160.4, 134.5, 128.4, 127.7, 116.2, 52.2, 46.0, 45.5.

^{19}F NMR (300 MHz, CDCl$_3$, ref. TFA [–77 ppm]) δ (ppm): –113.09.

Anal. Calcd. (%) for C$_{15}$H$_{12}$O$_2$FN: C, 70.03; H, 4.66; O, 12.45; F, 7.39; N, 5.44. Found C, 70.53; H, 4.41; N, 5.81.

2.3.3. *N*-2,2,6,6-tetramethylpiperidyl-*endo*-norbornene-5,6-dicarboximide (TMPNDI) (2c)

***endo*-NDA** (5 g, 30.5 mmol) was dissolved in 50 ml of toluene. An amount of 4.75 g (30.4 mmol) of 2,2,6,6-tetramethylpiperidylamine in 5 ml of toluene was added dropwise to the stirred solution of ***endo*-NDA**. The reaction was maintained at 60°C for 3 h. A precipitate was filtered and dried to give 9.2 g of amic acid (**1c**). The amic acid obtained (9.2 g, 28.7 mmol), anhydrous sodium acetate (1.8 g, 22.0 mmol) and acetic anhydride (27.2 g, 266 mmol) were heated at reflux for 5 h and then cooled. The solid which crystallized out on cooling was filtered, washed several times with cold water and dried in a vacuum oven at 50°C overnight. Pure monomer **2c** (Figure 1) was obtained after two recrystallizations from hexane (84% yield).

mp 116–119°C.

FT-IR (KBr): 3242 (N–H str), 2968 (C=C–H asym str), 1765 (C=O), 1697 (C=O), 1631 (C=C str), 1474 (C–H), 1369 (C–N), 1319, 1292 (C=C–H), 1207, 1159, 1127, 1090, 1044, 979, 915, 846 (C–C str), 741, 683, 625 cm^{-1}.

^{1}H NMR (300 MHz, CDCl$_3$) (Figure 5) δ (ppm): 6.13 (2H, s), 4.39–4.28 (1H, m), 3.39 (2H, m), 3.22 (2H, m), 2.48 (2H, t), 2.26 (2H, s), 1.75–1.71 (1H, m), 1.58–1.46 (14H, m).

^{13}C NMR (75 MHz, CDCl$_3$) δ (ppm): 177.7, 174.2, 134.3, 57.9, 51.9, 45.5, 45.0, 43.8, 42.7, 33.1, 29.8, 27.8.

Anal. Calcd. (%) for $C_{18}H_{26}O_2N_2$: C, 71.52; H, 8.60; O, 10.59; N, 9.27. Found: C, 72.02; H, 8.35; N, 9.64.

2.4. Metathesis polymerization of monomers

Polymerizations were carried out in glass vials under dry nitrogen atmosphere at 45°C. Polymerizations were quenched by adding a small amount of ethyl vinyl ether and the solutions were poured into an excess of methanol. The polymers were purified by solubilization in chloroform containing a few drops of 1 N HCl and precipitation into either methanol or ethyl ether. The obtained polymers were dried in a vacuum oven at 40°C to constant weight.

2.4.1. Polymerization of 2a

1 g (2.66 mmol) of **2a** and 0.0023 g ($2.70\cdot10^{-3}$ mmol) of catalyst **I** were stirred in 2.7 ml of 1,2-dichloroethane at 45°C for 3 h (Figure 2). The obtained polymer **3a** was soluble in chloroform and dichloromethane.

T_g = 165°C, M_w/M_n = 1.6, M_n = 25,000.

FT-IR: 3036, 2941, 2880, 1778, 1733, 1598,1462, 1360, 1332, 1298, 1160, 983, 790 cm^{-1}.

^1H NMR (300 MHz, $CDCl_3$) (Figure 4) δ (ppm): 7.89–7.69 (3H, m), 5.85 (2H, m, trans), 5.67 (2H, m, cis), 3.46 (2H, m), 3.09 (2H, m), 2.02–1.52 (2H, m).

^{13}C NMR (75 MHz, $CDCl_3$) δ (ppm): 174.0, 133.2 (*cis*), 132.6 (*trans*), 129.2, 126.5, 124.5, 122.1, 120.9, 48.9, 45.3, 40.6, 37.5.

^{19}F NMR (300 MHz, $CDCl_3$, ref. TFA [–77 ppm]) δ (ppm): –62.0.

2.4.2. Polymerization of 2b

1 g (3.89 mmol) of **2b** and 0.0033 g ($3.89\cdot10^{-3}$ mmol) of catalyst **I** were stirred in 3.9 ml of 1,2-dichloroethane at 45°C for 3 h (Figure 2). The obtained polymer **3b** was soluble in 1,2-dichloroethane, DMF and DMSO.

T_g = 180°C, M_w/M_n = 1.8, M_n = 34,500.

FT-IR: 3075, 2998, 2947, 1768, 1700, 1597, 1492, 1390, 1320, 611 cm^{-1}.

^1H NMR (300 MHz, DMSO-d_6) δ (ppm): 7.32–7.13 (4H, m), 5.70 (2H, s, trans), 5.53 (2H, s, cis), 3.86 (2H, m), 3.48 (2H, m), 3.40 (2H, m), 1.76–1.37 (2H, m).

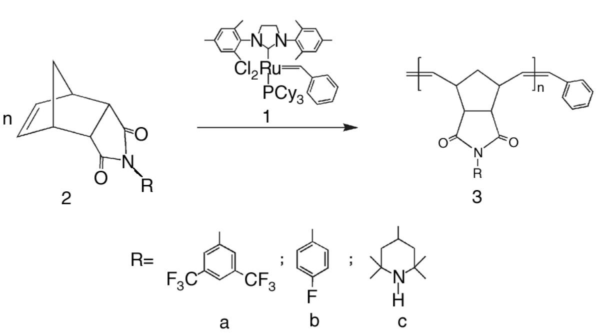

Figure 2. Ring opening metathesis polymerization of monomers **2a**, **2b** and **2c**

^{13}C NMR (75 MHz, DMSO-d_6) δ (ppm): 176.9, 175.9, 160.0, 134.6 (*cis*), 133.9 (*trans*), 129.4, 128.9, 116.0, 115.7, 51.9, 48.9, 48.6, 48.3, 48.0, 47.7, 47.5, 47.2, 46.9, 45.5, 44.9.

^{19}F NMR (300 MHz, DMSO-d_6, ref. TFA [–77 ppm]) δ (ppm): –112.40.

2.4.3. Polymerization of 2c

1 g (3.31 mmol) of **2c** and 0.0028 g ($3.29\cdot10^{-3}$ mmol) of catalyst **I** were stirred in 3.3 ml of 1,2-dichloroethane at 45°C for 3 h (Figure 2). The obtained polymer **3c** was soluble in chloroform and dichloromethane.

T_g = 189°C, M_w/M_n = 1.9, M_n = 39,300.

FT-IR: 3241, 2960, 1769, 1698, 1628, 1478, 1361, 1310, 1286, 1212, 1162, 1129, 1087, 1047, 976, 911, 849, 746, 680, 622 cm^{-1}.

^1H NMR (300 MHz, $CDCl_3$) (Figure 5) δ (ppm): 5.69 (2H, s, trans), 5.62 (2H, s, cis), 4.49 (1H, m), 3.19 (2H, s), 2.95 (2H, m), 2.60 (2H, s), 2.26 (2H, s), 1.90 (1H, s), 1.60–1.26 (14H, m).

^{13}C NMR (75 MHZ, $CDCl_3$) δ (ppm): 176.5, 175.8, 174.2, 169.6, 132.0 (*cis*), 129.3 (*trans*), 123.6, 58.0, 53.0, 48.3, 44.1, 43.2, 40.3, 33.3, 29.8, 27.6, 25.3, 24.3, 18.2.

2.5. Polymer hydrogenation

The hydrogenation of poly(*N*-bis(trifluoromethyl) phenyl-*endo*-norbornene-5,6-dicarboximide) (Figure 3) was made using several catalysts. The reaction was investigated at room temperature and pressures ranging from 1–115 bar. The catalysts employed in the reaction were: Pd/C, PtO_2, Al/Ni and Wilkinson catalyst $ClRh(PPh_3)_3$.

A Parr shaker hydrogenator was used. This apparatus provides compact and easily operated systems for the treatment of chemicals with hydrogen in the

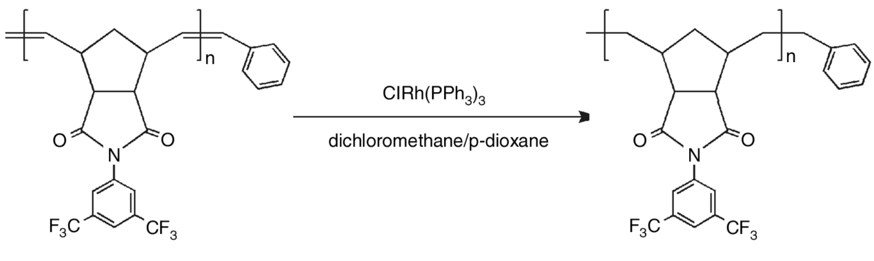

3a

4a

Figure 3. Hydrogenation of Poly-TFMPhNDI (**3a**) by Wilkinson's catalyst

presence of a catalyst at pressure up to 5 bar. The polymer to be treated in a Parr hydrogenator is sealed in a reaction bottle with the catalyst and connected to a hydrogen reservoir. Air is removed by evacuating the bottle. Pressure is then applied from the reservoir and the bottle is shaken vigorously to initiate the reaction. The progress of the reaction was followed by observing the pressure drop in the system and by ^{1}H NMR (Figure 4). The reaction at high pressure was carried out in a stainless steel 160 ml autoclave (Parr).

^{1}H NMR spectra were obtained on a Varian Gemini spectrometer at an observation frequency of 200 MHz with TMS as internal standard.

In a typical procedure, the polymer (0.5 g) was added to 60 ml of solvent in a Schlenk tube. The catalyst was previously introduced into the reactor. The solution was degassed and charged into the reactor under N_2. Hydrogen was added.

The optimum H_2 pressure is higher than 80 bar with $ClRh(PPh_3)_3$ as catalyst. Experiments were carried out using several solvents and the mixture dichloromethane-*p*-dioxane provided the best result. $T_g = 142°C$, $M_w/M_n = 1.9$, $M_n = 25{,}870$.

3. Results and discussion

Monomers **2a**, **2b** and **2c** were readily prepared with high yields (84–88%). 3,5-bis(trifluoromethyl)aniline, 4-fluoroaniline and 2,2,6,6-tetramethylpiperidylamine reacted with ***endo*-NDA** to the corresponding amic acids which were cyclized to *endo*-imides using acetic anhydride as dehydrating agent (Figure 1). ^{1}H, ^{13}C and ^{19}F NMR spectra and elemental analysis confirmed monomers structures and purity. The infrared spectra of monomers were very similar and showed characteristic peaks at 1760 and 1690 cm^{-1} (asymmetric and symmetric C=O stretching), 1400 cm^{-1} (C–N stretching). ROMP of monomers using ruthenium catalyst **I** were carried out in 1,2-dichloroethane at 45°C. The *endo* monomers reacted in 3 h giving polymer with high yields (93–97%). The results obtained by GPC analysis show that the number average molecular weights (M_n) were between 25,000 and 39,300. Polymer yields showed a slightly decrease with increasing the monomer to catalyst ratio. The polydispersity of the polymers is about $M_w/M_n = 1.6$–1.9 which is broader compared to polymers prepared by a living polymerization. This fact is due to slow initiation of this catalyst [25]. It has been also reported that the *endo* norbornene monomers give polymers with broader polydispersity compared to polymers from *exo* monomers [23].

Changing the pendant moiety did not affect neither the conversion of monomers nor the stereochemistry of the double bonds in the polymer. Catalyst **I** gives polymers with a mixture of *cis* and *trans* double bonds (42–49% of *cis* structure). ^{1}H NMR spectra were used to determine the *cis*/*trans* content in the polymer. Figure 4 shows the ^{1}H NMR spectra of (a) monomer **2a**, (b) polymer **3a** prepared by **I** and (c) its saturated analogous polymer **4a**. The monomer olefinic signals at $\delta = 6.29$ ppm are replaced by new signals at $\delta = 5.85$ and 5.67 ppm, which corresponds to the *trans* and *cis* double bonds of the polymer, respectively. After the hydrogenation step, the signals mentioned above become weak and new signals corresponding to the methylene protons arise in the region of $\delta = 1.0$–2.5 ppm. The hydrogenation level was determined by integrating the area, in the ^{1}H NMR spectrum, of the olefinic proton region ($\delta = 5.5$–6 ppm) relative to aromatic proton region ($\delta = 7$–8.5 ppm) (Figure 4). A 98% of hydrogenation for poly-TFMPhNDI (**3a**) was achieved by Wilkinson catalyst $ClRh(PPh_3)_3$ at room temperature.

T_g's for Poly-TFMPhNDI (**3a**), Poly-FPhNDI (**3b**) and Poly-TMPNDI (**3c**) were observed at 165, 180 and 189°C, respectively (Figure 6). Polymer **3c**

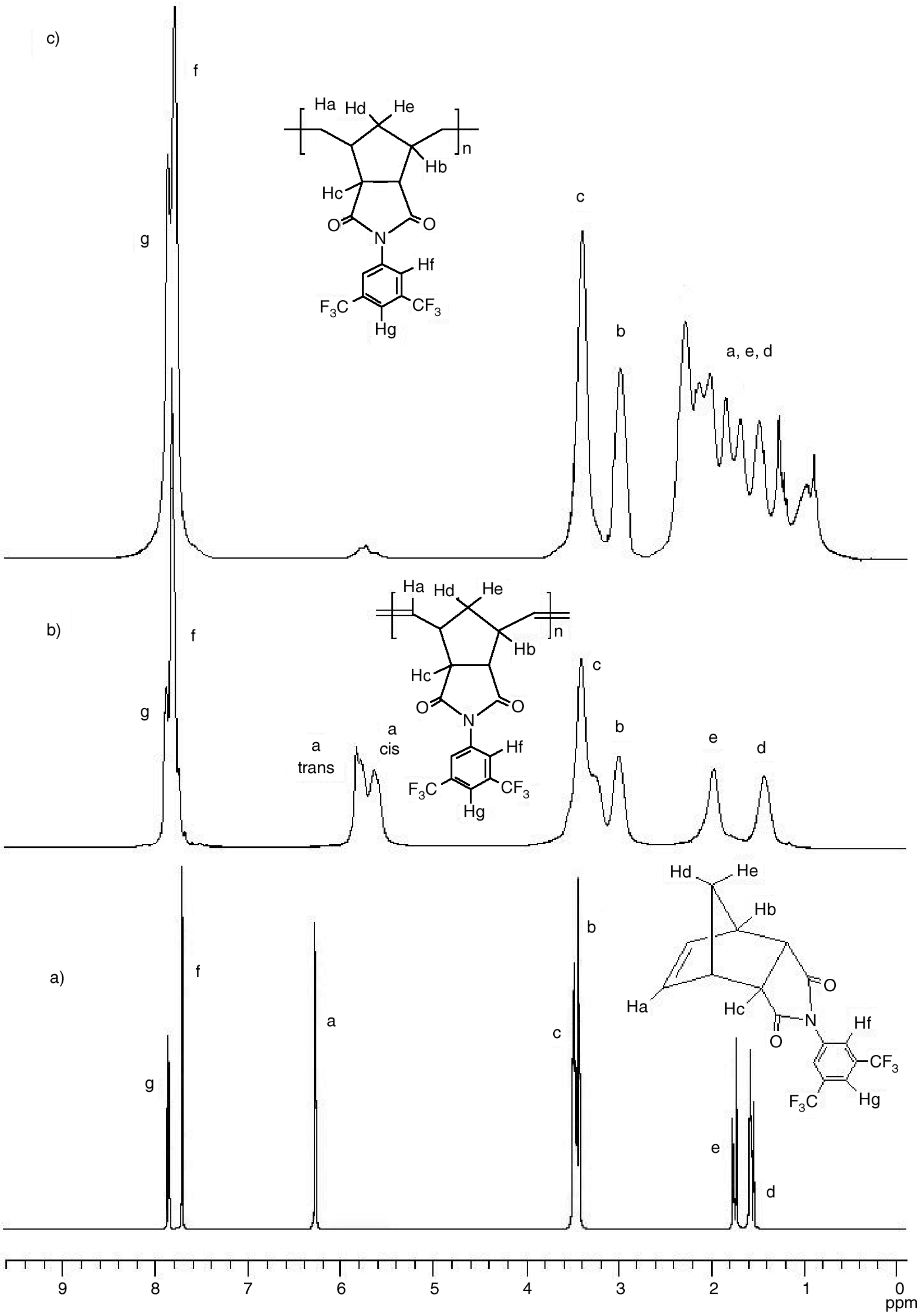

Figure 4. ^{1}H NMR spectra of a) monomer **2a**, b) polymer **3a** and c) its saturated analogous polymer **4a**

with larger substituents exhibits the higher glass transition temperature which indicates that the bulky tetramethyl groups should decrease the segmental motion of the polymer backbone. On the other hand, in spite of bearing the smaller substituent, polymer **3b** shows a T_g higher than polymer **3a**. The latter could be attributed to the ability of Poly-FPhNDI (**3b**) to chain packing which results in an increase in rigidity. The T_g of hydrogenated Poly-TFMPhNDI (**4a**) was lowered to 142°C on account of the highest conformational mobility of polymer chains in the saturated backbone which was also reflected in a lesser elastic modulus and stress in tension, 1567 and 28 MPa, respectively. The same effect of hydrogenation was

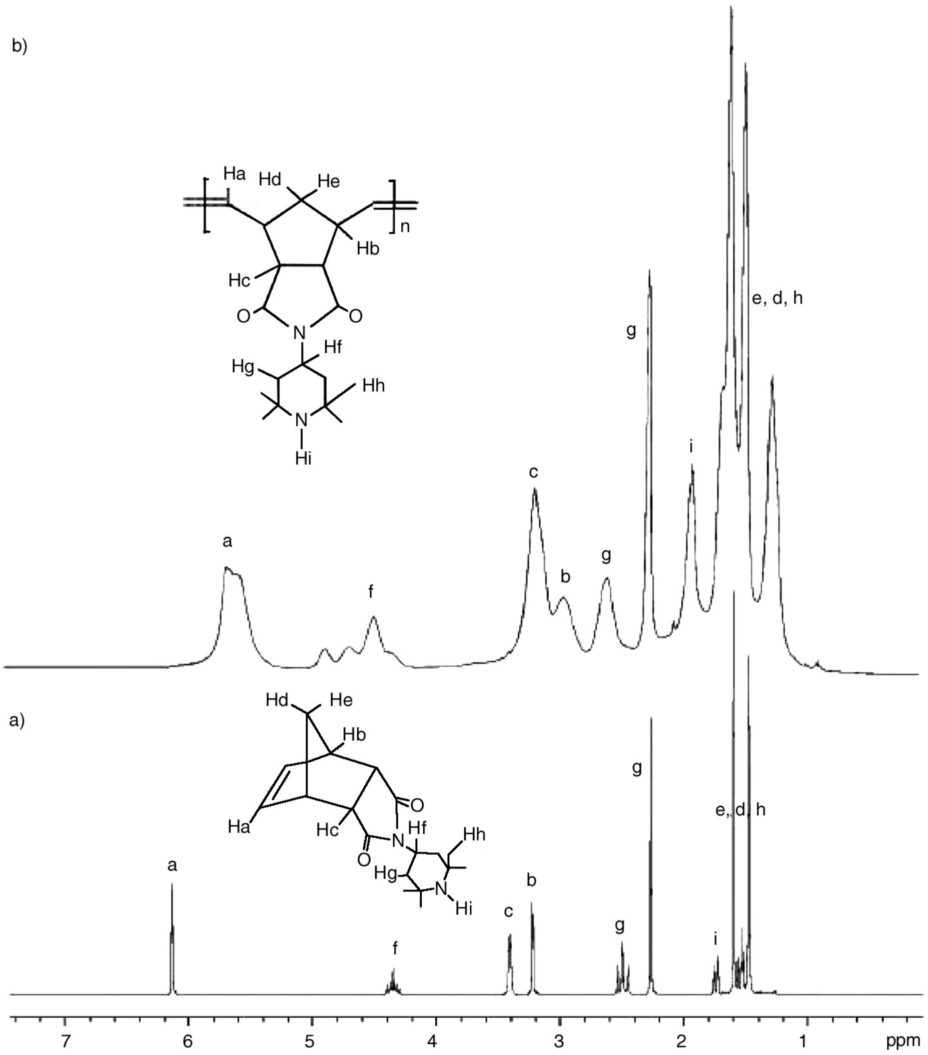

Figure 5. ^{1}H NMR spectra of a) monomer **2c** and b) polymer **3c**

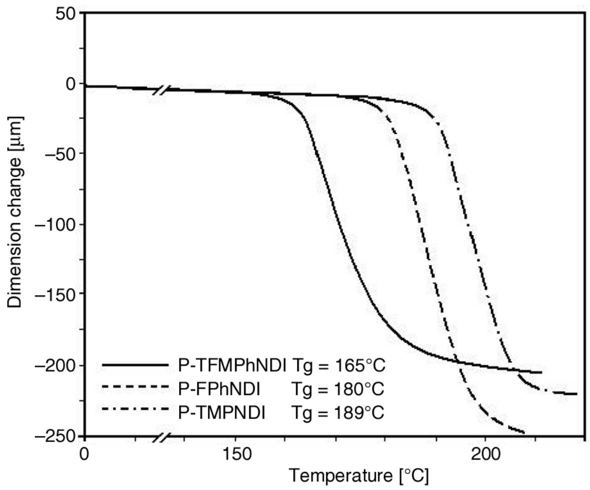

Figure 6. Thermomechanical curves of polymers **3a**, **3b** and **3c**, respectively

observed for other fluorine containing polynorbornenes [17].

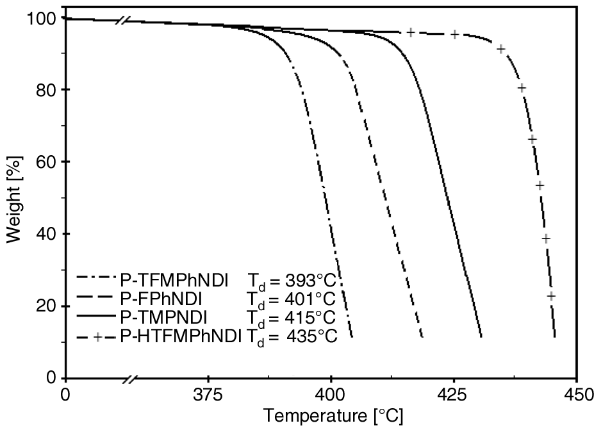

Figure 7. Thermogravimetric analysis of polymers **3a**, **3b**, **3c** and **4a** respectively

The thermal stability of the polymers was studied by TGA under N_2. As can be seen from Figure 7 onset temperature for decomposition of Poly-TFM-PhNDI is about 393°C which was considerably

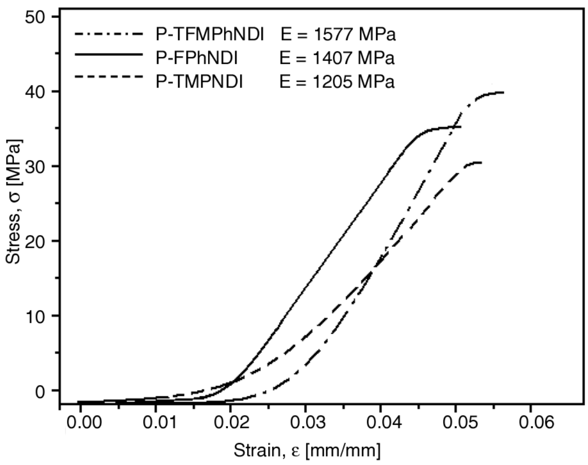

Figure 8. Stress versus strain plots of polymers **3a**, **3b** and **3c**, respectively

raised to 435°C (Poly-HTFMPhNDI, **4a**) after the hydrogenation step. Figure 8 represents, comparatively, the stress-strain curve in tension for the films of the synthesized polymers. The plots were cut at the maximum stress and show, for example, that not only the stress (39.1 MPa.) but also the elastic modulus (1577 MPa) are higher for the sample **3a**. In counterpart, the polymer **3c** has the lowest elastic modulus (1205 MPa) and stress in tension (30 MPa).

4. Conclusions

Endo isomers of TFMPhNDI (**2a**), FPhNDI (**2b**) and TMPNDI (**3c**) were synthesized and polymerized via ROMP using a second generation ruthenium alkylidene catalyst (1,3-dimesityl-4,5-dihydroimidazol-2-ylidene) ($PCy_3Cl_2Ru = CHPh$) (**I**). T_g's for Poly-TFMPhNDI, Poly-FPhNDI and Poly-TMPNDI were observed at 165, 180 and 189°C, respectively. Around 98% of hydrogenation for Poly-TFMPhNDI was achieved by $ClRh(PPh_3)_3$ catalyst. The onset of decomposition temperature, T_d, of the hydrogenated polymer was enhanced by almost 42°C nevertheless T_g was lowered to 142°C on account of the highest conformational mobility of polymer chains in the saturated backbone.

Acknowledgements

We thank DGAPA-UNAM PAPIIT for generous support to this research with contracts ES-104307 and IX227904. We are grateful to Alejandrina Acosta, Salvador López Morales and Miguel Ángel Canseco for their assistance in NMR, GPC and thermal properties, respectively.

References

[1] Bazan G. C., Schrock R. R., Cho H-N., Gibson V. C.: Polymerization of functionalized norbornenes employing Mo(CH-T-Bu)(NAr)(O-t-Bu)$_2$ as the initiator. Macromolecules, **24**, 4495–4502 (1991).

[2] Asrar J.: Metathesis polymerization of N-phenylnorbornenedicarboximide. Macromolecules, **25**, 5151–5156 (1992).

[3] Asrar J., Hurlbut J. B.: Synthesis, rheology, and physical properties of a metathesis polymer. Journal of Applied Polymer Science, **50**, 1727–1732 (1993).

[4] Asrar J.: High-temperature metathesis polymers: Structure-property relationships. Macromolecules, **27**, 4036–4042 (1994).

[5] Garbow R. J., Goetz J., Asrar J.: Polymers of methyl-substituted N-phenylnorbornene-5,6-dicarboximide: characterization of structure and dynamics. Macromolecules, **31**, 3925–3930 (1998).

[6] Weck M., Schwab P., Grubbs R. H.: Synthesis of ABA triblock copolymers of norbornenes and 7-oxanorbornenes via living ring-opening metathesis polymerization using well-defined, bimetallic ruthenium catalysts. Macromolecules, **29**, 1789–1793 (1996).

[7] Contreras A. P., Cerda A. M., Tlenkopatchev M. A.: Synthesis of high-T_g polymers by ring-opening metathesis polymerization of N-cycloalkylnorbornene dicarboximide. Macromolecular Chemistry and Physics, **203**, 1811–1818 (2002).

[8] Vargas J., Sánchez E., Tlenkopatchev M. A.: Ring-opening metathesis polymerization (ROMP) of N-cycloalkyl-7-oxanorbornene dicarboximides by well-defined ruthenium intiators. European Polymer Journal, **40**, 1325–1335 (2004).

[9] Díaz K., Vargas J., del Castillo L. F., Tlenkopatchev M. A., Aguilar-Vega M.: Polynorbornene dicarboximide with cyclic pendant groups: Synthesis and gas transport properties. Macromolecular Chemistry and Physics, **206**, 2316–2322 (2005).

[10] Tlenkopatchev M. A., Vargas J., López-González M. M., Riande E.: Gas transport in polymers prepared via metathesis copolymerization of exo-N-phenyl-7-oxanorbornene-5,6-dicarboximide and norbornene. Macromolecules, **36**, 8483–8488 (2003).

[11] Contreras A. P., Tlenkopatchev M. A., López-González M. M., Riande E.: Synthesis and gas transport properties of new high glass transition temperature ring-opened polynorbornenes. Macromolecules, **35**, 4677–4684 (2002).

[12] Sherratt S., Bringer R., Ferstandig L. L., Wolinski L. E., Barnhart W. S, Hall N. T.: The chemistry and technology of fluorine. Kirk-Othmer Encyclopedia of Chemical Technology. Wiley, New York (1966).

[13] Yampol'skii Y. P., Bespalova N. B., Finkel'shtein E. S., Bondar V. I., Popov A. V.: Synthesis, gas permeability, and gas sorption properties of fluorine-containing norbornene polymers. Macromolecules, **27**, 2872–2878 (1994).

[14] Tlenkopatchev M. A., Vargas J., Almaráz-Girón M. A., López-González M. M., Riande E.: Gas sorption in new fluorine containing polynorbornenes with imide side chain groups. Macromolecules, **38**, 2696–2703 (2005).

[15] Ivin K. J., Mol J. C.: Olefin metathesis and metathesis polymerization. Academic Press, San Diego (1997).

[16] Feast W. J., Blackmore P. M.: Stereoregular fluoropolymers: 6. The ring-opening polymerization of N-pentafluorophenylbicyclo[2.2.1]hept-5-ene-2,3-dicarb oximide. Journal of Fluorine Chemistry, **40**, 331–347 (1988).

[17] Feast W. J., Gimeno M., Khosravi E.: Approaches to highly polar polymers with low glass transition temperatures. 1. fluorinated polymers via a combination of ring-opening metathesis polymerization and hydrogenation. Polymer, **44**, 6111–6121 (2003).

[18] Feast W. J., Gimeno M., Khosravi E.: Approaches to highly polar polymers with low glass transition temperatures: 2. fluorinated polymers via ring-opening metathesis copolymerisation and hydrogenation. Journal of Molecular Catalysis A: Chemical, **213**, 9–14 (2004).

[19] Buchmeiser M. R.: Homogeneous metathesis polymerization by well-defined group vi and group viii transition-metal alkylidenes: fundamentals and applications in the preparation of advanced materials. Chemical Review, **100**, 1565–1604 (2000).

[20] Maughon B. R., Weck M., Mohr B., Grubbs R. H.: Influence of backbone rigidity on the thermotropic behavior of side-chain liquid crystalline polymers synthesized by ring-opening metathesis polymerization. Macromolecules, **30**, 257–265 (1997).

[21] Bielawski C. W., Grubbs R. H.: Highly efficient ring-opening metathesis polymerization (ROMP) using new ruthenium catalysts containing N-heterocyclic carbene ligands. Angewandte Chemie International Edition, **39**, 2903–2906 (2000).

[22] Khosravi E., Al-Hajaji A. A.: Ring opening metathesis polymerisation of N-alkyl norbornene dicarboxyimides using well-defined initiators. Polymer, **39**, 5619–5625 (1998).

[23] Khosravi E., Feast W. J., Al-Hajaji A. A., Leejarkpai T.: ROMP of N-alkyl norbornene dicarboxyimides: from classical to well-defined initiators, an overview. Journal of Molecular Catalysis A: Chemical, **160**, 1–11 (2000).

[24] Lapinte V., Brosse J-C., Fontaine L.: Synthesis and ring-opening metathesis polymerization (romp) reactivity of endo-and exo-norbornenylazlactone using ruthenium catalysts. Macromolecular Chemistry and Physics, **205**, 824–833 (2004).

[25] Grubbs R. H.: Olefin metathesis. Tetrahedron, **60**, 7117–7140 (2004).

eXPRESS Polymer Letters Vol.1, No.5 (2007) 283–291
Available online at www.expresspolymlett.com
DOI: 10.3144/expresspolymlett.2007.41

Effects of dynamical cure and compatibilization on the morphology and properties of the PP/epoxy blends

X. L. Jiang[*1], *K. Sun*[1], *Y. X. Zhang*[2]

[1]State Key Laboratory of Metal Matrix Composites,Shanghai Jiao Tong University, Shanghai, 200030, China
[2]Research Institute of Polymer Materials, Shanghai Jiao Tong University, Shanghai 200030, China

Received 28 February 2007; accepted in revised form 9 April 2007

Abstract. In this paper, effects of dynamical cure and compatibilization on the morphology and properties of the PP/epoxy blends were studied. The addition of maleic anhydride-grafted polypropylene (MAH-g-PP) and dynamical cure of epoxy by dicyanamide give rise to decrease the average diameter of epoxy particles in the PP/epoxy blends. The epoxy particles in the PP/epoxy blends act as effective nucleating agents, accelerating the crystallization of PP component. The dynamical cure and compatibilization increase the kinetic constant $K(T)$ of PP crystallization in the PP/epoxy blends. Dynamical cure of the epoxy resin leads to an improvement in the modulus and strength of the PP/epoxy blends, and the addition of MAH-g-PP results in an increase in the impact strength. Dynamic mechanical thermal analysis (DMTA) results indicate that the addition of MAH-g-PP improves the compatibility between PP and epoxy resin, and the storage modulus of the PP/epoxy blends increase by dynamical cure. Thermogravimetric analysis (TGA) results show dynamical cure of epoxy and addition of MAH-g-PP improved the thermal stability of the PP/epoxy blends. Wide-angle X-ray diffraction (WAXD) analysis shows that the PP/epoxy blends have the same crystalline structure as pure PP, indicating dynamical cure and compatibilization do not disturb the crystalline structure of the PP/epoxy blends.

Key words: *polymer blends and alloys, polypropylene (PP), epoxy resin, dynamical cure, compatibilization*

1. Introduction

Dynamical vulcanization is an effective way to prepare thermoplastic vulcanizates [1–3]. It is the process of vulcanizing an elastomer during melt-mixing with a molten plastic. This technology has led to a significant number of new thermoplastic elastomer products commercialized during the mid- to late-1980s [4–7]. Many thermoplastic vulcanizates are attributed to dynamic vulcanization of elastomers [8, 9]. However, as far as we know, there are few papers concerning dynamical vulcanization that is applied to thermoplastic resin/thermosetting resin blends [10].

The properties of polymeric materials strongly depend on their microstructure and crystal structure [11, 12]. PP has an important place among the synthetic polymers because of its growing commercial applications. However, it exhibits relatively lower modulus and stiffness compared to common engineering plastics. Glass fiber and inorganic fillers are often used to enhance the modulus and stiffness of PP [13, 14].

Our laboratory has applied dynamical vulcanization to prepare a new type of PP/epoxy blends with the structure of crosslinked epoxy resin particles dispersed in the PP matrix [15–17]. The blends were prepared in the mixing chamber of a Haake rheometer RC90 through dynamical curing an epoxy resin by 2-ethylene-4-methane-imidazole (EMI-2,4) in the molten PP.

In this paper, the PP/epoxy blends were prepared by extrusion method, and dicyanamide was used as

---

[*] Corresponding author, e-mail: jx1110@sjtu.edu.cn

a curing agent. As the epoxy resin and PP were immiscible, maleic anhydride-grafted polypropylene (MAH-g-PP) was acted as a compatibilizer, the effects of dynamical cure and compatibilization on morphology and properties of PP/epoxy blends were studied.

2. Experimental

2.1. Materials

PP, F401 was produced by Yangzi Petrochemical Co., Ltd. (China), with a melt flow index (MFI) of 1.9 dg/min (230°C, 2.16 kg). Diglycidyl ether of bisphenol-A resin with epoxy equivalent weight (EEW) of 2000 g/mol, was supplied by Shanghai Resin Co., Ltd. (China). The curing agent, dicyanamide, was supplied by Shanghai Chemical Agent Company (China). Maleic anhydride-grafted polypropylene (MAH-g-PP) with a MAH content of 1% was prepared by Shanghai Sunny New Technology Development Co., Ltd. (China), and its MFI is 6.8 dg/min (230°C, 2.16 kg).

2.2. Sample preparation

The PP/epoxy blends were prepared by twin-screw extruder. Before extruding, MAH-g-PP and the epoxy resin were dried at 80°C under vacuum for about 8 h. The content of dicyanamide is 2 parts per 100 parts by the weight of epoxy resin. The temperature profile of the extruder was 140°C, 160°C, 180°C and 200°C, and the rotation speed of the screws was 60 rpm. The strips from the extruder were cut into granules about 4 mm long after cooling in a water bath. The composition was moved out and compression-moulded in a press at 195°C for 10 min, then cold pressed to give samples for testing.

2.3. Scanning electron microscope (SEM) analysis

A scanning electron microscope (SEM, HITACHI-S-2150, Japan) was used to examine the morphology of the blends. Samples were fractured in liquid nitrogen and covered with a thin gold layer for further observation. The number-average particle diameter (d_n) was calculated from a minimum of 100 particles as $d_n = \Sigma n_i d_i / \Sigma n_i$ where n_i is the number of particles with a diameter d_i.

2.4. DSC analysis

Crystallization behavior was analyzed using a Perkin-Elmer DSC (Paris 1, USA) in a nitrogen atmosphere. Samples of about 4 mg were taken from the moulded plaques. Isothermal crystallization kinetics was performed as follows: the samples were heated to 200°C at a heating rate of 10°C/min and maintained at this temperature for 5 min in order to eliminate any previous thermal history and then were cooled rapidly (100°C/min) to the crystallization temperature, and maintained at that temperature till the time necessary for the complete crystallization of the PP matrix.

2.5. Measurements of mechanical properties

The tensile properties were measured using an Instron 4465 (UK) tensile tester at a crosshead speed of 20 mm/min according to ASTM D638. Notched Izod impact strengths were determined using a Ray-Ran Universal Pendulum Impact Tester (UK) at an impacting pendulum speed of 3.5 m/s, according to ASTM D256. Flexural properties were measured using the Instron 4465 and a three-point-loading rig, and the central head was loaded on the specimen at a speed of 1.7 mm/min according to ASTM D790. In each of the tests, at least five samples were tested, and the average results were reported.

2.6. Dynamic mechanical thermal analysis (DMTA)

Dynamic mechanical thermal analysis (DMTA) was carried out in a Dynamic Mechanical Thermal Analyser (Rheometrics Scientific DMTA IV, USA). Measurements were performed in the tension modeat a frequency of 1 Hz over a temperature range of –40°C to 150°C, and at a heating rate of 3°C/min. The strain amplitude remained at 0.01%.

2.7. Thermogravimetric analysis (TGA)

The thermogravimetry was carried out in a Perkin–Elmer TGA7 (USA). The samples were scanned from 30°C to 800°C at a heating rate of 20°C/min in a nitrogen atmosphere.

2.8. Wide-angle X-ray diffraction (WAXD) analysis

The X-ray diffraction experiments were performed using a Rigaku Dmax-rC diffractometer (Japan) with Cu target and a rotating anode generator operated at 40 kV and 100 mA. The scanning rate was 2°/min from 5° to 35°. The sample for WAXD measurement was prepared by compression-moulded at 200°C and 5 MPa.

3. Results and discussion

3.1. Morphology of the PP/epoxy blends

Figure 1 shows SEM micrographs of the fracture surfaces of the PP/epoxy (80/20), PP/MAH-g-PP/epoxy (75/5/20), dynamically cured PP/epoxy (80/20) and dynamically cured PP/MAH-g-PP/epoxy (75/5/20) blends. For the PP/epoxy (80/20) blend (Figure 1a), the epoxy resin is dispersed as spherical particles with a number-average diameter (d_n) of about 6 μm in the PP matrix, and the boundaries between the dispersed phase and the PP matrix are distinct. While for the PP/MAH-g-PP/epoxy (75/5/20) blend (Figure 1b), fine epoxy particles with d_n of about 1.0 μm are distributed in the PP matrix. The small particle size should be related to the presence of 5% MAH-g-PP. It can be concluded that MAH-g-PP improves the compatibility between PP and the epoxy resin. Figure 1c, d shows the fracture morphology of the dynamically cured PP/epoxy (80/20) and dynamically cured PP/MAH-g-PP/epoxy (75/5/20) blends. The d_n of epoxy particles in the dynamically cured PP/MAH-g-PP/epoxy (75/5/20) blend is much smaller than that of dynamically cured PP/epoxy (80/20) blend because of the compatibility of MAH-g-PP, and is about 0.5 μm which is also slightly smaller that of the PP/MAH-g-PP/epoxy (75/5/20) blend. The dynamically cured PP/epoxy (80/20) blend has the finer domains compared to the PP/epoxy (80/20) blend. The result shows that dynamical cure could further decrease an average diameter of epoxy particles in the PP/epoxy blends, which is attributed to the aggregation of the uncured epoxy particles in the blends and results in an increase in an average diameter of the epoxy particles.

The FTIR spectra of the MAH-g-PP, epoxy resin and PP/MAH-g-PP/epoxy (75/5/20) blend are shown in Figure 2, the characteristic band of the epoxy ring of the epoxy resin (Figure 2a) was observed at 921 cm^{-1}, and the absorption peak of the C–O–C appeared at 1259 cm^{-1}. Furthermore the characteristic band assigned to the $–CH_2–$ stretching of the epoxide ring was observed at

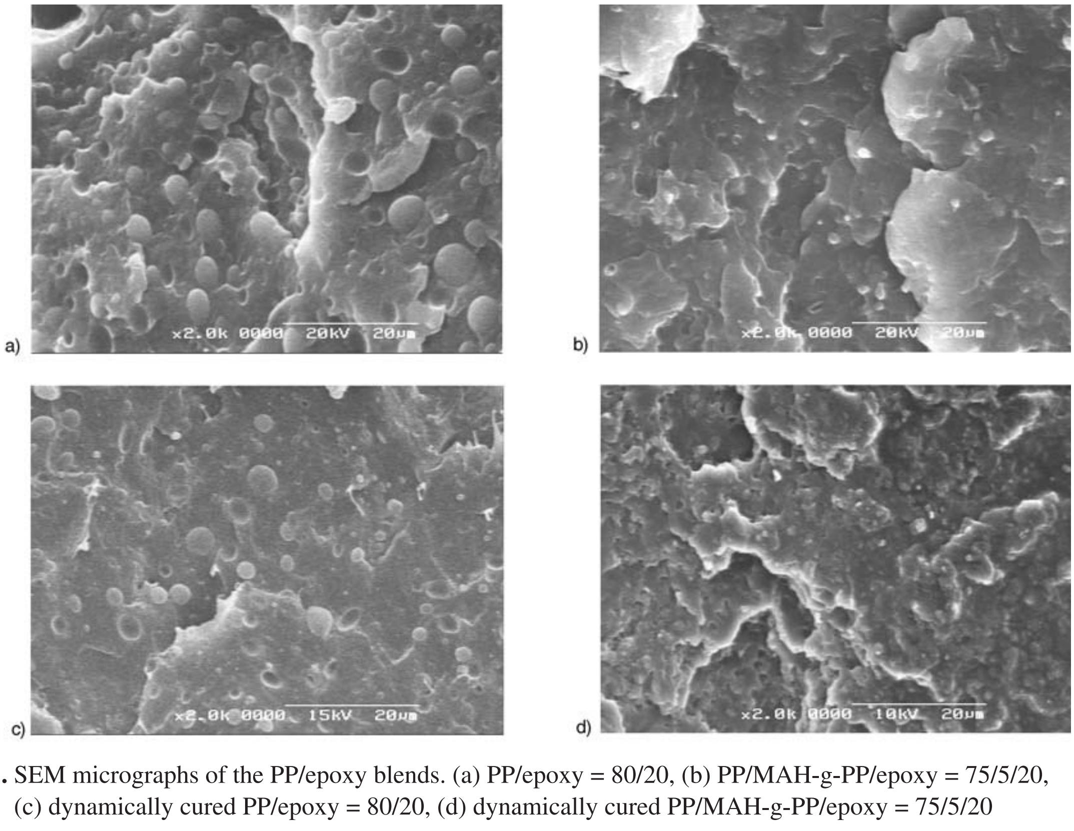

Figure 1. SEM micrographs of the PP/epoxy blends. (a) PP/epoxy = 80/20, (b) PP/MAH-g-PP/epoxy = 75/5/20, (c) dynamically cured PP/epoxy = 80/20, (d) dynamically cured PP/MAH-g-PP/epoxy = 75/5/20

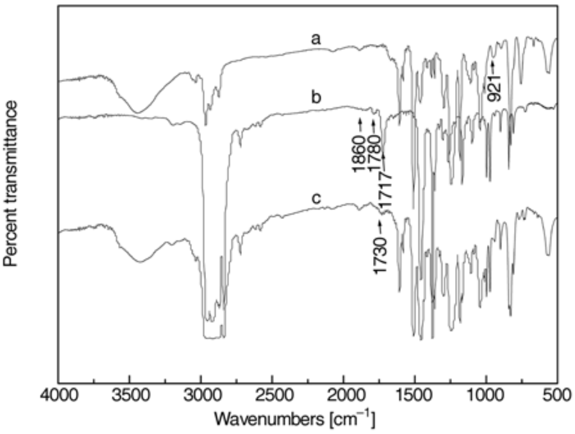

Figure 2. FTIR spectra of (a) epoxy resin (b) MAH-g-PP (c) PP/MAH-g-PP/epoxy = 75/5/20

2852–3057 cm^{-1}. The spectrum of MAH-g-PP (Figure 2b) shows the characteristics of a saturated ring anhydride. The bands at 1860 cm^{-1} and 1780 cm^{-1} are attributed to the symmetrical and asymmetrical stretching modes of C=O in the maleic anhydride and the bands at 1717 cm^{-1} are attributed to the C=O bond of maleic acid which is come from the hydrolyzate of MAH. In the case of the PP/MAH-g-PP/epoxy (75/5/20) blend (Figure 2c), a little higher absorption peak (1731 cm^{-1}) was seen compared with the absorption peak of the C=O of maleic acid at 1717 cm^{-1} in the spectrum of MAH-g-PP, which is come from the C=O of the ester group, the intensity of the peak attributed to the epoxide ring at 921 cm^{-1} also decreased. As MAH-g-PP has active maleic anhydride groups, the functional groups of MAH-g-PP react with the hydroxyl or epoxy groups of epoxy resin. A simple scheme of reaction between MAH-grafted PP and the epoxy resin was shown in Figure 3. We thought that the reactions between the groups take place in the PP/MAH-g-PP/epoxy blends and lead to an improved compatibility between PP and epoxy resin.

3.2. Isothermal crystallization kinetics of the PP/epoxy blends

The crystallization kinetics of polymers under isothermal conditions for various modes of nucleation and growth can be well approximated by the known Avrami equation [18, 19]. The general form of the Equation (1) is:

$$X(t) = 1 - \exp(-K(T)t^n) \tag{1}$$

where $X(t)$ is the relative crystallinity at different crystallization time, the Avrami exponent n is a constant depending on the mechanism of nucleation and the form of crystal growth, $K(T)$ is a constant related to nucleation and growth parameters. $X(t)$ can be calculated according to the Equation (2).

$$X(t) = \frac{Q_t}{Q_\infty} = \frac{\int_0^t \frac{\mathrm{d}H}{\mathrm{d}t}\mathrm{d}t}{\int_0^\infty \frac{\mathrm{d}H}{\mathrm{d}t}\mathrm{d}t} \tag{2}$$

where Q_t and Q_∞ are the heat generated at time t and infinite time t_∞, respectively, and dH/dt is heat evolution rate.

The Avrami equation can be written as (3):

$$\log[-\ln(1 - X(t))] = n\cdot\log t + \log K(T) \tag{3}$$

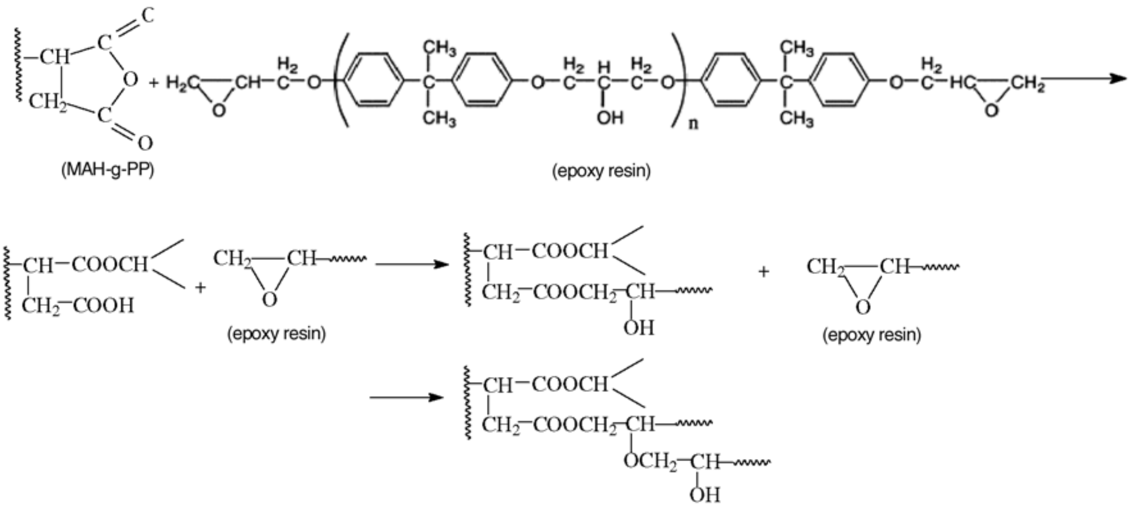

Figure 3. A simple scheme of reaction between MAH-g-PP and the epoxy resin

From a graphic representation of log[–ln(1 – $X(t)$)] versus log$t$, the Avrami exponent n (slope of the straight line) and the crystallization kinetic constant $K(T)$ (intersection with the y-axis) can be obtained. The half time of PP crystallization, $t_{1/2}$, is defined as the time at which the relative crystallinity is 50%. Figure 4 shows that the relative crystallinity $X(t)$ changes with increasing T_c. Usually, $t_{1/2}$ is employed to characterize the rate of crystallization directly. The greater the value of $t_{1/2}$ is, the smaller the rate of the crystallization. Plots of log[–ln(1–$X(t)$)] versus log$t$ are shown in Figure 5. The results from Figure 5 are listed in Table 1.

The kinetic constant $K(T)$ of PP crystallization in the PP/epoxy blends is higher than that of PP, which suggests that the epoxy particles act as effec-

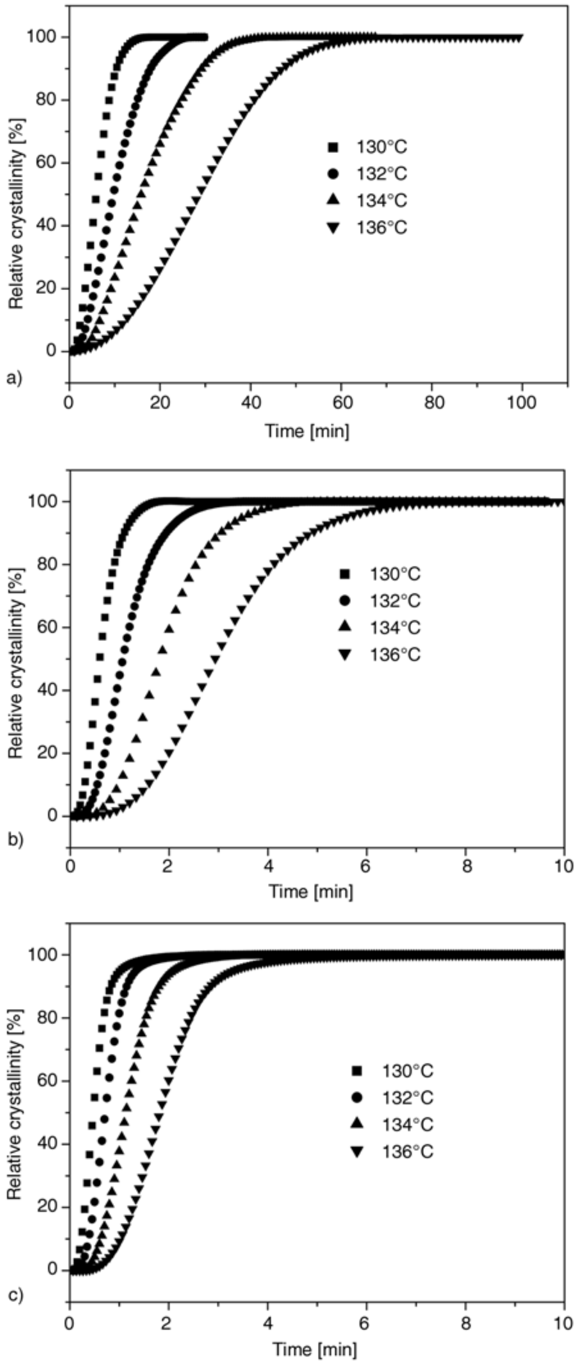

Figure 4. Development of relative crystallinity with time for isothermal crystallization. (a) PP; (b) PP/MAH-g-PP/epoxy = 75/5/20; (c) dynamically cured PP/MAH-g-PP/epoxy = 75/5/20

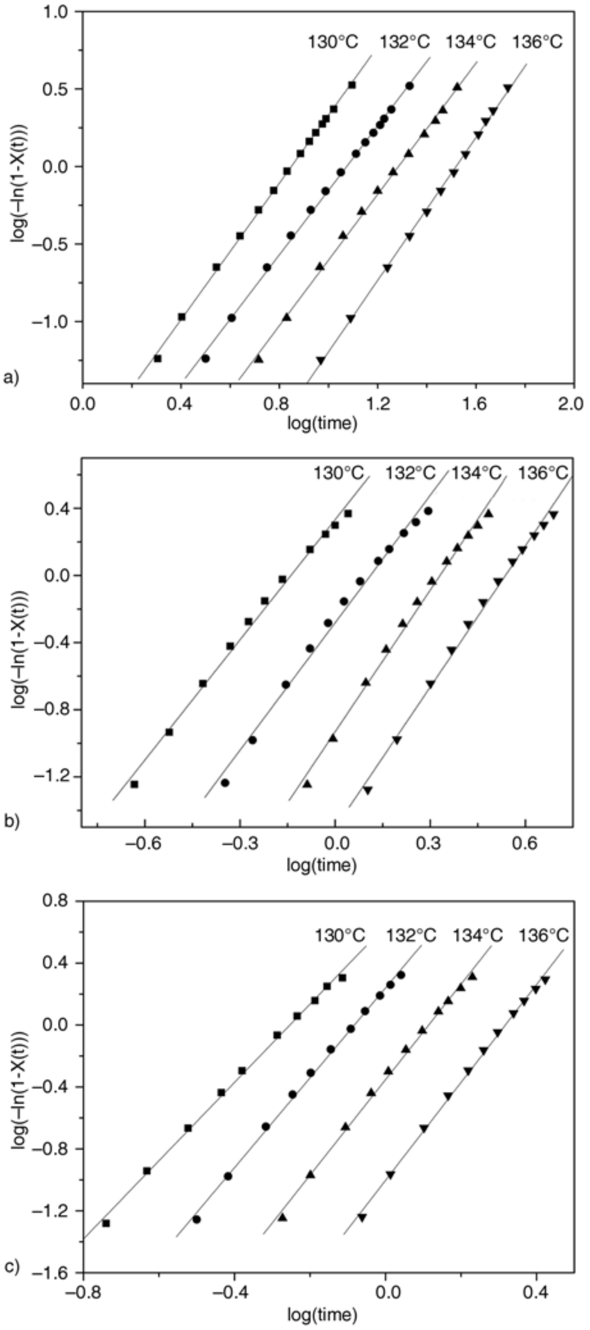

Figure 5. Avrami plots of PP and dynamically cured PP/epoxy blends at different crystallization temperature. (a) PP; (b) PP/MAH-g-PP/epoxy = 75/5/20; (c) dynamically cured PP/MAH-g-PP/epoxy = 75/5/20

Table 1. Kinetic parameters of the PP and the PP/epoxy blends

Compositions	T_c [°C]	K(*T*)	n	$t_{1/2}$ [min]
PP	130	0.065	2.09	5.34
	132	0.006	2.14	7.86
	134	0.002	2.20	13.80
	136	0.0003	2.30	30.97
PP/epoxy = 80/20	130	0.342	3.00	1.24
	132	0.085	3.08	1.92
	134	0.011	3.16	3.44
	136	0.004	3.29	5.42
PP/MAH-g-PP/epoxy = 75/5/20	130	2.152	2.78	0.61
	132	0.523	2.83	1.07
	134	0.117	2.91	1.81
	136	0.032	3.05	2.93
dynamically cured PP/epoxy=80/20	130	1.444	2.76	0.78
	132	0.185	2.98	1.51
	134	0.086	3.15	2.01
	136	0.017	3.29	3.05
dynamically cured PP/MAH-g-PP/epoxy = 75/5/20	130	4.37	2.87	0.46
	132	1.75	2.94	0.77
	134	0.44	3.10	1.27
	136	0.10	3.20	1.94

tive nucleating agents, accelerating the crystallization of PP component in the blends. *K*(*T*) of PP crystallization in the PP/MAH-g-PP/epoxy (75/5/20) and dynamically cured PP/MAH-g-PP/epoxy (75/5/20) are higher than that in the PP/epoxy (80/20) and dynamically cured PP/epoxy (80/20), and the dynamically cured PP/MAH-g-PP/epoxy (75/5/20) has a minimum of *K*(*T*) in all the PP/epoxy blends. The result shows that the dynamical cure and compatibilization further accelerated the crystallization of PP component in the PP/epoxy blends because the smaller size of epoxy particles act as the more effective the nucleating agents for PP crystallization. Nano-fillers often act as more effective nucleating agents for PP crystallization compared with other components [13, 20].

It is well known that the Avrami exponent *n* depends on the nucleation process and the geometry of the growing crystals. As shown in Table 1, the *n* value is about 3 for the PP/epoxy blends, which suggests a three-dimensional heterogeneous crystal growth in a spherical form of PP. As shown in Table 1, the PP/epoxy blends show a noticeable decrease in the half time of PP crystallization ($t_{1/2}$) compared with the pure PP, which is attributed to a nucleating effect of the epoxy particles on the PP crystallization. $t_{1/2}$ increases with increasing crystallization temperature at a given blend composition.

3.3. Mechanical properties

Table 2 shows the effects of dynamical cure and compatibilization the mechanical properties of the PP/epoxy blends. The addition of 20 wt% epoxy resin to the PP matrix improves the flexural modulus but reduces the impact strength, tensile strength, and elongation at break because of the poor compatibility between PP and the epoxy resin. Through the addition of 5 wt% MAH-g-PP (used as a compatibilizer), the PP/MAH-g-PP/epoxy (75/5/20) has a higher modulus and tensile strength than the PP/epoxy (80/20). The dynamically cured PP/epoxy (80/20) has the higher flexural modulus (1960 MPa) and tensile strength (38.8 MPa), which increase by 14% and 50%, respectively, in comparison with those of PP/epoxy (80/20), but the impact strength of the blend is lower than that of the PP/MAH-g-PP/epoxy (75/5/20). The dynamically cured PP/MAH-g-PP/epoxy (75/5/20) has best mechanical properties in all the PP/epoxy blends. The result shows that dynamical cure of the epoxy resin led to an improvement in the modulus and strength of the PP/epoxy blends, and the addition of MAH-g-PP results in the increases in the impact strength.

3.4. DMTA analysis

DMTA was used to determine the miscibility of the blends by investigating the glass transition temperatures (T_g) of the blend components. The loss factor (tanδ) and the storage modulus (*E*') are shown as

Table 2. Mechanical properties of PP and the PP/epoxy blends

Compositions	Impact strength [J/m]	Tensile strength [MPa]	Elongation at break [%]	Tensile modulus [MPa]	Flexural modulus [MPa]
PP	30±2	30.8±1.5	300±35	1357±44	1250±36
PP/epoxy (80/20)	20±3	24.2±1.2	11±3	1724±51	1650±42
PP/MAH-g-PP/epoxy (75/5/20)	31±2	38.6±1.7	22±4	1872±32	1792±29
dynamically cured PP/epoxy (80/20)	22±2	38.8±1.3	11±3	2097±38	1960±47
dynamically cured PP/MAH-g-PP/epoxy (75/5/20)	33±2	42.3±1.6	15±4	2268±29	2140±34

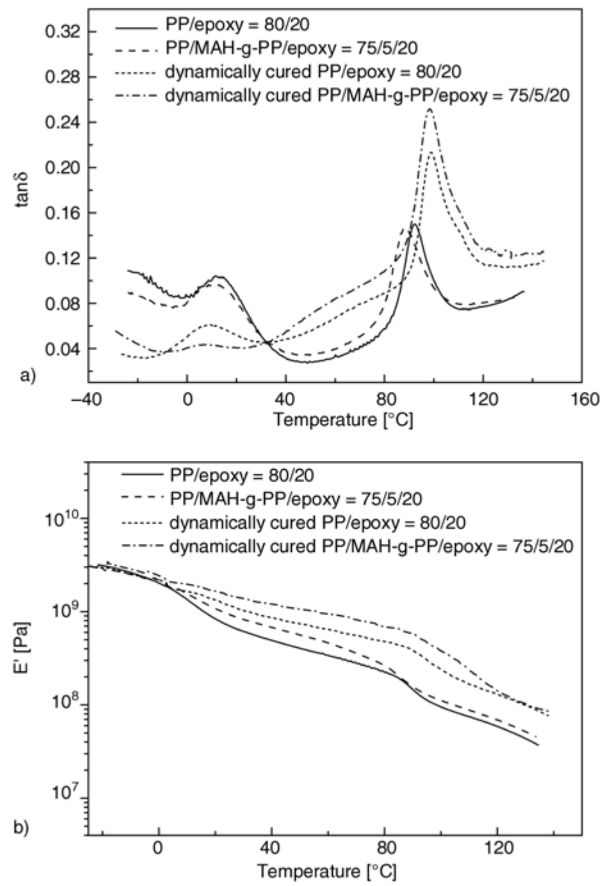

Figure 6. Curves of dynamical properties versus temperature for the PP/epoxy blends. (a) tanδ-temperature; (b) *E'* – temperature

functions of temperature for the PP/epoxy blends in Figure 6. Figure 6a shows the loss factor-temperature (tanδ–*T*)) curves for the blends. They indicate two obvious glass transition peaks, which confirm the presence of two phases. For the PP/epoxy (80/20) blend, the peak at about 12.5°C is the glass transition peak of PP, while the glass transition peak of the epoxy resin is at 90.4°C. The glass transition peak of the epoxy resin in the PP/MAH-g-PP/epoxy (75/5/20) blend moved to a lower temperature on the addition of 10 wt% MAH-g-PP, and this suggests that the compatibility between PP and epoxy resin was improved. The T_g values of the epoxy resin in the dynamically cured PP/epoxy (80/20) and dynamically cured PP/MAH-g-PP/epoxy (75/5/20) blends were higher than that of the epoxy resin in the PP/epoxy (80/20) and PP/MAH-g-PP/epoxy (75/5/20) blends, a shift in the T_g of the epoxy resin in the blends to a higher temperature suggests that dynamic cure results in a decrease in the molecular mobility of the epoxy resin.

Table 3. DMTA analysis results of the PP/epoxy blends

Compositions	T_g of PP [°C]	T_g of epoxy [°C]	E' at 25°C [Pa]
PP/epoxy = 80/20	12.5	90.4	$6.89\cdot10^{8}$
PP/MAH-g-PP/epoxy = 75/5/20	12.2	85.5	$8.09\cdot10^{8}$
dynamically cured PP/epoxy = 80/20	12.9	100.6	$9.24\cdot10^{8}$
dynamically cured PP/MAH-g-PP/epoxy = 75/5/20	12.2	99.7	$1.03\cdot10^{9}$

Figure 6b shows that the storage modulus (*E*') of the dynamically cured PP/MAH-g-PP/epoxy (75/5/20) and dynamically cured PP/epoxy (80/20) are obviously higher than that PP/epoxy (80/20) and PP/MAH-g-PP/epoxy (75/5/20), the dynamically cured PP/MAH-g-PP/epoxy (75/5/20) has highest *E*', but the PP/epoxy (80/20) blend has the lowest *E*'. The result shows that the interaction between PP and epoxy resin was strengthened by the addition of the MAH-g-PP, dynamical cure of epoxy resin increases the storage modulus (*E*') of the PP/epoxy blends (Table 3).

3.5. TGA analysis

One of the most widely accepted methods for studying the thermal properties of polymeric materials is thermogravimetry, which by means of integral and derivative thermogravimetric curves provide information about the nature and extent of degradation of polymeric materials [21]. Thermograms of the PP and PP/epoxy blends are shown in Figure 7. The degradation of PP started at 367°C and finished at 448°C. In the case of the PP/epoxy (80/20), the incorporation of 20 wt% epoxy resin increases the initial degradation temperature (T_0) from 367°C to 402°C. The T_0 of the PP/MAH-g-PP/epoxy (75/5/20) blend is higher than that of the PP/epoxy (80/20) blend, but lower than that of dynamically cured PP/epoxy (80/20) blend. The dynamically cured PP/MAH-g-PP/epoxy (75/5/20) blend has the highest initial degradation temperature (T_0) in the all PP/epoxy blends, the T_0 of the blend is about 429°C, and increases by 20°C compared with the PP/epoxy (80/20) blend (shown in Table 4). The temperature of maximum rates of mass losses (T_{max}) for PP and the PP/epoxy blends were obtained by derivative thermogravimetric (DTG) curves (shown in Figure 7b), and T_{max} has

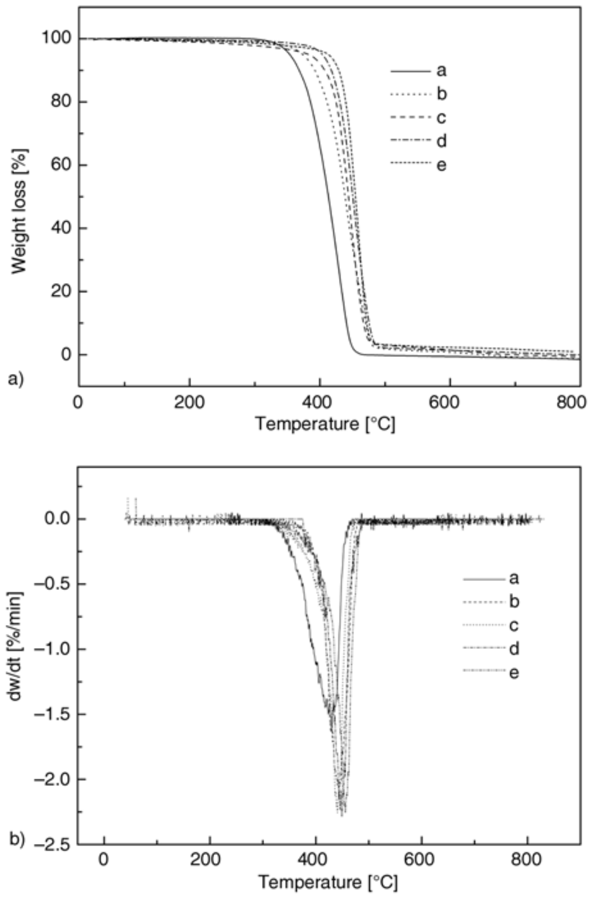

Figure 7. TG (a) and DTG (b) curves of the PP and the PP/epoxy blends. (a) PP; (b) PP/epoxy=80/20; (c) PP/MAH-g-PP/epoxy = 75/5/20; (d) dynamically cured PP/epoxy = 80/20; (e) dynamically cured PP/MAH-g-PP/epoxy = 75/5/20

Table 4. TG and DTG analysis results of PP and the PP/epoxy blends (T_0: initial degradation temperature; T_f: final degradation temperature; T_{max}: temperature of maximum rate of mass loss)

Compositions	T_0 [°C]	T_f [°C]	T_{max} [°C]
PP	367	448	424
PP/epoxy = 80/20	405	480	431
PP/MAH-g-PP/epoxy = 75/5/20	417	485	436
dynamically cured PP/epoxy = 80/20	425	492	441
dynamically cured PP/MAH-g-PP/epoxy = 75/5/20	430	498	448

the same tendency as T_0. All the degradation of PP/epoxy blends took place in one step, in the same way as for PP. The results show that the incorporation of the epoxy resin into the PP could improve the thermal stability of PP, and the dynamic cure of epoxy resin obviously could further improve the thermal stability. George [21] suggested that the thermal degradation of polymer blends depends not only on the thermal stability of the components but also on the morphology and the extent of interaction between the phases.

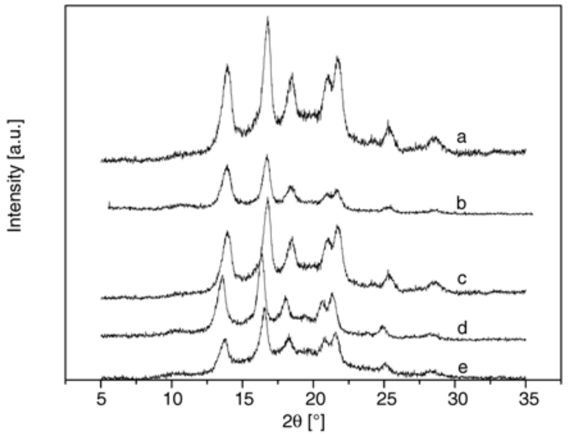

Figure 8. Crystal structure of PP and the PP/epoxy blends. (a) PP; (b) PP/epoxy = 80/20; (c) PP/MAH-g-PP/epoxy = 75/5/20; (d) dynamically cured PP/epoxy = 80/20; (e) dynamically cured PP/MAH-g-PP/epoxy = 75/5/20

3.6. Wide-angle X-ray diffraction (WAXD) analysis

In order to investigate whether the crystalline structure formed by one component of the blend can be affected by the other component or the compatibilizer. X-ray diffraction studies were made on the corresponding PP and the PP/epoxy blends. Figure 8 shows the WAXD patterns of PP, PP/epoxy (80/20), PP/MAH-g-PP/epoxy (75/5/20), dynamically cured PP/epoxy (80/20) and dynamically cured PP/MAH-g-PP/epoxy (75/5/20). Several reflections in both the PP/epoxy blends and PP are observed at 2θ = 13.9°, 16.7°, 18.3°, 20.9°, 21.8°, which belong to the identical monoclinic α form of the PP component. The result shows that the dynamical cure and compatibilization do not disturb the crystalline structure of PP in the PP/epoxy blends.

4. Conclusions

The PP/epoxy blends compatibilized with MAH-g-PP have finer domains compared with the PP/epoxy blends, and dynamical cure could further decrease an average diameter of epoxy particles in the PP/epoxy blends. Isothermal crystallization kinetics show that the dynamical cure and compatibilization give a rise to the number of smaller epoxy particles, further accelerating the crystallization of PP component in the PP/epoxy blends. Dynamical cure of the epoxy resin leads to an improvement in the tensile strength and flexural modulus of the PP/epoxy blends, and the addition of MAH-g-PP results in an increase in the impact strength. DMTA results indicate that the compatibility between PP and epoxy resin is improved by the addition of MAH-g-PP, and dynamical cure of epoxy resin obviously increase the storage modulus of the PP/epoxy blends. TGA results show the dynamical cure and compatibilization could improve the thermal stability of the PP/epoxy blends. The crystalline structure of PP in the PP/epoxy blends is the same as that of PP, and the dynamical cure and compatibilization do not disturb the crystalline structure of PP in the blends, a similar result was reported by Zhang [22].

References

[1] Geessler A. M.: Process for preparing a vulcanized blend of crystalline polypropylene and chlorinated butyl rubber. US Patent, 3037954, USA (1962).

[2] Fischer W. K.: Thermoplastic blend of partially cured monoolefin copolymer rubber. US Patent 3758643, USA (1971).

[3] Coran A. Y., Das B., Patel R. P.: Thermoplastic vulcanizates of olefin rubber and polyolefin resin, US Patent, 4130535, USA (1978).

[4] Coran A. Y., Patel R.: Rubber-thermoplastic compositions. Part I. EPDM-polypropylene thermoplastic vulcanizates. Rubber Chemistry and Technology, **53**, 141–150 (1980).

[5] Coran A. Y., Patel R.: Rubber-thermoplastic compositions. Part III. Predicting elastic moduli of melt mixed rubber-plastic blends. Rubber Chemistry and Technology, **54**, 91–100 (1981).

[6] Coran A. Y., Patel R. P.: Thermoplastic compositions of high unsaturation diene rubber and polyolefin resin. US Patent 4104210, USA (1975).

[7] Coran A. Y.: Thermoplastic elastomeric rubber-plastic blends. in 'Handbook of elastomers: new developments and technology' (eds.: Bhowmick A. K., Stephens H. L.) Marcel Dekker, New York, 249–260 (1988).

[8] Huang H., Yang J. L., Liu X., Zhang Y. X.: Dynamically vulcanized ethylene propylene diene terpolymer/nylon thermoplastic elastomers. European Polymer Journal, **38**, 857–861 (2002).

[9] Wang Z. J., Zhang X. F., Zhang Y., Zhang Y. X., Zhou W.: Effect of dynamic vulcanization on properties and morphology of nylon/SAN/NBR blends: A new compatibilization method of nylon/ABS blends. Journal of Applied Polymer Science, **87**, 2057–2062 (2003).

[10] Wan C., Patel S. H., Xanthos M.: Reactive melt modification of PP with a crosslinkable polyester. Polymer Engineering and Science, **43**, 1276–1288 (2003).

[11] Avalos F., López-Manchado M. A., Arroyo M.: Crystallization kinetics of polypropylene: 1. Effect of small additions of low-density polyethylene. Polymer, **37**, 5681–5688 (1996).

[12] Arroyo M., Zitzumbo R., Avalos F.: Composites based on PP/EPDM blends and short fibers I Morphology/behaviour relationship. Polymer, **41**, 6351–6359 (2000).

[13] Chan C-M., Wu J., Li J-X., Cheung Y-K.: Polypropylene/calcium carbonate nanocomposites. Polymer, **43**, 2981–2992 (2002).

[14] Lee N-J., Jang J.: The effect of fibre content on the mechanical properties of glass fibre mat/polypropylene composites. Composites Part A: Applied Science and Manufacturing, **30**, 815–822 (1999).

[15] Jiang X. L., Zhang Y., Zhang Y. X.: Study of dynamically cured PP/MAH-g-EPDM/epoxy blends. Polymer Testing, **23**, 259–265 (2004).

[16] Jiang X. L., Zhang Y., Zhang Y. X.: Study of dynamically cured PP/MAH-g-PP/talc/epoxy composites. Journal of Applied Polymer Science, **99**, 2752–2758 (2006).

[17] Jiang X. L., Huang H., Zhang Y., Zhang Y. X.: Dynamically cured polypropylene/epoxy blends. Journal of Applied Polymer Science, **92**, 1437–1448 (2004).

[18] Avrami M.: Kinetics of phase change-I. General theory. Journal of Chemistry and Physics, **7**, 1103–1112 (1939).

[19] Avrami M.: Granulation, phase change and microstructure kinetics of phase change. III. Journal of Chemistry and Physics, **9**, 177–184 (1941).

[20] Xu W. B., Ge M. L., He P. S.: Nonisothermal crystallization kinetics of polypropylene /montmorillonite nanocomposites. Journal of Polymer Science Part B: Polymer Physics, **40**, 408–414 (2002).

[21] Remiro P. M., Cortazar M., Calahorra E., Calafel M. M.: The effect of crosslinking and miscibility on the thermal degradation of an uncured and an amine-cured epoxy resin blended with poly(ε-caprolactone). Polymer Degradation and Stability, **78**, 83–93 (2002).

[21] George S., Varughese K. T., Thomas S.: Thermal and crystallization behavior of isotactic polypropylene/nitrile rubber blends, Polymer, **41**, 5485–5503 (2000).

[22] Zhang M. L., Liu Y., Zhang X. H. Jianming Gao, Huang F., Song Z. H., Wei G., Qiao J. L.: The effect of elastomeric nano-particle on the mechanical properties and crystallization behavior of polypropylene. Polymer, **43**, 5133–5138 (2002).

eXPRESS Polymer Letters Vol.1, No.5 (2007) 292–298
Available online at www.expresspolymlett.com
DOI: 10.3144/expresspolymlett.2007.42

Preparation of porous carbon particle with shell/core structure

Y. B. Jiang[1,2], L. H. Wei[3], Y. Z. Yu[1], T. Zhao[1*]

[1]Beijing National Laboratory for Molecular Sciences, Laboratory of Advanced Polymer Materials, Institute of Chemistry, Chinese Academy of Sciences, Beijing 100080, P. R. China
[2]Graduate University of Chinese Academy of Sciences, Beijing 100039, P. R. China
[3]Department of Chemistry, Zhengzhou University, Zhengzhou, 450001, P. R. China

Received 12 March 2007; accepted in revised form 19 April 2007

Abstract. Porous carbon particles with a shell/core structure have been prepared successfully by controlled precipitation of the polymer from droplets of oil-in-water emulsion, followed by curing and carbonization. The droplets of the oil phase are composed of phenolic resin (PFR), a good solvent (ethyl acetate) and porogen (Poly(methyl methacrylate), PMMA). The microstructure was characterized in detail by scanning electron microscopy (SEM), transmission electron microscopy (TEM), nitrogen adsorption, and thermo gravimetric analysis (TGA). The obtained carbon particles have a capsular structure with a microporous carbon shell and a mesoporous carbon core. The BET surface area and porous volume are calculated to be 499 $m^2 g^{-1}$ and 0.56 $cm^3 g^{-1}$, respectively. The effects of the amount of porogen (PMMA), co-solvent (acetone) and surfactant on the resultant structure were studied in detail.

Keywords: *polymer composites, phase separation, polymer blend, porous carbon*

1. Introduction

In recent years, there has been growing interest in new applications of porous carbons because of their characteristic physicochemical properties, such as, their large surface area, large pore volume, thermal and chemical stability. Porous carbon particles are of great interest in column packing, filler, hydrogen storage, supercapacitors, catalyst supports and other applications [1].

Several methods have been developed to prepare spherical carbon [2–8]. The solid-templating approach has been widely used for the synthesis of a variety of nanoporous carbon materials [5–9]. Although precise control of pore size and pore structures is desirable, it has several limitations such as incomplete and time consuming infiltration of the precursor, laboring and expensive template removal process. The commercially available and inexpensive Pluronic block copolymers have been used as templates to prepare mesoporous carbon with various pore structures [10, 11], but direct synthesis of porous carbon particles still remains challenging by this method. Polymer as porogen to prepare porous carbon is another efficient method. Yamazaki et al prepared nanostructure carbonaceous material with continuous pores from reaction-induced phase separation of miscible polymer blends [12, 13]. As PFR interacts strongly with PMMA via hydrogen bonds, the miscibility of PMMA to PFR is perfect, and the phase separation occurs after the curing reaction has advanced to some extent. After PMMA removal and carbonization, the carbonaceous materials with continuous pores can be obtained. Furthermore, porous carbon materials having hierarchically structures have

---

*Corresponding author, e-mail: tzhao@iccas.ac.cn

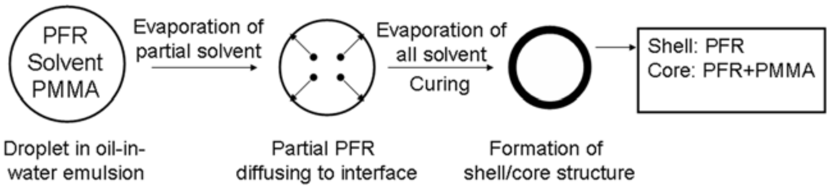

Figure 1. Schematic illustration for capsular structure formation

attracted much interest because of their special character [2, 5, 8].

In this paper, we prepared carbon particles with a microporous carbon shell and a mesoporous carbon core through the method called 'internal phase separation' within the droplets of an oil-in-water emulsion. This method has been used in several reported works. Mathiowitz et al prepared double-walled microspheres by this one-pot method for controlled drug release [14, 15]. Vincent et al prepared a series of polymer microcapsules with liquid cores also by this method [16–18]. In our work, PFR has been used as the shell material, and PMMA as the porogen. As described by Solomon et al, the PMMA domain size in the blends (PFR/PMMA) before curing was 2 to 3 nm and it became 20 to 30 nm after full curing [19]. The process for the formation of the shell/core structure is illustrated in Figure 1. The organic phase containing PFR and PMMA was emulsified in the aqueous surfactant. After solvent removal, hydrophilic PFR preferred to diffuse to the interface of oil-water. But because of good miscibility of PFR and PMMA, partial PFR retained to blend with PMMA and the capsule structure formed with PFR shell and blends of PFR/PMMA core. After carbonization, the final products with microporous carbon shells and mesoporous carbon cores were prepared. The carbon materials with special structures in our work will show advantages in many fields such as controlling release, hydrogen storage, electrochemical double-layer capacitors and so on.

2. Experiment

2.1. Materials

Phenol, formaldehyde (37% aqueous solution) and hexamethylenetetramine were purchased from Beijing Yili Chemicals Factory and used to synthesize phenolic resin. Poly(methyl methacrylate) (PMMA, Aldrich, $M_w = 10{,}000$) was used as the porogen. Gum arabic and sodium dodecyl sulfate (SDS, Tianjin Kemiou Chemical Regents Factory, China) were used as emulsifiers. The solvents used were supplied by Beijing Chemicals Factory, China. All the reagents were of analytical grade and used as received. Doubly deionized water was used as the aqueous medium.

2.2. Synthesis of phenolic resin

The PFR used as the carbon precursor was synthesized and purified as described by Brode [20]. In a typical synthesis, the mixture of phenol (50 g), aqueous formaldehyde (50 g), hexamethylenetetramine (4.5 g), gum arabic (0.5 g) and water (27.5 g) was charged into a three-necked flask equipped with a mechanical stirrer, a thermometer and reflux condenser. The reaction temperature was maintained at 85°C in a water bath for 70 min. The obtained particulate resol was collected by filtration, washed with distilled water for three times and dried at 40°C for 2 h.

2.3. Preparation of porous carbon

PFR was dissolved in the mixture of ethyl acetate and acetone, and then PMMA was added. Aqueous surfactant solution was charged into a three-necked round-bottomed flask equipped with a mechanical stirrer. The organic solution was added to the aqueous surfactant solution, and the mixture was emulsified mechanically at a rate of 3000 rpm to form an oil-in-water emulsion. After agitation lasting for 1h at 25°C, the diluted emulsion was evaporated for 40 min at 30°C under reduced pressure, followed by transferring into a Teflon-lined autoclave, treated at 130°C for about 6 h and another 6 h at 150°C, then allowed to cool down to room temperature gradually. The resultant microsphere dispersion was collected with centrifugation, and then washed with distilled water, ethanol, and ethyl acetate, finally dried in vacuum oven for 10 h at 60°C. The solid sample obtained was carbonized under a nitrogen atmosphere at 800°C for 4 hours at a heating rate of 1°C min^{-1} to obtain porous carbon materials.

2.4. Characterization

SEM Scanning electron microscopy (SEM, HITACHI S-4300, Japan) was used to investigate the morphology of the products. One drop of the microsphere dispersion was placed on a stainless steel SEM stub and allowed to air-dry overnight. Before observation, the dried sample was coated with a layer of gold with a thickness of approximately 10 nm.

TEM Transmission electron microscopy (TEM) pictures were taken on a JEOL 2010 microscope (Japan) with an acceleration voltage of 200 kV. Samples for TEM measurements were diluted and mounted on 400-mesh carbon-coated copper grids and left to dry at room temperature.

Nitrogen sorption Nitrogen sorption was performed on a Micromeritics ASAP 2020M Porosity Analyzer. The samples were degassed at 250°C for 6 h before the measurement. The specific surface area was determined by the Brunauer-Emmett-Teller (BET) method. The BJH (Barret-Joyner-Halenda) method was applied to analyze the mesopore size distributions using the adsorption branch.

TGA Thermo gravimetric analysis (TGA, Netzsch STA409pc) was employed to monitor the degradation behavior of as-prepared products. The sample was heated at a heating rate of 10°C min^{-1} in N_2 atmosphere.

3. Results and discussion

3.1. Characterization of porous carbon particles

TGA analysis was employed to monitor the degradation behavior of PFR, PMMA and as-prepared blending microsphere. Notable weight loss of approximately 99% (Figure 2) is observed in the temperature range of 300~400°C for pure PMMA, suggesting that most of the templates can be decomposed under nitrogen before 400°C. Compared with the TGA curve of PFR, the blending microsphere has a lower mass residue, which is mainly attributed to the degradation of PMMA. Therefore, simple heating treatment can be utilized to efficiently decompose and remove the porogen (PMMA) while generating porosity and maintaining an open framework.

Figure 3 shows representative SEM images of as-prepared microsphere and corresponding porous carbon particles. As seen in the images, the polymer and carbon particles are spherical in morphology with polydisperse particles sizes that range from less than 100 nm to greater than 1um. Figure 3a shows the composite particles prepared from the PFR/PMMA blend (63/37 in weight). These microspheres have smooth surface with no pores or defects. After carbonization, as shown in Figure 3b, the obtained carbon particles can be observed shrinking on the surface, but still with no visible pores or defects. When carbon particles were fractured (shown in Figure 3c and d), obvious shell/core structure was observed. Small carbon particles interconnected to form the mesoporous structure surrounded by the microporous carbon shell. The formation of the capsule structure can be attributed to the two phase separation processed: solvent evaporation induced phase separation and curing induced phase separation. As shown in Figure 1, after solvent removal, hydrophilic PFR diffused to the interface of oil-water. But because of good miscibility of PFR and PMMA, the capsule structure was formed with a PFR shell and blends of PFR/PMMA core. After curing, phase separation occurred in the core, and PFR shell was preserved. Therefore, after PMMA removal and carbonization, the final structure was obtained.

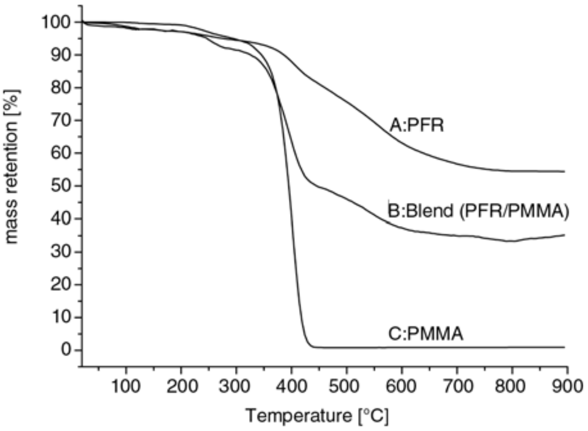

Figure 2. TGA thermograms of PFR, PMMA and blending microspheres. The composition of PFR/PMMA blends was 63/37 in weight

Nitrogen adsorption-desorption isotherms and the resulting pore size distribution are shown in Figure 4. The isotherms are similar to type IV isotherms with a hysteresis loop and a steep adsorption step at a relative pressure of 0.9. The non-parallel hysteresis reflects a non-uniform pore connectivity that is due to the existence of some larger pores. The resulting pore size distribution displays that most of mesopore is about 4 nm and a small quantity of

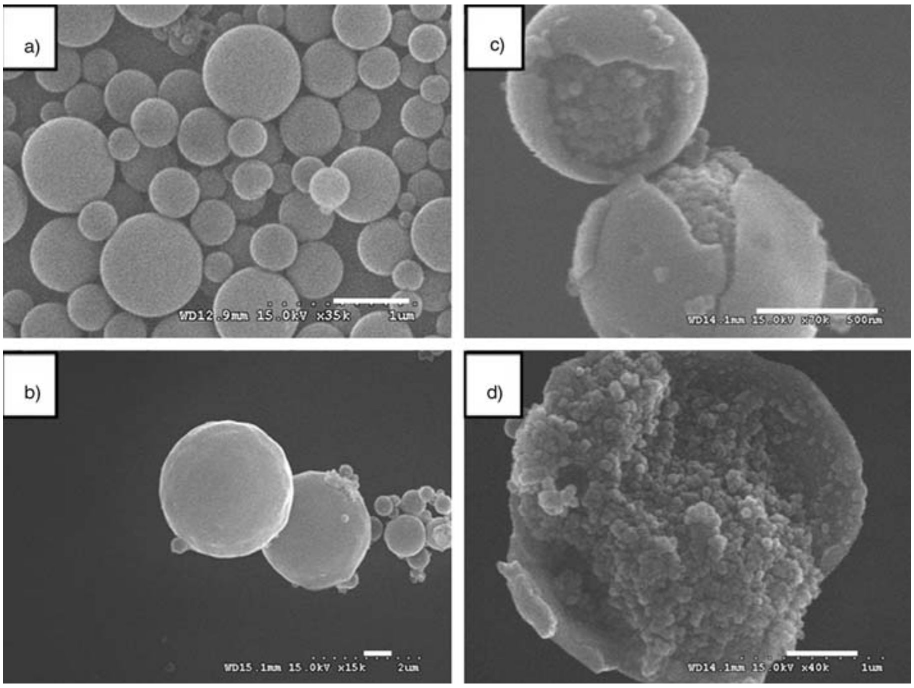

Figure 3. SEM images of as-prepared PFR/PMMA blending microspheres (a) and carbon particles (b, c, d). The composition of PFR/PMMA blends was 63/37 in weight. The scale bar is 500 nm

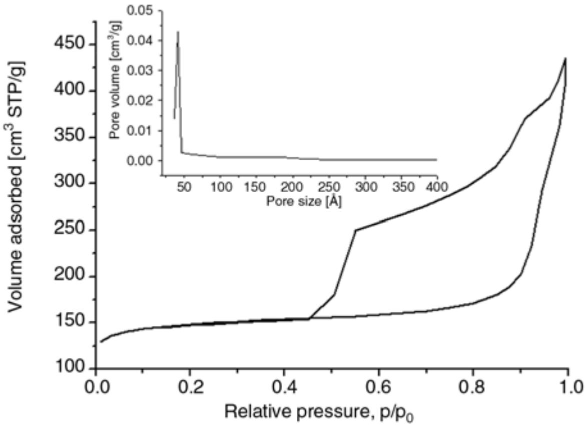

Figure 4. Nitrogen adsorption/desorption isotherms and pore size distribution (insets) for carbon particles. The composition of PFR/PMMA blends was 63/37 in weight

larger pores less than 25 nm exist, which agrees with the desorption isotherm in Figure 4. The calculated BET surface area and pore volume of the carbon particles is 499 $m^2 g^{-1}$ and 0.56 $cm^3 g^{-1}$, respectively.

3.2. Effect of the composition of phenolic resin/PMMA blends

The component of blends (PFR/PMMA) is the most important factor to the final structure of carbon particles. Figure 3 shows the images of carbon with low PMMA content. But when increasing the PMMA content (50/50) as shown in Figure 5, the similar structure as shown in Figure 3 is formed, but the core size is smaller than that of the shell, and the hollow carbon sphere with a movable porous carbon core is obtained. Furthermore, when the amount of PMMA increased to 37/63, no spherical morphology is observed. Only nanosheet and small carbon particles are contained in the SEM images. From these fragments, we conclude the formation of a shell-core structure. However because of the thinner shell wall and smaller core, the strength of the shell is not enough to maintain the spherical shape. The results can be explained from the phase separation by solvent evaporation. When the amount of PMMA increased, both the amount of PFR diffusing to the oil-water interface, and that remaining in the core, decreased. Carbonization removed all the PMMA and about 50% of the PFR, the large amount of mass loss of the composite finally induced structure collapse.

3.3. Effect of co-solvent content

Ethyl acetate was used as the solvent to prepare the materials. However, a weak polarity makes it an unsuitable solvent for PFR. Acetone was added as the co-solvent. We studied the effect of the amount of acetone on the structure of final carbon particles. Figure 6 shows the SEM images of carbon particles

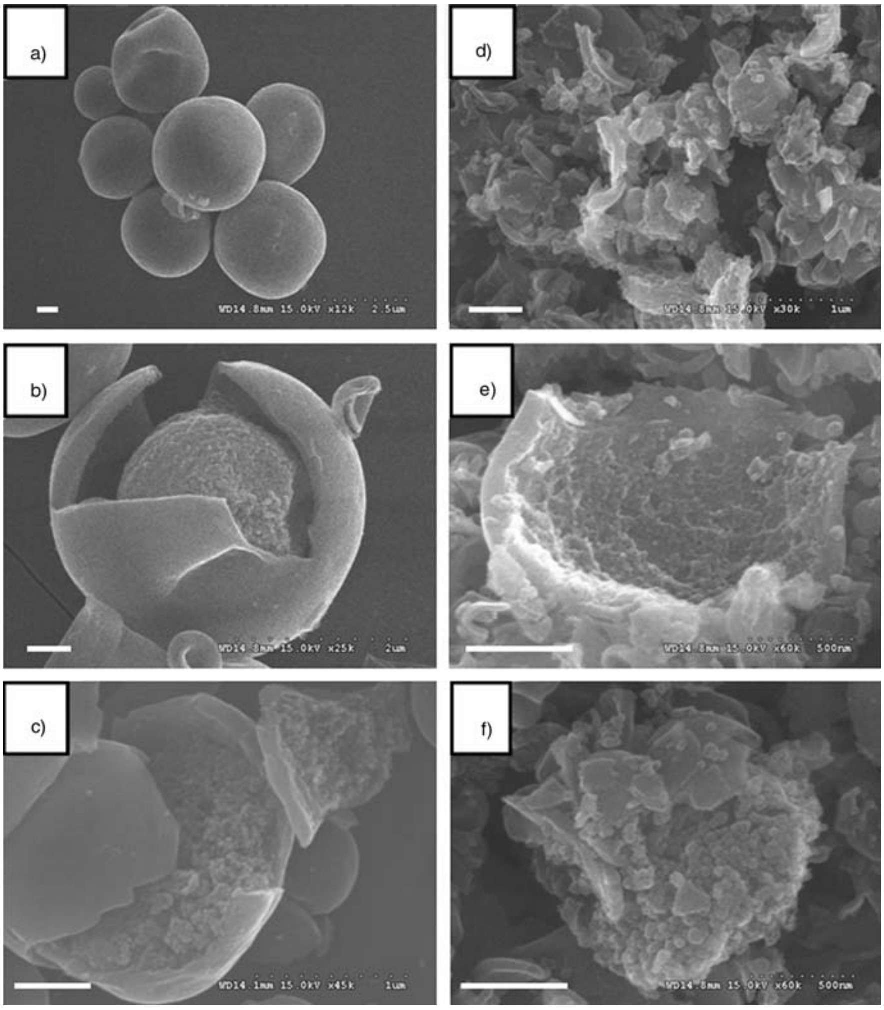

Figure 5. SEM images of obtained carbon with different composition of PFR/PMMA blends in weight. a, b, c: 50/50; d, e, f: 37/63. The scale bar is 500 nm

prepared with different amounts of acetone added. With the increase of amounts of acetone, the distribution of particle size narrowed, and the average particle diameter increased obviously (Figure 6a, b). But with the further increase of acetone, the distribution of particle size widened. These results suggest that the content of acetone can affect the emulsification process, and therefore affect the final particle morphology. This is consistent with the reported results [16].

3.4. Effect of surfactant content

The structure shown in Figure 3 was prepared from the solution emulsified by 2% gum Arabic and 0.1% SDS as emulsifiers. When changing the emulsifiers' content to 2% gum Arabic and 0.2% SDS, the structure obtained changed much. As shown in Figure 7, the as-prepared polymer microcapsule has a hollow cavity, and there is a narrow channel in the shell wall. The TGA curves and residual mass of the product is similar to that of pure PFR (not shown here), it suggests that the component of the hollow sphere is PFR. The formation of the peculiar structure may result from increasing the surfactant. It decreased the oil/water interfacial tension too much, which would decrease the driving force of polymer diffusion to the oil/water interface. This will lead to the result that the region where the adsorption of polymer is insufficient would be occupied by the surfactant molecular aggregates. After curing and washing with the solvent, PMMA escaped from the core, and was removed by the solvent. Finally, a cavity and a channel were left. Further study on the formation mechanism and application potential are in progress.

4. Conclusions

Porous carbon particles have been prepared by the method of polymer blend and internal phase sepa-

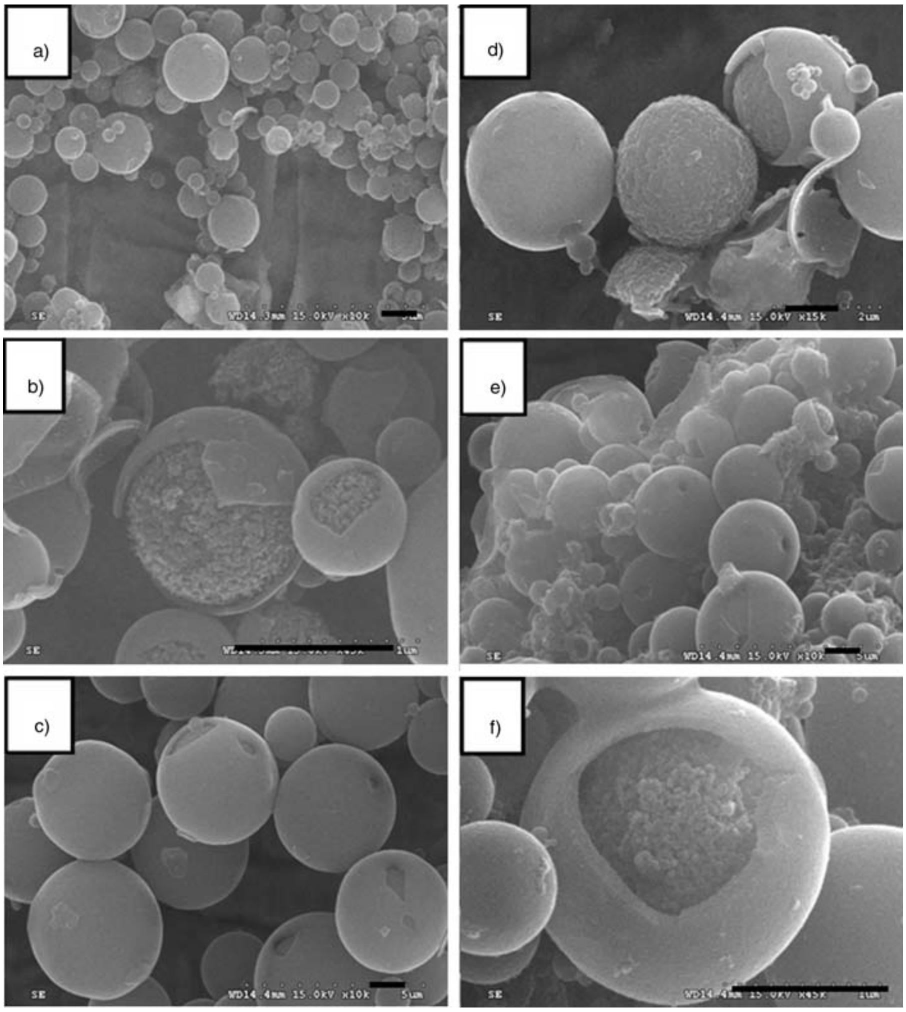

Figure 6. SEM images of obtained carbon with different content of acetone added. a, b: 20%; c, d: 33%; e, f: 50%. The scale bar is 1 μm

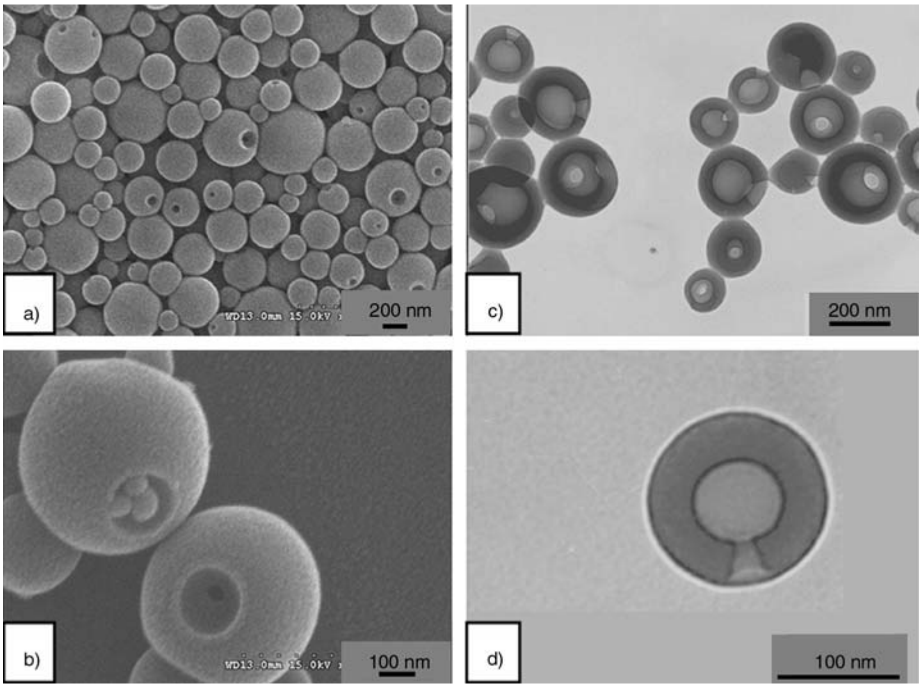

Figure 7. SEM (a, b) and TEM (c, d) images of obtained hollow carbon particles with one channel on the shell

ration. PFR was used to serve as the carbon precursor and PMMA as porogen. Through emulsification and solvent removal, the capsular structure was obtained with PFR as the shell and the blend of PFR/PMMA as core. After heat treatment in nitrogen, porous carbon particles with microporous carbon shells and mesoporous carbon cores were formed. The content of PMMA affected the microstructure and the mechanical strength of the resultant carbon materials. The addition of a co-solvent can affect the emulsification process, and appropriate acetone amount can produce carbon particles with narrow size distributions. Varying the surfactant amounts, hollow PFR microspheres with one channel on the shell can be prepared. We believe that carbon materials in our work may find potential applications in such areas as column packing, hydrogen storage and electrochemical double-layer capacitors, etc.

References

[1] Lee J., Kim J., Hyeon T.: Recent progress in the synthesis of porous carbon materials. Advanced Materials, **18**, 2073–2094 (2006).

[2] Hampsey J. E., Hu Q. Y., Rice L., Pang J. B., Wu Z. W., Lu Y. F.: A general approach towards hierarchical porous carbon particles. Chemistry Communications, (29), 3606–3608 (2005).

[3] Fujikawa D., Uota M., Yoshimura T., Sakai G., Kijima T.: Surfactant-templated synthesis of resorcinol-formaldehyde polymer and carbon nanocomposite: nanospheres and nanowires. Chemistry Letters, **35**, 432–433 (2006).

[4] Xia Y. D., Mokaya R.: Ordered mesoporous carbon hollow spheres nanocast using mesoporous silica via chemical vapor deposition. Advanced Materials, **16**, 886–891 (2004).

[5] Arnal P. M., Schüth F., Kleitz F.: A versatile method for the production of monodisperse spherical particles and hollow particles: templating from binary core-shell structures. Chemistry Communications, (11), 1203–1205 (2006).

[6] Hampsey J. E., Hu Q. Y., Wu Z. W., Rice L., Pang J. B., Lu Y. F.: Templating synthesis of ordered mesoporous carbon particles. Carbon, **43**, 2977–2982 (2005).

[7] Yang M., Ma J., Ding S. J., Meng Z. K., Liu J. G., Zhao T., Mao L. Q., Shi Y., Jin X. G., Lu Y. F., Yang Z. Z.: Phenolic resin and derived carbon hollow spheres. Macromolecular Chemistry and Physics, **207**, 1633–1639 (2006).

[8] Yoon S. B., Sohn K., Kim J. Y., Shin C. H., Yu J. S., Hyeon T.: Fabrication of carbon capsules with hollow macroporous core/mesoporous shell structures. Advanced Materials, **14**, 19–21 (2002).

[9] Kamil P. G., Mietek J.: Carbons with extremely large volume of uniform mesopores synthesized by carbonization of phenolic resin film formed on colloidal silica template. Journal of the American Chemical Society, **128**, 10026–10027 (2006).

[10] Liang C. D., Dai S.: Synthesis of mesoporous carbon materials via enhanced hydrogen-bonding interaction. Journal of the American Chemical Society, **128**, 5316–5317 (2006).

[11] Meng Y., Gu D., Zhang F. Q., Shi Y. F., Cheng L., Feng D., Wu Z. X., Chen Z. X., Wan Y., Stein A., Zhao D. Y.: A family of highly ordered mesoporous polymer resin and carbon structures from organic-organic self-assembly. Chemistry of Materials, **18**, 4447–4464 (2006).

[12] Yamazaki M., Teduka M., Ikeda K., Ichihara S.: Preparation of carbon materials with coral-like continuous pores using miscible polymer blends. Journal of Materials Chemistry, **13**, 975–977 (2003).

[13] Yamazaki M., Kayama M., Ikeda K., Alii T., Ichihara S.: Nanostructured carbonaceous material with continuous pores obtained from reaction-induced phase separation of miscible polymer blends. Carbon, **42**, 1641–1649 (2004).

[14] Pekarek K. J., Jacob J. S., Mathiowiz E.: Double-walled polymer microspheres for controlled drug release. Nature, **367**, 258–260 (1994).

[15] Pekarek K. J., Jacob J. S., Mathiowiz E.: One-step preparation of double-walled microspheres. Advanced Materials, **6**, 684–687 (1994).

[16] Loxley A., Vincent B.: Preparation of poly(methylmethacrylate) microcapsules with liquid cores. Journal of Colloid and Interface Science, **208**, 49–62 (1998).

[17] Atkin R., Davies P., Hardy J., Vincent B.: Preparation of aqueous core/polymer shell microcapsules by internal phase separation. Macromolecules, **37**, 7979–7985 (2004).

[18] Dowding P. J., Atkin R., Vincent B., Bouillot P.: Oil core-polymer shell microcapsules prepared by internal phase separation from emulsion droplets. I. characterization and release rates for microcapsules with polystyrene shells. Langmuir, **20**, 11374–11379 (2004).

[19] Zhang X., Solomon D. H.: Phase structures of hexamine cross-linked novolac blends. 1. blends with poly(methyl methacrylate). Macromolecules, **27**, 4919–4926 (1994).

[20] Brode G. L., Kopf P. W., Chow S. W.: Phenolic thermospheres: Chemical design and principles. Industrial Engineering Chemistry Products Research and Development, **21**, 142–145 (1982).

eXPRESS Polymer Letters Vol.1, No.5 (2007) 299–307
Available online at www.expresspolymlett.com
DOI: 10.3144/expresspolymlett.2007.43

Surface modification and micromechanical properties of jute fiber mat reinforced polypropylene composites

X. Y. Liu, G. C. Dai*

State-Key Laboratory of Chemical Engineering, East China University of Science and Technology, 130 Meilong Road, Shanghai 200237, P. R. China

Received 13 March 2007; accepted in revised form 23 April 2007

Abstract. A new treating method using sodium hydroxide (NaOH) and Maleic anhydride-grafted polypropylene (MPP) emulsion was introduced to treat jute fiber mat in order to enhance the performance of jute/polypropylene (PP) composite prepared by film stacking method. The surface modifications of jute fiber mat have been found to be very effective in improving the fiber-matrix adhesion. It was shown that treatments changed not only the surface topography but also the distribution of diameter and strength for the jute fibers, which was analyzed by using a two-parameter Weibull distribution model. Consequently, the interfacial shear strength, flexural and tensile strength of the composites all increased, but the impact strength decreased slightly. These results have demonstrated a new approach to use natural materials to enhance the mechanical performances of composites.

Keywords: *mechanical properties, jute fiber mat, polypropylene, surface modification, distribution*

1. Introduction

Ecological concern has resulted in a renewed interest in natural materials for their recyclability, light weight and non pollution. Important issues such as recyclability and environmental safety need to be addressed when new materials and products are introduced. Lignocellulosic natural fibers such as flax, hemp, sisal and jute are an interesting, environmentally friendly alternative to the use of glass fibers as reinforcement in engineering composites because of the benefits that these fibers provide over conventional reinforcement materials, and the development of natural fiber composites has been a subject of interest for the past few years [1–4]. These fibers are renewable, nonabrasive, and can be incinerated for energy recovery since they possess a good calorific value and cause little concern in terms of health and safety during handling of fiber products. In addition, they exhibit excellent mechanical properties, low density and are cheap. This good environmental friendly feature makes the materials very popular in engineering markets such as the automotive [5–8] and construction industry [9, 10].

There are several reports about the use of jute as reinforcing fibers for thermosets [11–13] and thermoplastics [14, 15]. The studies of jute fiber composites were carried out mostly in India in early years and jute fiber reinforced thermosets had been the focus of studies. In recent years, natural fiber reinforced thermoplastics were receiving more and more attention because of issues of environmental protection. Fiber treatment and interfacial modification were most frequently studied issues aiming to improve the properties of short or long fiber reinforced composites. However, interfacial modification of natural fiber mat reinforced thermoplastics was rarely reported elsewhere and there is no report

---

*Corresponding author, e-mail: lxy_7945@163.com on surface modification of natural fiber mat using NaOH solution and MPP emulsion. Composite strength and stiffness generally increased as a consequence of the improved mechanical properties of the fibers by NaOH treatment under isometric conditions. Impact damping was distinctly affected by the shrinkage state of the fibers during the NaOH treatment because of its influence on yarn toughness [11]. Silane treatment of fibers led to increased tensile, flexural strength, and Young's modulus of composites by up to 30% [12]. MPP was widely used as a coupling agent to improve the adhesion between natural fiber and PP, and the effect of MPP and fiber length on the performance of a jute/PP composite system has been investigated. The influence of the fiber-matrix adhesion in jute fiber-reinforced polypropylene on the materials behavior under fatigue and impact loadings was investigated by some authors [15]. A novel hybrid coupling agent made from silane coupling agent and MPP were found to be a good adhesion promoter to improve natural fiber reinforced powder polypropylene composites [16].

This paper introduces a new treating method for jute fiber mat by using NaOH and MPP emulsion to enhance the properties of jute/PP composite. Interfacial shear strength (IFSS) values were measured using a microbond test. Surface characterization using Scanning Electron Microscopy (SEM) and Fourier Transform Infrared (FT-IR) spectroscopy was carried out to observe the modification on fiber surfaces after the treatment and the effect of NaOH treatment on jute fibers in terms of their diameter and mechanical strength is explained.

2. Experimental

2.1. Materials

Polypropylene (Y3700) with a melt flow index of 37 g/10 min and density of 0.908 g/cm^3, supplied by Shanghai Jinshan petrochemical company was used in this work. MFI was measured under temperature of 230°C. Polypropylene wax with an average molecular weight of 5000~8000 were obtained from Shanghai Jinshan Plastic company to prepare MPP emulsion. Jute fibers were obtained from Zhenjiang Lida Fiber Company. The fibers were washed with water and dried in an air oven at 70°C for 8 h and a vacuum oven at 60°C for 2 h before preparation of composites.

2.2. Preparation of MPP water emulsion

In preparation of MPP emulsion, PP wax and maleic anhydride (MAH) were selected as raw materials and Benzoyl Peroxide (BPO) as initiator. First, PP wax and was put in acetone solution. Stirring and heat were applied to ensure the melting of PP wax. After acetone was vaporized by increasing temperature to 120°C, BPO and MAH mixture dissolved in xylene was added to PP wax melt continuously to initiate reaction. Graft reaction was carried out in xylene solution under reaction temperature of 144°C. After reaction completed, xylene was vaporized and emulsification was carried out by using water and emulsification reagent in high shear dispersing emulsifier for about 2 h. Sodium bicarbonate was also used to counteract some leftover MAH. The MAH content in grafted PP is 7%, which is measured by using the method of chemical titration.

In chemical titration, the grafted PP was dissolved in xylene with additional heating and circumfluence for 8 hours. The superfluous KOH-ethanol solution was added and the surplus solution was titrated by using acetic acid-xylene solution to determine MAH content in grafted PP. Following formula shows how to calculate MAH content.

G = [mol consumption of KOH × molecular weight of MAH/(2 × sample weight)] × 100%

2.3. Preparation of PP/jute composites

PP reinforced by non-woven jute fiber mat was manufactured using a film-stacking method. In this film-stacking method, 2 layers of pre-dried non-woven jute mats in combination with 3 layers of PP films were stacked alternately, with fiber content of 38 wt%. Impregnation of the non-woven mats was achieved by applying heat (200°C) and pressure (5 MPa) in a continuous molding machine (manufactured by Polymer Processing Laboratory).

The laminates were prepared through the period of preheating, hot pressing and cooling continuously. They were then cut into certain shape and prepared to specimens for mechanical tests by using a milling machine. The size of the specimens was determined according to ASTM standards.

2.4. Chemical treatment

2.4.1. Alkali treatment

NaOH which was used for treatment was provided by Shanghai Feida trading company. The fiber mats were put in a stainless steel vessel containing solution of NaOH with different concentration of 2 wt% and 5 wt% and a given pressure was applied to ensure good impregnation of NaOH solution. This was kept for 1 h, after which the fiber mats were washed thoroughly with water to remove the excess of NaOH on the fibers. Final washing was carried out with distilled water and the fiber mats were finally air dried at 70°C for 8 h and vacuum dried at 60°C for 2 h.

2.4.2. Silane treatment

The untreated fiber mats were placed in a stainless steel vessel containing solution of silane coupling agent (KH550) with concentration of 2 wt% for 1 h. Chemical formula of KH550 is $NH_2(CH_2)_3Si(OC_2H_5)_3$ supplied by Shanghai Yaohua industrial trading company. The hydrolysis takes place in water for about 1 h. The mats were then dried in an air oven at 70°C for 8 h and then vacuum oven at 60°C for 2 h.

2.4.3. NaOH + MPP emulsion treatment

The jute fiber mat was first treated by NaOH under guideline of alkali treatment above and then was soaked in 2 wt% MPP water emulsion for 1 h to ensure MPP particles adhered on surface of the jute fibers. The mats were then dried in air and vacuum oven at 60°C.

2.5. Fiber surface characterization

The surface topography of fibers was investigated using a scanning electron microscope (SEM), (SEM Model JSM-6360LV, JEOL Corporation Japan). The FTIR spectra of raw and surface treated natural fibers were recorded in a Nicolet AVATAR360 FT-IR spectrophotometer (Nicolet Corporation USA).

2.6. Mechanical characterization

The tensile properties, such as tensile strength, elongation at break, and tensile modulus of the composites were evaluated following the ASTM D638 method with a crosshead speed of 2 mm/min. The ASTM D790 method was followed to evaluate the flexural properties and ASTM D256 method for evaluation of impact strength. All tests were carried out at room temperature (20±2°C) and with a relative humidity between 25 and 50%.

The tensile properties of jute fibers were measured using a single fiber tensile testing machine (Model YG004A, Changzhou No2 Weaving Machine Factory). Specimen gauge length was 20 mm. One hundred fibers were tested in order to give the probability distribution of their tensile strength.

The interfacial shear strength (IFSS) of specimens was measured by a microbond technique [17]. All specimens were equilibrated at standard conditions of 21°C and 65% relative humidity for more than 24 h before the microbond test on a mechanical testing machine using an iron slice with a round aperture. The diameter of the aperture is larger than that of a fiber and smaller than the size of a micro droplet in order to pull out the fiber from micro droplet. The schematic of the microbond test rig is shown in Figure 1. The diameter, d, and embedded length, l, of the fiber were measured prior to the microbond test using an optic microscope and an image processing analysis program called UTHSCA Imagetool. As the fiber was pulled out, the shear load at the fiber/micro droplet interface increased. Debonding occurred when the load exceeded the interfacial bond strength. The average IFSS, τ, was calculated using the Equation (1):

$$\tau = \frac{F}{\pi \cdot d \cdot l} \tag{1}$$

where F is the load to debond the micro droplet. It was assumed that the shear strength was uniform along the entire fiber/micro droplet interface. Fifty

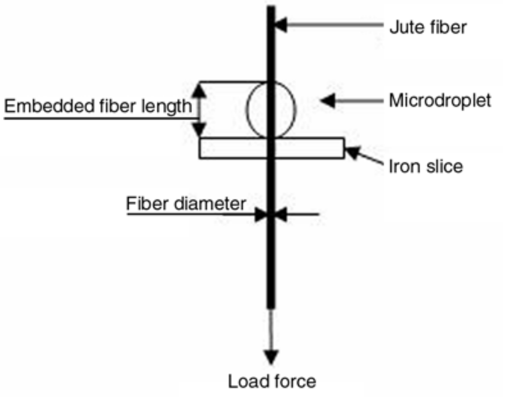

Figure 1. Schematic of the microbond test rig

successful tests were conducted to obtain statistical results.

3. Results and discussions

3.1. Fiber surface characterization

The surface structures of untreated and alkali treated jute fibers are shown in Figure 2. From comparison of the SEM-micrographs, it seems that the untreated fibers had smooth surfaces (Figure 2a and 2c), having some impurities and layers over layers of sheet substances like wax or fatty substances whereas the surfaces of the treated fibers were rough (Figure 2b and 2d). It can also been seen that a number of lumpy strips existed on the surfaces of the treated fibers, which might be due to mercerization function of NaOH, resulting in the partial removal of wax or fatty substances. It is a well-known fact [18] that there are binder lignin and fatty substances which hold the unit cells firmly in a fiber. After alkali treatment, the crystallinity of fibers increases [2], which might be attributed to the removal of the cementing materials, leading to a better packing of cellulose chains. Additionally, treatment of the fibers with NaOH might lead to a decrease in the spiral angle and increase in molecule orientation.

Untreated and treated jute fibers were analyzed by FTIR spectroscopy using attenuated total reflectance (ATR) scanning with a resolution of 2 cm^{-1} and a scanning range from 4000 cm^{-1} to 450 cm^{-1}. The FTIR spectra of untreated and treated jute fibers are shown in Figure 3. NaOH and MPP emulsion treated jute fiber was heated to 160°C before characterization in order to initiate the reaction between jute and MPP wax. It can be noted that there is an absorption band at ~1730 cm^{-1} and 1240 cm^{-1} for the untreated jute fibers, which no longer exists for NaOH treated fibers. The hemicelluloses contain groups that absorb in the carbonyl region and ester group on surface of the fiber. They are soluble in aqueous alkaline solutions. During alkali treatment, a substantial portion of uronic acid and fatty substances might be removed resulting in disappearance of this peak at ~1730 cm^{-1} and 1240 cm^{-1}. After treating with alkali and MPP emulsion, the peak at ~1733 cm^{-1} and 1241 cm^{-1} appears again, which is consistent with the work reported by Mohanty *et al.* [19]. This may be attributed to presence of ester functionality in the MPP treated jute fibers due to carbonyl functionality in MPP. The schematic representation of the possible reaction of MPP with jute fiber is represented in Figure 4.

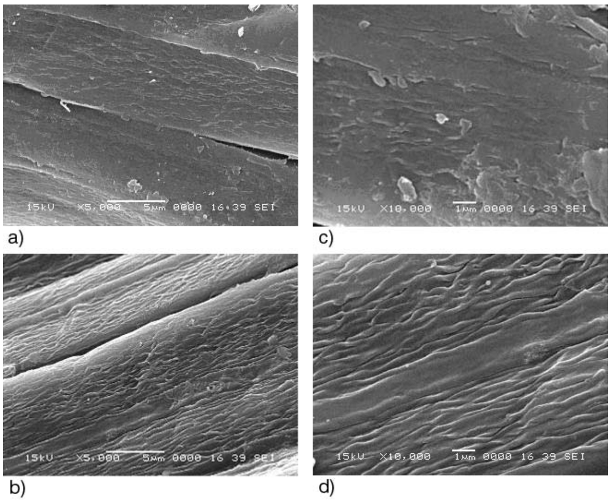

Figure 2. SEM micrographs of: (a) untreated jute (5000×); (b) 5%NaOH treated jute (5000×); (c) untreated jute (10000×); and (d) 5%NaOH treated jute (10000×)

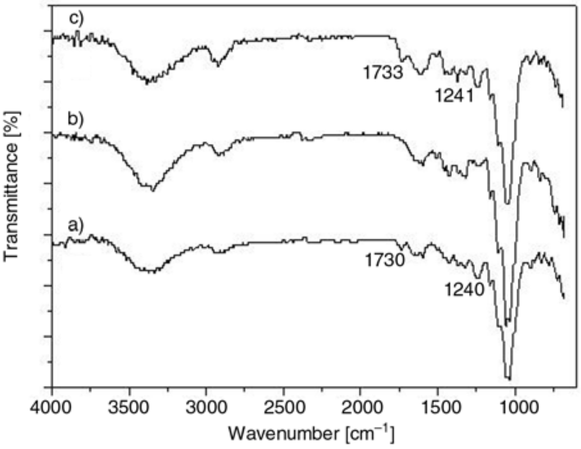

Figure 3. FTIR spectra of: (a) untreated jute; (b) alkali treated jute; and (c) alkali and MPP emulsion treated jute fibers

3.2. Distribution characterization of jute fiber

Figure 5 shows the cumulative diameter distribution of the untreated jute fibers and treated jute fibers including 2 wt% KH550 treated, 2 wt% NaOH treated and 5 wt% NaOH treated, respectively. In each kind of fiber, 100 fiber samples were selected to conduct the experiment. The experimental diameter data were estimated from $F(N) = i/(N+1)$, where N is the total number of samples tested and i is the number in ascendingly ordered

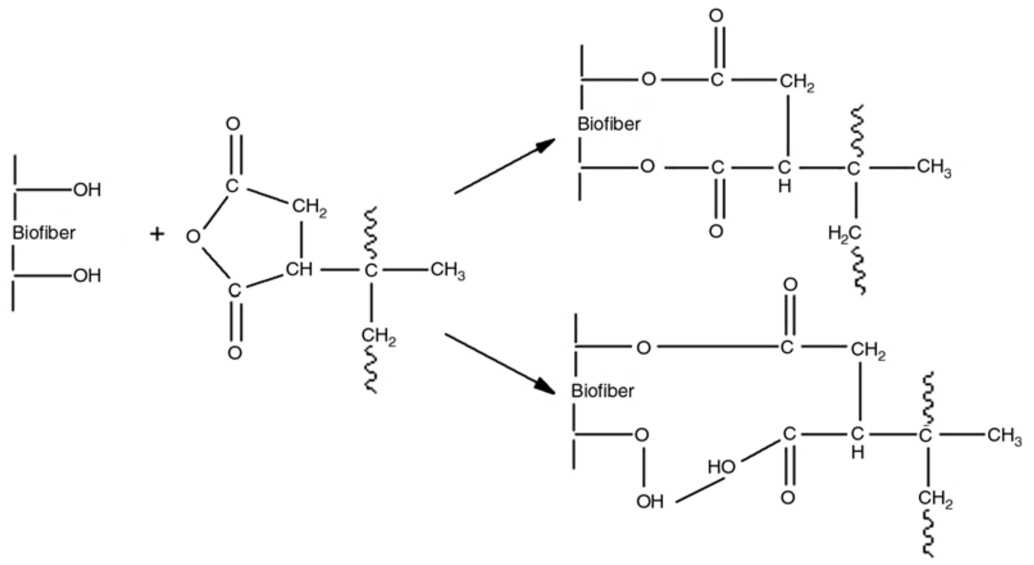

Figure 4. Possible reaction of natural/biofiber with MPP

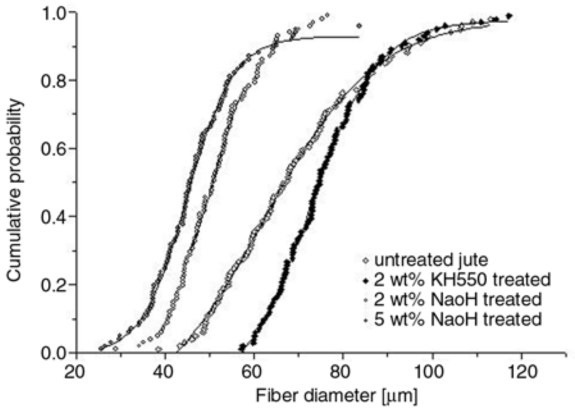

Figure 5. Diameter distribution of untreated and treated jute fiber

diameter data. It was easily noted that the distribution of the diameter shifted significantly to the left side under the treatment with NaOH and to the right side under the treatment with KH550. The average diameter of the untreated fibers is 62 µm whilst that of the fibers treated by 2 wt%, 5 wt% NaOH and 2 wt% KH550 is 51 µm, 47 µm and 72 µm, respectively. The bigger diameter of untreated jute fibers resulted from layers of wax and fatty substances on their surface and a large numbers of micro fibrils in one fiber bundle. The reduced diameter of NaOH treated jute fibers can be attributed to removal of plentiful wax and fatty substances and cementing materials in fiber bundles while the increased diameter of KH550 treated jute fibers can be attributed to reaction between jute fiber and coupling agent taking place on the surface of the fibers.

The fiber strength values were further analyzed statistically using a two-parameter Weibull distribution to describe the fiber strength distribution. The statistical variability of the tensile strength of jute fibers can be written as Equation (2):

$$P = 1 - \exp\left[-L\left(\sigma - \frac{\sigma_u}{\sigma_0}\right)^w\right] \qquad (2)$$

where P is the cumulative probability of failure of a fiber length of L at an applied stress σ, σ_0 is the characteristic strength of a unit which is also called Weibull scale parameter, and σ_u is the lowest value of the strength and is set to zero for simplification. Hence the two-parameter Weibull equation can be re-written as Equation (3):

$$P = 1 - \exp\left[-1\left(\frac{\sigma}{\sigma_0}\right)^w\right] \qquad (3)$$

where w is the shape parameter or Weibull modulus which defines the variability in the strength values. A low value of the Weibull modulus indicates a high variability. Rearrangement of the two-parameter Weibull equation shown leads to the Equation (4):

$$\ln\left[\ln\frac{1}{1-P}\right] = w\ln\sigma - w\ln\sigma_0 + \ln L \qquad (4)$$

where w and σ_0 can be found from the slope and intercept of the plot ln[ln1/(1 – P)] versus lnσ. The Weibull plots for untreated and treated jute fibers are shown in Figure 6a. A good fit was observed with this distribution, as it was evident from the

Table 1. Tensile strength of jute fibers and Weibull parameter

Jute fibers	Tensile strength±SD* [MPa]	Weibull modulus	Characteristic strength [MPa]
Untreated	250±119	2.2	238
2 wt% NaOH treated	325±132	2.6	304
5 wt% NaOH treated	389±150	2.7	355
2 wt% KH550 treated	326±145	2.5	301

*SD, standard deviation

closeness to the best-fit line. Weibull parameter obtained from the Weibull plots are given in Table 1. It can be easily noted that before the treatment, Weibull modulus for jute fiber is 2.2 while after being treated with 2 wt% KH550, 2 wt% NaOH and 5 wt% NaOH, the Weibull modulus are 2.5, 2.6 and 2.7 respectively, indicating a obvious variability in strength of untreated fibers compared to chemically treated fibers. It can be also seen that the Weibull modulus values for jute fibers are much lower compared to synthetic fiber such as carbon fiber [20], which indicates the non-homogeneous nature of natural fibers which in turn is due to the predominance of defects within their structures. Similar results were reported earlier for other natural fibers by some authors [21–23]. The tensile strength of fibers increases obviously after treatment of NaOH. Generally speaking, a fiber with larger cross-section area should have greater chance to have a bigger flaw. Therefore, it is expected to be weaker than that with a smaller cross-section area. The cross-section area of jute fibers decreases after they were treated by NaOH, which could be concluded from the diameter change of jute fibers. This can also be proved by Weibull plots in Figure 6a, where the curve shifts right after treatment. In Figure 6b, fiber strength exhibited a scattering with various diameters for different kind of fibers. Scattering in strength of natural fibers may be influenced by inhomogeneous distribution of their chemical structure and inherent properties of composite materials.

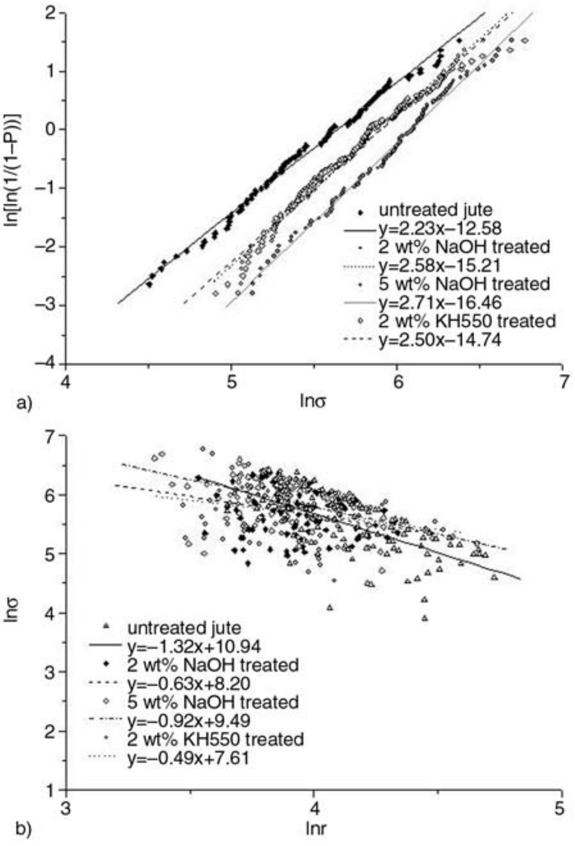

Figure 6. (a) Weibull plots for untreated and differently treated jute fibers. (b) Variation of tensile strength of jute fibers as a function of fiber diameter

3.3. Mechanical and micromechanical properties of the composites

The mechanical properties including flexural strength, tensile strength and impact strength in association with interfacial shear strength of jute fiber/PP composites formed with different treating methods is shown in Table 2.

The mean IFSS between untreated jute fiber and PP is 3.49 MPa, which is much lower than the IFSS between synthetic fiber and thermosets [24]. The IFSS depends mainly on two factors: mechanical interlocking and chemical bonding. In the case of untreated jute fiber/PP, chemical bonding is considered to be rather weak because of incompatibility between hydrophobic resin and –OH group on the fiber. As a result, the IFSS is mainly attributed to the high surface irregularity of jute fibers and the resulting mechanical interaction.

After treating with alkali solution, the possible reaction between –OH groups on the fiber and NaOH might greatly diminish water absorption of the fiber, which improved the compatibility between fibers and resin. The IFSS with 2 wt% NaOH, 5 wt% NaOH and 2 wt% KH550 treatment

Table 2. IFSS and mechanical properties of jute fiber mat reinforced PP

Jute fibers	IFSS±SD [MPa]	Flexural strength±SD [MPa]	Tensile strength±SD [MPa]	Impact strength±SD [J m^{-1}]
untreated	3.49±0.32	35.1±1.2	28.4±0.9	65.0±3.2
2 wt% KH550treated	4.27±0.83	43.8±1.7	33.7±1.4	62.8±3.1
5 wt% NaOH treated	4.85±0.64	55.2±2.2	38.1±1.6	57.4±2.9
2 wt% NaOH treated	5.27±0.82	58.3±2.3	36.9±1.5	61.2±3.3
2 wt% NaOH + MPP emulsion	9.00±1.47	59.0±2.0	42.2±2.3	54.1±2.5

are approximately 51%, 39% and 22% greater than that of the untreated fibers. It should be noted that coupling agents can play a role of bridging between fibers and resins. After treating with NaOH and MPP emulsion, the IFSS increased dramatically to 9.00 MPa. In this case, the effect of chemical bonding on the IFSS might be significant as reaction could occur between fiber and coupling agents.

The level of adhesion between fiber and matrix greatly affects the mechanical properties of the composites. The flexural strength of the untreated composite increases correspondingly with the treatment by KH550, NaOH and NaOH + MPP emulsion. Similarly, the tensile strength of the untreated fibers also increases simultaneously. However, the impact strength seemed to decrease slightly after each treatment. These results indicate that surface modification improved the interfacial adhesion between fibers and matrix, resulting in the higher flexural strength and tensile strength as well as the modulus but slightly lower impact strength. In other words, the rigidity of the fibers after the treatments increased but their toughness reduced. The reason why mechanical properties of jute fiber reinforced PP are improved may be different in terms of different treatment. In alkali treatment, reaction between jute fiber and NaOH can be shown in following ways:

$$\text{Cell–OH} + \text{NaOH} \rightarrow \text{Cell–O}^{-}\text{Na}^{+} + \text{H}_2\text{O} + \text{impurity}$$

Natural fiber is hydrophilic due to large number of hydroxyl groups in their structure, which makes it incompatible with PP that is hydrophobic. In this reaction, a number of hydroxyl groups can be eliminated, which decreases the tendency of water absorption and improves the compatibility between jute fiber and PP. Besides, the mechanical properties of jute fiber are improved through alkali treatment, which has been proved above. Since the mechanical properties of the reinforcing materials play an important role in composite properties, increasing tensile strength of jute fiber contributes to the improvement of mechanical properties of the composite. As to KH550 and MPP, they play a role like a bridge between jute fiber and PP. The reaction between coupling agent and jute fiber can be displayed in Figure 7, where hydrogen bond is

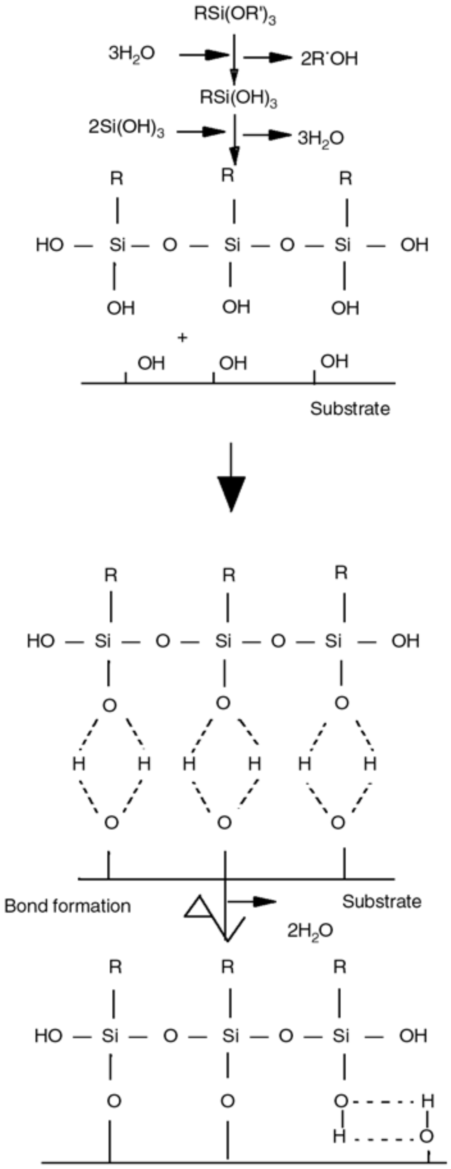

Figure 7. Scheme of reaction between coupling agent and jute fiber

formed. Thus the adhesion between jute fiber and PP is improved, which can contribute to the improving properties of the composite. In reaction between jute fiber and MPP, both chemical (ester bond) and physical interactions (hydrogen bond) are formed. The PP chain of MPP diffuses into the PP matrix through interchain entanglement. The kind of entanglement should be stronger than most of MPP because we applied MPP particles on the surface of the jute fiber through coating of MPP water emulsion and this kind of MPP has a much smaller molecular weight and much higher content of MAH. On the other hand, the maleic anhydride group forms both covalent and hydrogen bonds with the hydroxyl groups of the fiber. These cause better adhesion between the fiber and the matrix. Therefore, the transfer of stress from the matrix to the fibers is improved and lead to highest flexural and tensile properties of PP reinforced with NaOH and MPP emulsion treated jute fiber from among all composites.

The reason why IFSS is in inverse ratio with impact strength of the composites may be speculated as follows: Firstly, the interfacial adhesion is weak before surface modification, which results in a number of voids around fiber surfaces that can be seen from Figure 8. The main reason might be huge difference of surface energy between untreated fiber and matrix. When PP melt reaches fiber surface, some small defects on fiber surface can’t be surrounded by matrix, which leads to formation of voids. After an impact force is applied to the composite, the stress is transferred from the matrix to the fiber surfaces, which causes these voids to become a number of micro crackles. Then absorption of a significant amount of energy by these crackles takes place around the interface of the composites, which consequently exhibits relatively higher impact strength. Although adhesion between fibers and matrix could be greatly strengthened after the fibers are treated, the decrease in size of the pores leads to formation of fewer micro crackles. Under these circumstances, an impact force could cause the composite to crumble as few energy is absorbed by the micro crackles. Moreover, significant stress concentration might exist at the end of a fiber, where the stress concentration could not be dissipated in this area due to its strong adhesion with matrix. With decline of the IFSS, slipping on the interface was possible, which could consume energy and prevent stress concentration. Thus, the impact strength is improved and the elongation of the material is increased at the same time. It is worth mentioning that the composite with balanced rigidity and toughness or with different combination of mechanical properties could be tailor-made, which remains to be proved in future works.

Figure 8. Cross section of untreated jute reinforced PP

4. Conclusions

Treatment of jute fibers with alkali treatment and MPP emulsion has been found to be very efficient in improving the fiber-matrix adhesion in jute fiber mat reinforced PP composites. NaOH treatment removed wax and fatty substances and changed surface topography of the jute fibers through SEM observations and FT-IR spectra. Consequently, the diameter distribution for the fibers changed dramatically after treatment with coupling agent or NaOH. The distribution of strength for untreated and treated jute fiber fits well with Weibull distribution and difference of fiber strength can be explained by Weibull modulus and characteristic strength. There was a strong connection between the interfacial shear strength and the mechanical properties of the jute/PP composites, including flexural strength, tensile strength and impact strength, and the results also showed that combination of NaOH and MPP emulsion is a good adhesion promoter in manufacturing jute fiber mat reinforced PP and controlling interfacial shear strength can be an effective strategy to balance the mechanical properties of the composites.

References

[1] Saheb D. N., Jog J. P.: Natural fiber polymer composites: A review. Advances in Polymer Technology, **18**, 351–363 (1999).

[2] Bledzki A. K., Gassan J.: Composites reinforced with cellulose based fibres. Progress in Polymer Science, **24**, 221–274 (1999).

[3] Eichhorn S. J., Baillie C. A., Zafeiropoulos N., Mwaikambo L. Y., Ansell M. P., Dufresne A., Entwistle K. M., Herrera-Franco P. J., Escamilla G. C., Groom L., Hughes M., Hill C., Rials T. G., Wild P. M.: Current international research into cellulosic fibres and composites. Journal of Materials Science, **36**, 2107–2131 (2001).

[4] Srikanth G., Nangia S.: Development of natural fiber composites in India. in 'Proceedings of Annual Convention and Trade Show, Tampa, USA' 3–6 (2001).

[5] Eastham J.: Natural fibres for the automotive industry in 'Seminar of The Alternative Crops Technology Interaction Network, Manchester, UK' **16**, 142–146 (2001).

[6] Han S. O., Defoort B., Drzal L. T., Askeland P. A.: Environmentally friendly biocomposites for automotive applications in '33rd ISTC Conference, Seattle, USA' **33**, 1466–1477 (2001).

[7] Marsh G.: Next step for automotive materials. Materials Today, **6**, 36-43 (2003).

[8] Chen Y., Chiparus O., Sun L., Negulescu I., Parikh D. V., Calamari T. A.: Natural fibers for automotive nonwoven composites. Journal of Industrial Textiles, **35**, 47–62 (2005).

[9] Head P. R.: Construction materials and technology: A look at the future. Proceedings of the Institution of Civil Engineers: Civil Engineering, **144**, 113–118 (2001).

[10] Bledzki A. K.: New light construction materials. Przemysl Chemiczny, **82**, 548–548 (2003).

[11] Gassan J., Bledzki A. K.: Possibilities for improving the mechanical properties of jute/epoxy composites by alkali treatment of fibres. Composites Science and Technology, **59**, 1303–1309 (1999).

[12] Gassan J., Bledzki A. K.: Effect of cyclic moisture absorption desorption on the mechanical properties of silanized jute-epoxy composites. Polymer Composites, **20**, 604–611 (1999).

[13] Gassan J., Gutowski V. S.: Effects of corona discharge and UV treatment on the properties of jute-fibre epoxy composites. Composites Science and Technology, **60**, 2857–2863 (2000).

[14] Karmaker A. C., Youngquist J. A.: Injection moulding of polypropylene reinforced with short jute fibers. Journal of Applied Polymer Science, **62**, 1147–1151 (1996).

[15] Gassan J., Bledzki A. K.: Possibilities to improve the properties of natural fiber reinforced plastics by fiber modification – jute polypropylene composites. Applied Composite Materials, **7**, 373–385 (2000).

[16] Mohanty A. K., Drzal L. T., Misra M.: Novel hybrid coupling agent as an adhesion promoter in natural fiber reinforced powder polypropylene composites. Journal of Materials Science Letters, **21**, 1885–1888 (2002).

[17] Miller B., Muri P., Rebenfeld L.: A microbond method for determination of the shear strength of a fiber/resin interface. Composites Science and Technology, **28**, 17–32 (1987).

[18] Bismarck A., K. Monhanty A., Aranberri-Askargorta I., Czapla S., Misra M., Hinrichsen G., Springer J.: Surface characterization of natural fibers; surface properties and the water up-take behavior of modified sisal and coir fibers. Green Chemistry, **3**, 100–107 (2001).

[19] Mohanty A. K., Drzal L. T., Misra M.: Engineered natural fiber reinforced polypropylene composites: Influence of surface modifications and novel powder impregnation processing. Journal of Adhesion Science and Technology, **16**, 999–1015 (2002).

[20] Pickering K. L., Murray T. L.: Weak link scaling analysis of high-strength carbon fibre. Composites Part A: Applied Science and Manufacturing, **30**, 1017–1021 (1999).

[21] Panthapulakkal S., Zereshkian A., Sain M.: Preparation and characterization of wheat straw fibers for reinforcing application in injection molded thermoplastic composites. Bioresource Technology, **97**, 265–272 (2006).

[22] Doan T-T-L., Gao S-L., Mader E.: Jute/polypropylene composites I. Effect of matrix modification. Composites Science and Technology, **66**, 952–963 (2006).

[23] Park J.-M., Quang S. T., Hwang B-S., DeVries K. L.: Interfacial evaluation of modified jute and hemp fibers/polypropylene (PP)-maleic anhydride polypropylene copolymers (PP-MAPP) composites using micromechanical technique and nondestructive acoustic emission. Composites Science and Technology, **66**, 2686–2699 (2006).

[24] Pisanova E., Zhandarov S., Mader E., Ahmad I., Young R. J.: Three techniques of interfacial bond strength estimation from direct observation of crack initiation and propagation in polymer-fibre systems. Composites: Part A-Applied Science and Manufacturing, **32**, 435–443 (2001).

eXPRESS Polymer Letters Vol.1, No.5 (2007) 308–317
Available online at www.expresspolymlett.com
DOI: 10.3144/expresspolymlett.2007.44

Synthesis and characterization of electrical conducting chitosan-graft-polyaniline

A. Tiwari[1*], *V. Singh*[2]

[1]Division of Engineering Materials, National Physical Laboratory, Dr. K. S. Krishnan Marg, New Delhi, 110 012, India
2Department of Chemistry, University of Allahabad, Allahabad, 211 002, India

Received 4 March 2007; accepted in revised form 29 April 2007

Abstract. A mucopolysaccharide, chitosan was grafted with polyaniline through oxidative-radical copolymerization using ammonium persulfate in acidic medium. The grafting conditions were extensively studied by varying grafting parameters. All the findings have been discussed and proposed a plausible mechanism for the graft copolymerization. The representative chitosan-graft-polyaniline (Ch-g-PANI) was characterized using UV-vis, FTIR, TGA, X-ray diffraction and Scanning electron microscopy taking chitosan as reference. Ch-g-PANI exhibited electrical conductivity, which increases with the extent of grafting onto chitosan backbone. Its electrical conductivity is further influenced by pH and showed pH switching electrical conduction behavior when exposed to NN_3/HCl vapors. The application of conducting biomaterial such as Ch-g-PANI in the electronic devices especially for the fabrication of sensor devices would be attractive not only in terms of product cost and environmental safety but also from a materials science point of view.

Keywords: *biopolymers, biocomposites, material testing, thermal properties, industrial applications*

1. Introduction

Polyaniline (PANI) being most promising organic conducting polymer finds wide applications, such as in rechargeable batteries, corrosion protection of metals, gas-separation membranes, and molecular sensors [1–4]. It bears good environmental, thermal and chemical stability, electrical and optical properties, facile redox and pH-switching behavior [5]. It can be rapidly 'switched' with the addition of acids (protonation) and bases (deprotonation). The acid doped PANI yields conducting emeraldine salt, and is dedoped to form the insulator emeraldine base [6]. The electrical conductivity of PANI is enhanced by simple change of pH conditions. Recently, conducting polymers, such as PANI, have been considered for microelectronics applications. The combination of tunable chemical properties with the electronic properties of conducting polymer has also a tremendous impact on the development of new sensors. The use of conducting polymers in sensors has recently been reviewed [7]. However, PANI has limitations in solubility and mechanical properties [8]. In general, incorporation of PANI into flexible matrix could result in good processability with the electrical conductivity having the requisite properties like chemical stability toward dopants, thermal stability, and insolubility under readily accessible conditions [9, 10]. Chitosan has gained growing interest to prepare semi-interpenetrating chitosan/polyaniline [11–13], because of its excellent film-forming ability, good adhesion, biocompatibility, and high mechanical strength.

Chitosan is a high molecular weight polysaccharide [14] composed of $\beta(1\rightarrow4)$ linked 2-deoxy-2-amino-D-glucopyranose units and $\beta(1\rightarrow4)$ linked 2-deoxy-2-acetamido-D-glucopyranose units. Chi-

---

[*]Corresponding author, e-mail: ashunpl@gmail.com

tosan has found potential use in many areas, it is a brittle material and tends to absorb a quantity of moisture and to improve its toughness, solubility and rheological properties, graft copolymerization of a vinyl monomer onto chitosan chains is commonly employed for several applications.

Therefore, chitosan as a low cost, degradable, biocompatible, high molecular weight, branched biopolymer with unique physiochemical properties [15] (presence of –OH and $–NH_2$ groups offers self doping) is a good candidate to introduce functional groups in PANI, and enhance its selectivity for chemical sensors. In the present study, PANI was grafted on to chitosan in order to synthesize electrically conducting tailor-made material having good pH-switching properties. In the accomplished studies, the reaction mechanism, crystallinty, morphology, thermal and electrical properties were extensively investigated. It was expected that the results would be promising for biomaterial based sensors fabrication and it may be used either *in vivo* or *in vitro*.

2. Experimental section

2.1. Materials

Chitosan (Aldrich; M_w $1.86\cdot10^5$) and aniline (E. Merck) were used after purification. Ammonium persulfate (Aldrich) was used without further purification.

2.2. Synthesis of PANI

PANI was synthesized by oxidative polymerization [16] of doubly distilled aniline dissolved in aqueous HCl (1 M), using ammonium persulfate (APS) in aqueous HCl (1 M) as an oxidant at 4°C. Aniline (0.5 M) was dissolved in 200 ml of aqueous solution of HCl (1 M) and APS (0.54 M) was dissolved in 200 ml HCl (1 M). The oxidant solution was then added slowly to the aniline solution with continuous stirring at 4°C. The reaction mixture was kept under continuous stirring for two hours and then kept in a refrigerator overnight. The reaction mixture was filtered and washed with HCl (1 M) till the filtrate became colorless and then washed with doubly distilled water until the filtrate became acid free. The polymer was ground to a fine powder and low molecular weight oligomers were removed from polyaniline by acetone extraction. The resulting PANI was dried at 60°C in an air oven for 48 h and stored in a desiccator.

2.3. Synthesis of Ch-g-PANI

Chitosan-graft-polyaniline (Ch-g-PANI) was synthesized by a calculated amount of the chitosan dissolved in the minimum or required amount of acidic water in a 150 ml flask. To this solution, a calculated amount of the aniline and hydrochloric acid (HCl) was added and the total volume was made up to 25 ml the flask being thermostated at 25±0.2°C and the contents continuously stirred. After 30 minutes a definite amount of ammonium persulfate was added and this was taken as zero time. Grafting was allowed to proceed for 1 h. The reaction mixture was neutralized by 5% aqueous NaOH and the graft copolymer was precipitated with absolute ethanol. The resulting precipitate was washed with N-methyl pyrrolidinone (NMP) in order to separate PANI (homopolymer) from the copolymer. The material was ground to a fine powder and low molecular weight PANI oligomers were removed from Ch-g-PANI via acetone extraction (Figure 1). Finally, the products were dried for 4 days in a vacuum oven at 50°C.

The percentage and efficiency of grafting were calcalculated by the Equations (1) and (2) [17]:

$$\%\ \text{Grafting}\ [\%\text{G}] = \frac{W_1 - W_2}{W_0} \cdot 100 \qquad (1)$$

$$\%\ \text{Efficiency}\ [\%\text{E}] = \frac{W_1 - W_2}{W_2} \cdot 100 \qquad (2)$$

where W_1, W_0 and W_2 denote, respectively, the weights of Ch-g-PANI, chitosan and aniline monomer.

2.4. Electrical conductivity measurement

The surface DC electrical conductivity of the Ch-g-PANI rectangular pressed pallets (pressure 4 tons/cm^2) was measured by the four-probe method [18].

The resistivity can be calculated by Equation (3):

$$\rho = 2\,\pi\,S\left(\frac{V}{I}\right) \qquad (3)$$

where, S is the probe spacing [mm], which was kept constant, I is the supplied current in [mA], and the

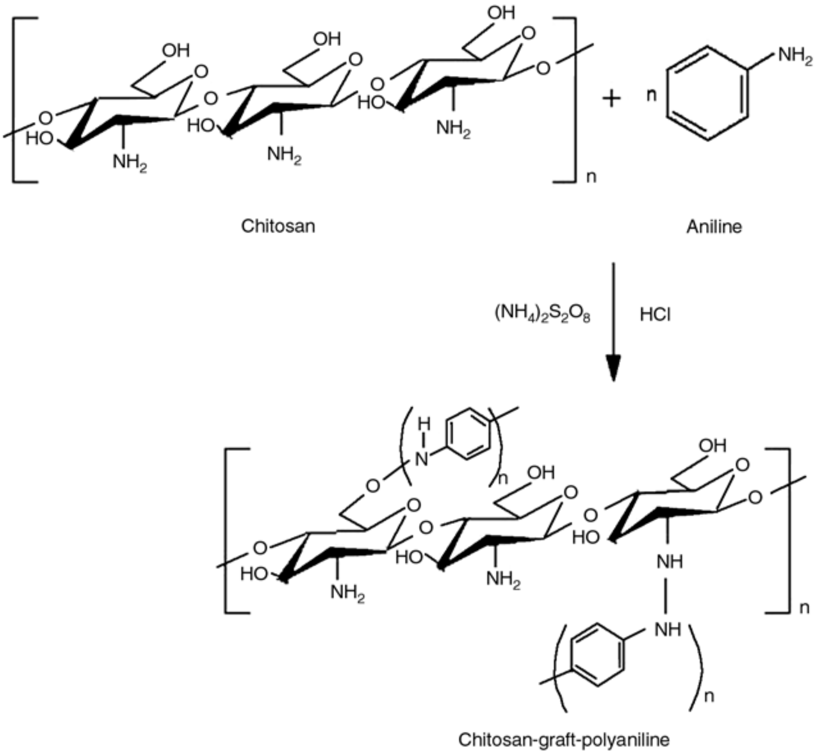

Figure 1. Chitosan-graft-polyaniline synthesized through the oxidative-radical graft copolymerization

corresponding voltage was measured in [mV]. Conductivity can be computed using the Equation (4):

$$\sigma = \frac{1}{\rho} \tag{4}$$

where σ and ρ are conductivity [S cm^{-1}] and resistivity [Ω cm] respectively. The electrical conductivity measurements were carried out at intervals of 20 min. The effect of pH on the electrical conductivity of Ch-g-PANI was studied. All the measurements were repeated three times at intervals of 20 min.

2.5. Characterization of chitosan-g-PANI

The UV-vis spectra were recorded on an Ocean Optics HR 4000 High Resolution Spectrophotometer, using aqueous solution of the samples. FTIR spectra were recorded on a Perkin-Elmer instrument (PK11310), using a pellet made with dehydrated KBr and instrument in the reflectance mode. X-ray diffractogram was taken by Rigaku Rotaflex, RAD/Max-B, Rigaku Corporation, Japan instrument with a scanning speed of 1° per minute. TGA was recorded on Rigaku Thermoflex, PTC-10A, Rigaku Corporation, Japan with 10°C per minute heating rate and Alumina as the reference material. Scanning electron microscope (SEM) was done on a JEOL-840, JEOL Corporation, Japan by making a film of desirable size and coated with gold. The DC electrical conductivity of the samples was measured by making rectangular pressed pallets (pressure 4 tons/cm^2) and using the Keithley four-probe system, having a 224 programmable current source, 181 nano voltameter and 195A digital multimeter.

3. Results and discussion

3.1. Determination of optimal grafting conditions

To optimize the condition for grafting of PANI on to the chitosan, ammonium persulfate/hydrochloric acid/aniline monomer/chitosan concentrations, reaction temperature and reaction time were varied and keeping total volume of the reaction mixture fixed at 25 ml. It was observed that $(NH_4)_2S_2O_8$/hydrochloric acid system can be efficiently used in the graft copolymerization of polyaniline on to chitosan, where maximum 91.40 %E could be achieved.

3.1.1. Effect of ammonium persulfate concentration

The %G increased with an increase in initiator/oxidant concentration, reaching a maximum value at

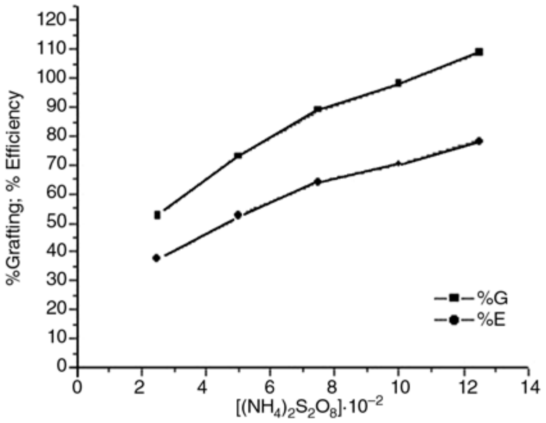

Figure 2. Effect of ammonium persulfate concentration at fixed concentration of [aniline] $1.5\cdot10^{-2}$, [HCl] 0.3 and [Ch] 1 g/l at 25±0.2°C for 1 h

$12.5\cdot10^{-2}$ M of ammonium persulfate (APS) at fixed concentrations of $1.5\cdot10^{-2}$ M aniline, 0.3 M hydrochloric acid and 1 g/l Chitosan (Ch) at 25±0.2°C for 1 h (Figure 2). It was observed that %G increased within the APS concentration range from $2.5\cdot10^{-2}$–$12.5\cdot10^{-2}$ M. It may be due to the fact that at this concentration range, the produced sulfate ion radical moieties activate the backbone of chitosan and simultaneously produced the PANI ion radical, which takes place immediately followed by the graft copolymerization of the monomer onto the chitosan backbone. Therefore, %E increased with an increase in the concentration of persulfate.

3.1.2. Effect of HCl concentration

The effect of acid was studied in the range 0.1–0.5 M at a fixed concentration of $12.5\cdot10^{-2}$ M ammonium persulfate, $1.5\cdot10^{-2}$ M aniline and 1 g/l chitosan at 25±0.2°C for 1 h (Figure 3). It was observed that both %G and %E increases with an increase in the acid concentration, which may be due to a higher degree of protonation of the aniline monomer and acceleration of the propagation of aniline, which can generate more PANI ion radicals.

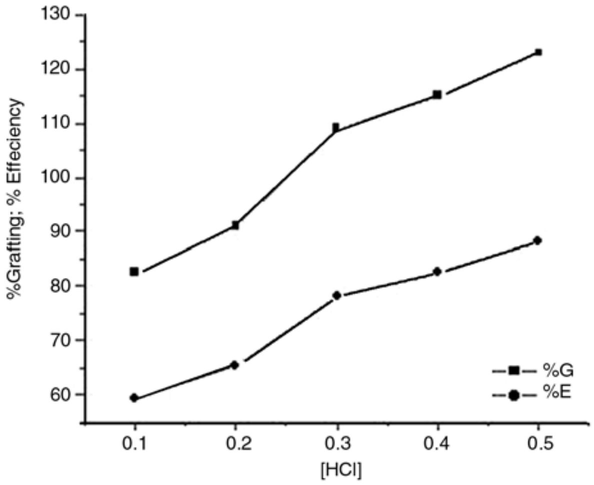

Figure 3. Effect of HCl concentration at fixed concentration of $[(NH_4)_2S_2O_8]$ $12.5\cdot10^{-2}$, [aniline] $1.5\cdot10^{-2}$ and [Ch] 1 g/l at 25±0·2°C for 1 h

3.1.3. Effect of aniline concentration

The increase in the concentration of monomer from $1\cdot10^{-2}$–$3\cdot10^{-2}$ M, resulted in the increase of %G and %E (up to $1.5\cdot10^{-2}$ M), under the fixed concentration of $12.5\cdot10^{-2}$ M persulfate, 0.5 M HCl and 1 g/l chitosan at 25±0.2°C for 1 h (Figure 4). The increase in %G and %E may be due to the formation of more PANI radical ions, while generating more grafting sites and availability of extra aniline monomer for grafting. With an increasing concentration beyond $1.5\cdot10^{-2}$ M the %E decreases slightly, which is probably due to formation of PANI homopolymer.

3.1.4. Effect of chitosan concentration

The effect of chitosan concentration was studied in the range of 1–5 g/l with the constant concentration of [persulfate] $12.5\cdot10^{-2}$, [HCl] 0.5, [aniline] $1.5\cdot10^{-2}$ at 25±0.2°C for 1 h (Figure 5). It was found that the %G and %E decreased with increasing the concentration of chitosan, which may be due to the increase in the viscosity of the reaction medium causing hindrance in the normal reaction.

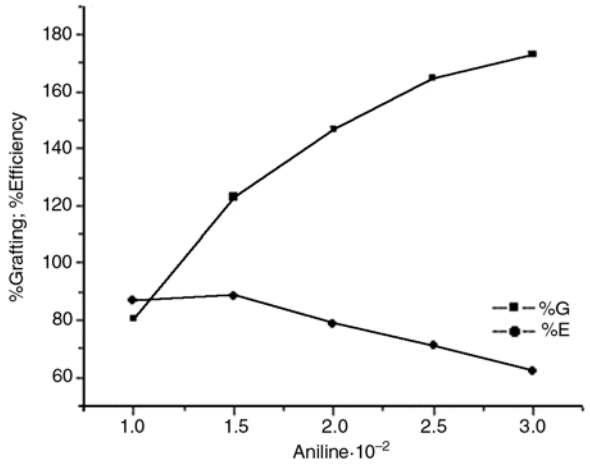

Figure 4. Effect of aniline concentration under the fixed concentration of $[(NH_4)_2S_2O)]$ $1.2\cdot10^{-2}$, [HCl] 0.5 and [Ch] 1 g/l at 25±0.2°C for 1 h

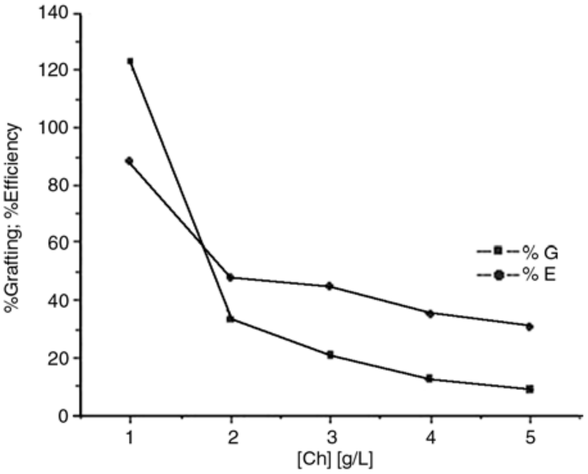

Figure 5. Effect of chitosan concentration with the constant concentration of [$(NH_4)_2S_2O_8$] $1.2\cdot10^{-2}$, [HCl] 0.5 and [aniline] $1.5\cdot10^{-2}$ at 25±0·2°C for 1 h

3.1.5. Effect of temperature

The grafting reaction was carried out at different temperatures (10–30°C), while keeping other variables constant; [persulfate] $12.5\cdot10^{-2}$, [HCl] 0.5, [aniline] $1.5\cdot10^{-2}$ and [Ch] 1.0 g/l for 2 h (Figure 6). Maximum %G was obtained at 25°C. The observed increase in %G may be attributed to the increase in the number of collisions between the monomer and the chitosan molecules that results in a decrease of the viscosity of the medium at higher temperature. Beyond 25°C, %G, the slight decrease may be due to an increase in ionic mobility of the PANI ion radical and formation of more homopolymer.

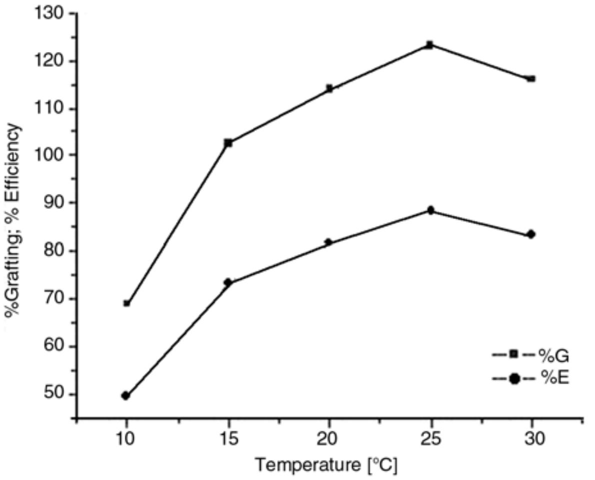

Figure 6. Effect of temperature keeping other variables constant; [$(NH_4)_2S)O)$] $1.2\cdot10^{-2}$, [HCl] 0.5, [aniline] $1.5\cdot10^{-2}$ and [Ch] 1 g/l for 1 h

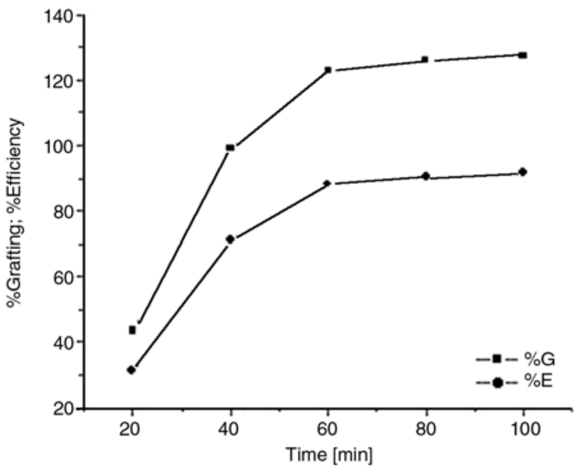

Figure 7. Effect of grafting time keeping other variables constant; [$(NH_4)_2S_2O_8$] $1.2\cdot10^{-2}$, [HCl] 0.5, [aniline] $1.5\cdot10^{-2}$ and [Ch] 1 g/l at 25±0.2°C

3.1.6. Effect of grafting time

The grafting reaction was carried out at different times (20–100 min) keeping other variables constant; [persulfate] $12.5\cdot10^{-2}$, [HCl] 0.5, [aniline] $1.5\cdot10^{-2}$ and [Ch] 1.0 g/l at 25±0.2°C (Figure 7). Maximum %G was obtained at 100 min. The %G increased rapidly with increase in time up to 100 min, after which it levels off. Finding could be attributed to a decrease in concentration for both initiator and monomer, thereby a reduction in the number of sites on the backbone accessible for grafting as the reaction procedure.

3.2. Mechanism for graft copolymerization

Other researchers [19–21] have exploited free radical copolymerization of vinyl monomers on to chitosan using persulfate. A chain mechanism [22] is involved due to formation of sulphate ion radicals ($SO_4^{-\cdot}$), which are well-known ion chain carriers for graft copolymerization. At the same time persulfate stimulates the oxidative polymerization reaction of aniline [23] via a medium of cationic radicals and form PANI and PANI radicals. Finally chitosan macro radicals and PANI cation radicals are combined to form Ch-g-PANI graft copolymer. Mechanism may be written as shown by Figure 8. $SO_4^{-\cdot}$ is the primary radicals, generated from the ammonium persulfate (APS) by the reduction of one electron, expressed as $R^{\cdot}$ in the Figure 8. Simultaneously, APS generates SO_4^{-2} ions by the reduction of two electrons and act as oxidant. They initiate the oxidative polymerization of aniline, as

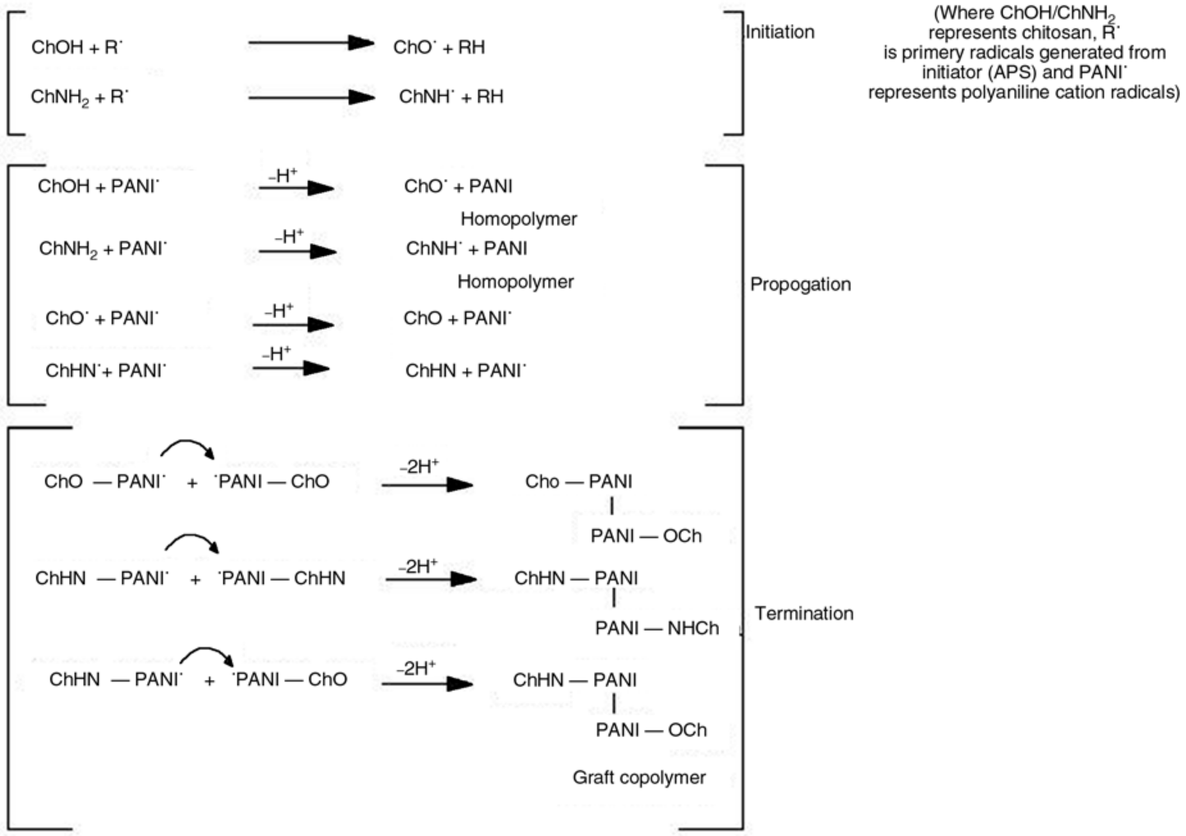

Figure 8. Graft copolymerization of polyaniline on to chitosan

the polymerization of monomer is reported to be faster than the H abstraction from the biopolymer backbone [24]. The macro radicals ChO$^{\cdot}$ and Ch-HN$^{\cdot}$ may be generated by the abstraction of H by the growing polyaniline ion radical (PANI$^{\cdot}$) in the medium of acid, which may add onto the ChO$^{\cdot}$ and Ch-HN$^{\cdot}$ macro radicals generating new radical ChO-PANI$^{\cdot}$ and Ch-NH-PANI$^{\cdot}$ and these chains will grow and combined with other ChO-PANI$^{\cdot}$ or Ch-NH-PANI$^{\cdot}$ chains to give a graft copolymer.

3.3. Characterization of the grafted chitosan

A representative Ch-g-PANI sample (173 %G) was characterized by UV-vis, FTIR, XRD, TGA and SEM analysis.

3.3.1. UV-vis spectra

The UV-vis spectra of Ch-g-PANI at pH 1 (Figure 9a) showed a broad absorption band at 300–350 nm due to overlapping of glucopyranose components of chitosan and π-π* transition of benzenoid rings of grafted PANI with bands at 430 nm (due to polaronic peak of grafted PANI) and at 800 nm (assigned bipolaronic transitions of grafted PANI), while Ch-g-PANI at pH 10 (Figure 9b) clearly showed the dedoping effect (emeraldine base form of grafted PANI) and peak suppressed at 430 nm but appeared a new peak at 620 nm (due to the π-π* transition of quinoid rings on the grafted PANI). These curves (Figure 9a and 9b) indicating that the grafted PANI showed transition 'emeraldine salt-emeraldine base' (protonation-deprotonation or doping-dedoping) and bears emeraldine oxidation state in the media of different pH, which

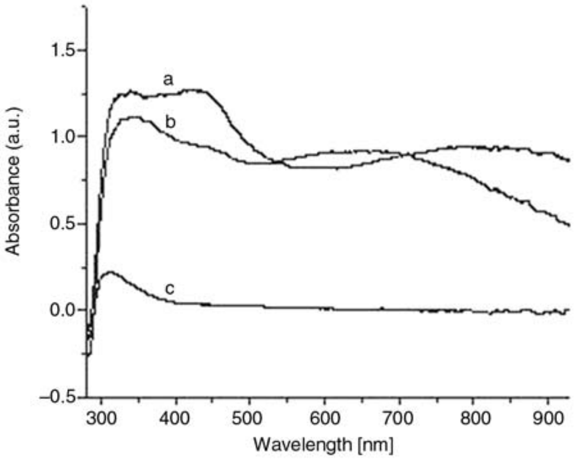

Figure 9. UV-vis spectra of (a) Ch-g-PANI at pH 1, (b) Ch-g-PANI at pH 10, (c) chitosan at pH 3

affects its electronic absorption spectra [23]. Chitosan showed (Figure 9c) a broad absorption band at 300 nm (due to glucopyranose components). Furthermore, the characteristic peaks of glucopyranose and PANI was significantly observed and it supports the grafting of PANI on to chitosan. Therefore, UV-vis spectra confirmed the chemical structure, conjugation, electronic transition and doping-dedoping behavior of Ch-g-PANI.

3.3.2. FTIR spectra

FTIR spectra of Ch-g-PANI (Figure 10) showed characteristic peaks of PANI as well as chitosan. The infrared band at 3040–3266 cm^{-1} corresponds to N–H stretching with hydrogen bonded 20 amino groups and free O–H stretching vibration, 3024 cm^{-1} corresponds to aromatic C–H stretching, 2930 and 2864 cm^{-1} (due to aliphatic C–H stretching), 1632 cm^{-1} (due to C=O stretching of carbonyl group, typical saccharide absorption), 1526 cm^{-1} (due to C=C stretching of quinoid rings), 1462 cm^{-1} (due to C=C stretching vibration of benzenoid rings), at 1284 cm^{-1} (due to C–N stretching). The absorption band at 1110 cm^{-1} was assigned to N=Q=N bending vibration shift towards the lower wave number correspond to the PANI. The shift of 1130 cm^{-1} band to lower wave number could be attributed to the hydrogen bonding between chitosan and imine group of the grafted chain of PANI. The absorption band at 1030 cm^{-1} (due to O–H bending), at 1076 cm^{-1} (characteristic peaks of a saccharide structure; C–O stretching) and at 830 cm^{-1} was assigned to aromatic C–H bending vibration band due to the 1, 4-disubstituted benzene ring, chitosan showed characteristic peaks of mucopolysaccharide [15]. Hence, FTIR studies clearly suggested the graft copolymerization of polyaniline on to chitosan.

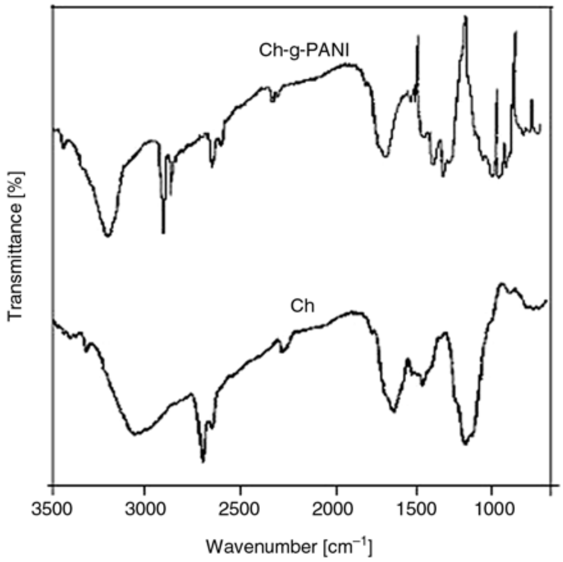

Figure 10. FTIR spectra of Ch-g-PANI and Ch

3.3.3. TGA

The thermal resistance of Ch-g-PANI was determined by thermogravimetric analysis (TGA) taking chitosan as reference. TGA indicates that the decomposition of the graft copolymer onsets at 176°C and 52% weight loss up to 700°C and the graft copolymer slowly degrades, while decomposition onsets of the chitosan was 145°C and showed weight loss of 61% up to 700°C. It indicates that Ch-g-PANI is more thermally stable than the chitosan (Figure 11).

3.3.4. XRD spectra

XRD of the Ch-g-PANI further supported the grafting (Figure 12). XRD spectra of the grafted chitosan showed a crystallinity area in the region of 2θ 18–24° due to the grafting of PANI onto the chitosan backbone, while XRD of the chitosan showed amorphous patterns.

3.3.5. SEM

The surface topography of the Ch-g-PANI was studied by scanning electron microscopy (SEM) taking chitosan as reference. The exterior surface of the Ch-g-PANI seems like globules that were accumulated in contrast to the interior structures and showed a porous surface. This fact can be attributed to the porosity of the globular surface in the grafted chitosan, while chitosan showed cotton like accumulation and bears an irregular shape with porous

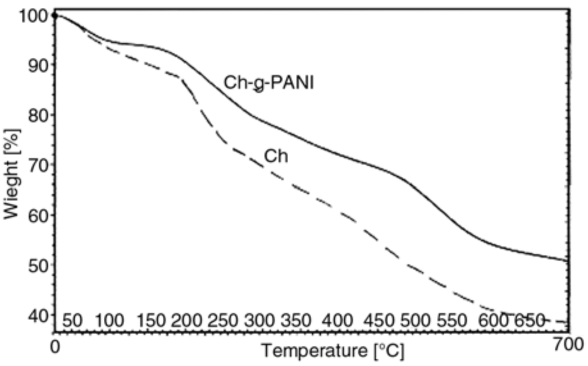

Figure 11. TGA analysis of Ch-g-PANI and Ch

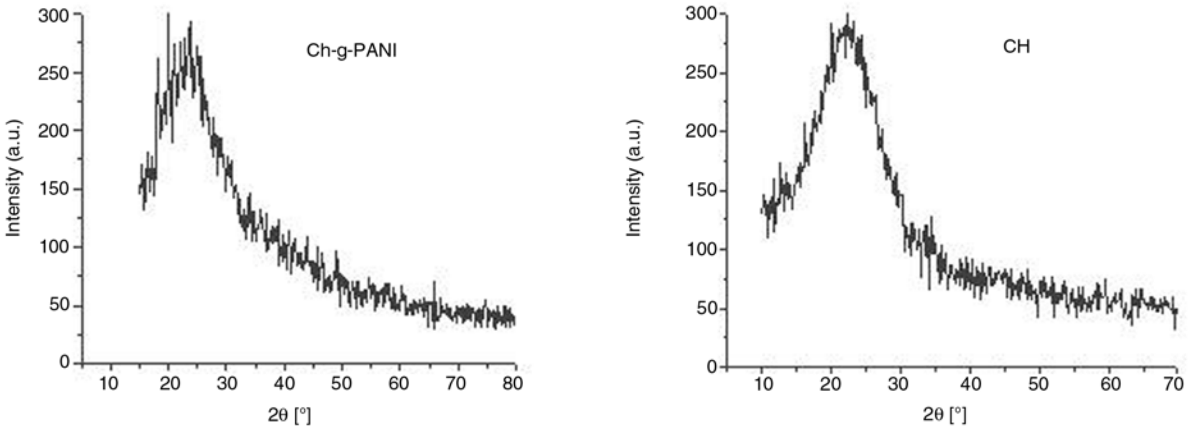

Figure 12. XRD spectra of Ch-g-PANI and Ch

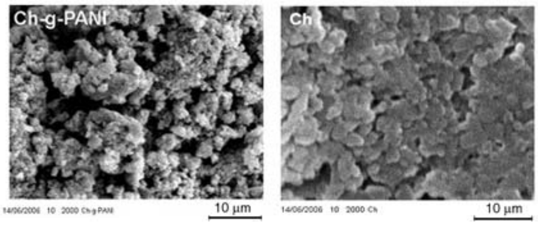

Figure 13. SEM pictures of Ch-g-PANI and Ch

surface. Hence, the surface evidence supports the homogeneity of the uniform grafting of PANI on to the chitosan (Figure 13).

3.4. Electrical conductivity measurement

The DC electrical conductivity of grafted (sample of optimum condition; 173 %G) was measured at laboratory condition with reference to PANI and chitosan. The results are summarized in the Table 1. The value of DC electrical conductivity was found almost 5000 times higher than that of the chitosan and is attributed to grafting of PANI on to chitosan backbone. The electrical conductivity was influenced with extent of grafting. The results are summarized in the Table 2. It has been clearly observed that increasing % grafting, electrical conductivity simultaneously increased. The finding was attributed to the electrical conduction in Ch-g-PANI material, which is purely electronic and occurred due to the grafting of PANI onto chitosan. The electrical conductivity pH switching behavior of the Ch-g-PANI was measured after doping and dedoping with different concentrations of HCl and NH_3 respectively at a fixed time. The conductivity of the grafted chitosan was increased with increasing dopant concentration (higher at pH 0 and very low at pH 10), indicating the formation of emeraldine salt to emeraldine base of the grafted PANI chain in the material [25, 26]. All the results are summarized in the Table 3. Therefore, grafted chitosan showed inter-conversion of emeraldine salt to emeraldine base like PANI and hence it could hold promise for sensor applications.

Table 1. Conductivity measurement of polyaniline, chitosan and chitosan-graft-polyaniline

Sl. No.	Polymer	%G	pH	Conductivity [S cm^{-1}]
1.	PANI	–	1	0.742
2.	Chitosan	–	7	$9.84\cdot10^{-6}$
3.	Ch-g-PANI	173	1	$4.03\cdot10^{-2}$

Table 2. Effect of %Grafting on electrical conductivity of chitosan-graft-polyaniline

Sl. No.	Polymer	%G	pH	Conductivity [S cm^{-1}]
1.	Ch-g-PANI	52.5	1	$6.74\cdot10^{-4}$
2.	Ch-g-PANI	91	1	$5.19\cdot10^{-3}$
3.	Ch-g-PANI	146.5	1	$0.96\cdot10^{-2}$
4.	Ch-g-PANI	173	1	$4.03\cdot10^{-2}$

Table 3. Effect of pH on electrical conductivity of chitosan-graft-polyaniline

Sl. No.	Polymer	%G	pH	Conductivity [S cm^{-1}]
1.	Ch-g-PANI	173	0	$9.63\cdot10^{-2}$
2.	Ch-g-PANI	173	1	$4.03\cdot10^{-2}$
3.	Ch-g-PANI	173	3	$4.91\cdot10^{-3}$
4.	Ch-g-PANI	173	7	$8.21\cdot10^{-4}$
5.	Ch-g-PANI	173	10	$0.53\cdot10^{-6}$

4. Conclusions

An inherently anisotropic graft copolymer was synthesized by grafting of polyaniline on to chitosan using persulfate as an initiator in acidic condition. The optimum grafting efficiency was find at $[(NH_4)_2S_2O_8]$ $12.5\cdot10^{-2}$, [aniline] $1.5\cdot10^{-2}$, [hydrochloric acid] 0.5, [chitosan] 1.0 g/l, temperature 25±0.2°C and reaction time 100 min. The grafted biomaterial exhibited electrical conductivity with pH switching behavior like PANI. The electrical conductivity depended on the extent of grafting and pH of the material. In conclusion, PANI grafted biopolymer will provide good processability with improved solubility, mechanical strength and controlled electrical properties. Therefore, Ch-g-PANI could be exploited for chemical and biosensor applications.

Acknowledgements

The authors are thankful to the Department of Science and Technology, Govt. of India for generous financial support and to the Director, National Physical Laboratory, New Delhi, India for providing infrastructure facilities to carry out this work.

References

[1] Sengupta P. P. S., Barik S., Adhikari B.: Polyaniline as a gas-sensor material. Materials and Manufacturing Processes, **21**, 263–270 (2006).

[2] Tan C. K., Blackwood D. J.: Interactions between polyaniline and methanol vapour. Sensors and Actuators B: Chemical, **71**, 184–191 (2000).

[3] Gosh M., Barman A., Meikap A. K., De S. K., Chatterjee S.: Hopping transport in HCl doped conducting polyaniline. Physics Letters: A, **260**, 138–148 (1999).

[4] Karami H., Mousavi M. F., Shamsipur M.: A new design for dry polyaniline rechargeable batteries. Journal of Power Sources, **117**, 255–259 (2003).

[5] Prokes J., Stejskal J.: Polyaniline prepared in the presence of various acids: 2. Thermal stability of conductivity. Polymer Degradation and Stability, **86**, 187–195 (2004).

[6] Kahol P. K., Kumar S. K. K., Geetha S., Trivedi D. C.: Effect of dopants on electron localization length in polyaniline. Synthetic Metals, **139**, 191–200 (2003).

[6] Kang Y., Kim S. K., Lee C.: Doping of polyaniline by thermal acid-base exchange reaction. Materials Science and Engineering: C, **24**, 39–41 (2004).

[7] Adhikari B., Majumdar S.: Polymers in sensor applications. Progress in Polymer Science, **29**, 699–766 (2004).

[8] Tiwari A.: Gum arabic-graft-polyaniline: An electrically active redox biomaterial for sensor applications. Journal of Macromolecular Science Part A: Pure and Applied Chemistry, **44**, 735–745 (2007).

[9] Lu X., Tan C. Y., Xu J., He C.: Thermal degradation of electrical conductivity of polyacrylic acid doped polyaniline: effect of molecular weight of the dopants. Synthetic Metals, **138**, 429–440 (2003).

[10] Takahashi K., Nakamura K., Yamaguchi T., Komura T., Ito S., Aizawa R., Murata K.: Characterization of water-soluble externally HCl-doped conducting polyaniline. Synthetic Metals, **128**, 27–33 (2002).

[11] Shin S. R., Park S. J., Yoon S. G., Spinks G. M., Kim S. I., Kim S. J.: Synthesis of conducting polyaniline in semi-IPN based on chitosan. Synthetic Metals, **154**, 213–216 (2005).

[12] Kim S. J., Shin S. R., Spinks G. M., Kim Y., Kim S. I.: Synthesis and characteristics of a semi-interpenetrating polymer network based on chitosan/polyaniline under different ph conditions. Journal of Applied Polymer Science, **96**, 867–873 (2005).

[13] Peniche C., Argüelles-Monal W., Davidenko N., Sastre R., Gallardo A., Roman S. J.: Self-curing membranes of chitosan/PAA IPNs obtained by radical polymerization: preparation, characterization and interpolymer complexation. Biomaterials, **20**, 1869–1878 (1999).

[14] Singh V., Tiwari A., Tripathi D. N., Sanghi R.: Microwave assisted synthesis of chitosan-graft-polyacrylamide: an efficient metal ion binder. Polymer, **47**, 254–260 (2006).

[15] Singh V., Tripathi D. N., Tiwari A., Sanghi R.: Microwave Promoted Synthesis of Chitosan-grafted-poly(acrylonitrile). Journal of Applied Polymer Science, **95**, 820–825 (2004).

[16] Albuquerque J. E., Mattoso L. H. C., Balogh D. T., Faria R. M., Masters J. G., MacDiarmid A. G.: A simple method to estimate the oxidation state of polyanilines. Synthetic Metals, **113**, 19–22 (2000).

[17] Singh V., Tiwari A., Tripathi D. N., Sanghi R.: Microwave assisted synthesis of Guar-g-poly(acrylamide). Carbohydrate Polymers, **58**, 1–6 (2004).

[18] Tiwari A., Mishra A. P., Dhakate S. R., Khan R., Shukla S. K.: Synthesis of electrically active biopolymer-SiO2 nanocomposite aerogel. Materials Letters, Doi: 10.1016/j.matlet.2007.02.076 (2007).

[19] Singh V., Tiwari A., Singh S. P., Shukla P. K., Sanghi R.: Co-polymerization of methylmethacrylate on to galactomannans using $K_2S_2O_8$/ascorbic acid redox system. Reactive and Functional Polymer, **66**, 1306–1318 (2006).

[20] Singh V., Tiwari A., Sanghi R.: Studies on $K_2S_2O_8$/ascorbic acid initiated synthesis of Ipomoea dasysperma seed gum-g-poly(acrylonitrile): A potential industrial gum. Journal of Applied Polymer Science, **98**, 1652–1662 (2005).

[21] Singh V., Tiwari A., Tripathi D. N., Sanghi R.: Poly(acrylonitrile) grafted ipomoea seed-gums: A renewable reservoir to industrial gums. Biomacromolecules, **6**, 453–456 (2005).

[22] Singh V., Tiwari A., Pandey S., Singh S. K.: Microwave promoted synthesis of starch-graft-poly(acrylonitrile). Express Polymer Letters, **1**, 51–58 (2007).

[23] Gospodinova N., Terlemezyan L.: Conducting polymers prepared by oxidative polymerization: Polyaniline. Progress in Polymer Science, **23**, 1443–1484 (1998).

[24] Singh V., Tiwari A., Tripathi D. N., Sanghi R.: Grafting of polyacrylonitrile on to guar gum under microwave irradiation. Journal of Applied Polymer Science, **92**, 1569–1575 (2004).

[25] Luthra V., Singh R., Gupta S. K., Mansingh A.: Mechanism of dc conduction in polyaniline doped with sulfuric acid. Current Applied Physics, **3**, 219–222 (2003).

[26] Matsuguchi M., Io J., Sugiyama G., Sakai Y.: Effect of NH_3 gas on the electrical conductivity of polyaniline blend films. Synthetic Metals, **128**, 15–19 (2002).

eXPRESS Polymer Letters Vol.1, No.5 (2007) 318–325
Available online at www.expresspolymlett.com
DOI: 10.3144/expresspolymlett.2007.45

The effect of fiber oxidation on the friction and wear behaviors of short-cut carbon fiber/polyimide composites

X. R. Zhang[1,2], *X .Q. Pei*[1,2], *Q. H. Wang*[1*]

[1]State Key Laboratory of Solid Lubrication, Lanzhou Institute of Chemical Physics, Chinese Academy of Sciences, Lanzhou 730000, China
[2]Graduate School, Chinese Academy of Sciences, Beijing 100039, China

Received 16 March 2007; accepted in revised form 29 April 2007

Abstract. Pitch-based short-cut carbon fibers were treated by HNO_3 oxidation, thereafter the treated (CFN) and untreated carbon fibers (CF) were incorporated into polyimide (PI) matrix to form composites. The carbon fibers before and after treatment were examined by Fourier Transform Infrared Spectroscopy (FTIR), X-ray photoelectron spectroscopy (XPS) and scanning electron microscope (SEM). The friction and wear behaviors of PI composites sliding against GCr15 steel rings were evaluated on an M-2000 model ring-on-block test rig, which revealed that small incorporation of carbon fibers can decrease the friction coefficient and improve the wear resistance of PI composites, and that the reinforcement effect of treated carbon fibers was better than that of the untreated ones. It was found that the optimum content of carbon fibers is 15 wt% when a thin and continuous transfer film was formed on the counterpart surface during the friction process. With further increasing content of carbon fibers, the friction coefficient increased and the wear resistance reduced owing to the drop out of carbon fibers from PI matrix. Besides, the friction coefficient of the PI composites decreased and the wear resistance improved with increasing load, while for the pure PI, its wear resistance decreased drastically owing to the micro-melting and mechanical deterioration caused by friction heat under a higher load.

Keywords: *polymer composites, reinforcement, carbon fiber, surface treatment, friction and wear*

---

1. Introduction

Carbon fiber reinforced polymer composites have been widely used in the fields of aerospace and high technical product. Carbon fibers present extremely high strength and modulus, good stiffness, and creep resistance etc., and have been widely employed as the reinforcing materials in the high performance polymer composites which have been extensively used in many industrial fields [1]. However, when applied without previous surface modification, the physical-chemical interaction between carbon fibers and its reinforced matrix is not tough enough due to the inert surface property of carbon fibers, which will directly affect the degree of interfacial adhesion in the composite system. Numerous methods concerning surface treatment, such as chemical method [2–4], electrochemical method [5–7], plasma treatment [8, 9], etc., have been developed to increase the quantity of surface functional groups and thus enhance the ability to establish strong interactions between fibers and matrix.

Polyimide (PI) possesses some extraordinary characteristics, such as excellent mechanical and electrical (insulating) properties, good thermal stability and chemical inertness, high wear resistance, and resistance against high energy radiation [10, 11]. The fiber-reinforced polyimide composites with high performance have especial applications in aerospace, robots, sports goods, etc. By reinforcing

---

[*]Corresponding author, e-mail: wangqh@lzb.ac.cn

PI with carbon fibers of high strength and modulus, excellent heat stability, and chemical inertness [12], it might be feasible to develop high performance PI-based composites. In the past years, many researchers have focused on the tribological behaviors of carbon fibers filled composites in various directions. Lu and Friedrich [13, 14] studied systematically the influence of carbon fibers volume content on the friction and wear behaviors of their composites, and declared that an optimum range for short carbon fibers in PEEK matrix is 15–25% (volume) according to the improved specific wear rate.

The objective of this work is to study the friction and wear behaviors of the modified short-cut carbon fibers reinforced polyimide composites. The surface properties of the carbon fibers before and after treatment were compared by FTIR, SEM, XPS. This work is believed to be helpful for the understanding of the effect of HNO_3 oxidation.

2. Experimental

2.1. Materials

PI(YS-20) powders (<38 μm) were commercially obtained from Shanghai Synthetic Resin Institute (Shanghai, China). The short-cut carbon fiber was about 100 μm in length and 7.8 μm in diameter, and the density was about 1.8 g/cm^3. HNO_3 solution (AR, with the weight concentration of 65–68%).

2.2. Preparation of PI composites

The commercial short-cut carbon fibers were dipped in acetone for 24 h, then cleaned ultrasonically with acetone for 0.5 h. Finally, they were dried at 100°C for 5 h before used. The oxidation of carbon fibers was achieved by heating carbon fibers in nitric acid (with the weight concentration of 65–68%) at 90°C for 1.5 h. After the surface oxidation, the modified fibers were thoroughly washed with distilled water, and dried before used. Such modified fibers were named as CFN.

In order to investigate the possible change of chemical composition of the carbon fibers treated by HNO_3 oxidation, Fourier Transform Infrared Spectroscopy (FTIR) measurements in the mid infrared (4000–400 cm^{-1}) were performed, which were recorded on a Bruker IFS/66v spectrometer. The specimens for FTIR measurements were prepared by KBr tabletting method. X-ray photoelectron spectroscopy (XPS) was used to detect functionalities on activated carbon fibers surfaces. The XPS measurement was performed using VG Scientific ESCA LAB 210 spectrometer, the base pressure in the sample chamber was about 10^{-7} Pa. The morphologies of the untreated carbon fibers (CF) and HNO_3 treated carbon fibers (CFN) were compared by SEM observation, before which the tested carbon fibers specimens were plated with gold coating to render them electrically conductive.

The CF and CFN were mixed with PI powders at selected mass fractions to prepare mixtures for the preparation of PI composites. To prepare the PI composites blocks, the mixtures were compressed and heated to 380°C in a mould. The pressure was held at 40 MPa for 75 min to allow full compression sintering. At the end of each run of compression sintering, the resulting specimens were cooled with the stove in air, cut into pre-set sizes for friction and wear tests.

2.3. Friction and wear test

The friction and wear behaviors of PI composites sliding against stainless steel were evaluated on an M-2000 model ring-on-block test rig (made by Jinan Testing Machine Factory, China).The contact schematic diagram is shown in Figure 1, the blocks in a size of 30 mm×7 mm×6 mm were made of the PI composites, the rings of ø40 mm×16 mm were made of GCr15 stainless steel, the chemical composition of the GCr15 bearing steel (mass fraction, %) is shown in Table 1. The tests were carried out

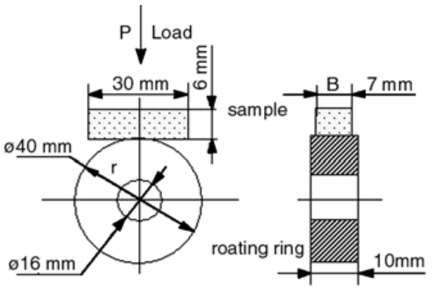

Figure1. The contact schematic diagram for the friction couple

Table 1. Chemical composition of the GCr15 steel ring

Chemical composition (mass fraction, %)					
C	Mn	Si	P	S	Cr
0.95–1.05	0.25–0.45	0.15–0.35	≤ 0.025	≤ 0.025	1.40–1.65

at a linear velocity of 0.431 m/s in a period of 120 min with the loads ranging from 200 N to 500 N. Before each test, the stainless steel ring and the PI composite block were polished to a roughness (R_a) of about 0.2–0.3µm. The block specimen was static and the GCr15 bearing was sliding against the block unidirectionally. The friction force was measured using a torque shaft equipped with strain gauges mounted on a vertical arm that carried the block, which was used to calculate the friction coefficient by taking into account the normal load applied. The width of the wear tracks was measured with a reading microscope to an accuracy of 0.01 mm. Then the specific wear rate (ω) of the specimen was calculated from Equation (1).

$$\omega = \frac{B}{L \cdot P}\left[\frac{\pi r^2}{180}\arcsin\left(\frac{b}{2r}\right) - \frac{b}{2r}\sqrt{r^2 - \frac{b^2}{2}}\right] \quad \left[\frac{\mathrm{mm}^3}{\mathrm{N \cdot m}}\right] \tag{1}$$

where B is the width of the specimen [mm], r is the semi diameter of the stainless steel ring [mm], and b is the width of the wear trace [mm], L is the sliding distance in meter, P is the load in Newton. The tests were repeated three times, the wear tracks of the composite and stainless steel specimens were examined on a JSM-5600LV scanning electron microscope (SEM). In order to increase the resolution for the SEM observation, the tested composite specimens were plated with gold coating to render them electrically conductive.

3. Results and discussion

3.1. FTIR analysis of CF and CFN

It can be seen from Figure 2 that there were many active groups on the surface of CFN. The peak in the 1100–1220 cm^{-1} region is associated with ether type structures (C–O–C). The peak in the 1350–1390 cm^{-1} region reveals the existence of C–N bands. The peak in the 1500–1680 cm^{-1} region is assigned to aromatic C=C bands and various substitution modes of the aromatic ring. The peak in the 1710 cm^{-1} region reveals evidence of carbonyl groups on the CFN surface. So it can be concluded that the structure of carbon fiber had changed and more polar components were formed.

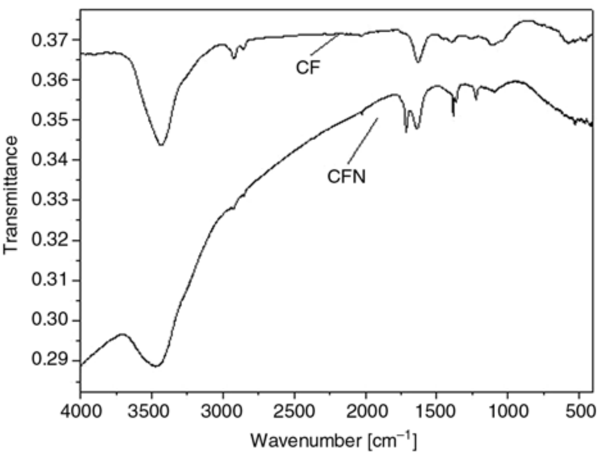

Figure 2. FTIR spectra of CF and CFN

3.2. XPS analysis of CF and CFN

The C1s XPS spectra of CF and CFN are shown in Figure 3. The dominant peak at 284.8 eV was assigned to graphitic carbon in the fiber [15]. The peak at 286.2 eV was assigned to the carbon in –C–O– structures. The binding energy of carbon in carbonyl groups is 287.5–288.1 eV.

It can be found from Table 2 that the surface C element concentration of the untreated, nitric acid treated carbon fiber samples were 80.2%, 67.4% respectively. A lower C concentration was found on the surfaces of the treated carbon fiber samples compared with that of the untreated ones. The surface O concentration of the untreated, nitric acid treated carbon fiber samples were 17.7%, 28.3 %, respectively. The O/C ratio on the surfaces of the treated carbon fiber samples increased compared with the untreated ones.

After HNO_3 oxidation, there were more active groups (–O–C– –C=O –O–C=O) on the surfaces of the carbon fibers, which increased total surface energy and their polarity and thus enhanced the

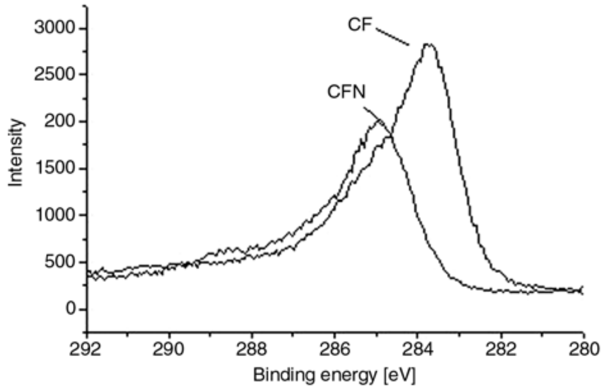

Figure 3. XPS spectra for C1s states on the CF and CFN

Table 2. XPS surface element analysis data of CF and CFN

Carbon fibers	C [%]	N [%]	O [%]	O/C
Untreated	80.2	2.1	17.7	0.22
Nitric acid treated	67.4	4.3	28.3	0.42

wettability of the carbon fibers with the PI matrix. Better wetting can improve the adhesive bond strength by increasing the thermodynamic work of adhesion or by reducing the number of interfacial defects [16]. Adhesion between the carbon fibers and PI matrix improved, which played an important role on the tribological properties of carbon fibers reinforced polymer composites.

3.3. Morphology analysis of CF and CFN

The morphologies of CF and CFN are shown in Figure 4. It can be seen that the surface of the carbon fiber after HNO_3 oxidation treatment (Figure 4b) was rougher than that of the untreated one (Figure 4a). There appeared more defects, closely spaced grooves, protuberances and dongas on the surfaces of CFN, which can increase surface roughness of carbon fibers. This would provide more contacts between the carbon fibers and PI matrix to ensure a significant level of van der Waals force, which enhanced the degree of mechanical interlocking between the fibers and the PI matrix [17].

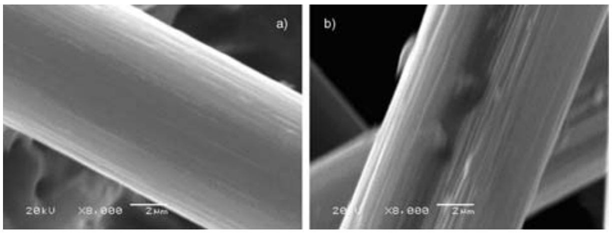

Figure 4. SEM morphologies of the CF (a) and CFN (b)

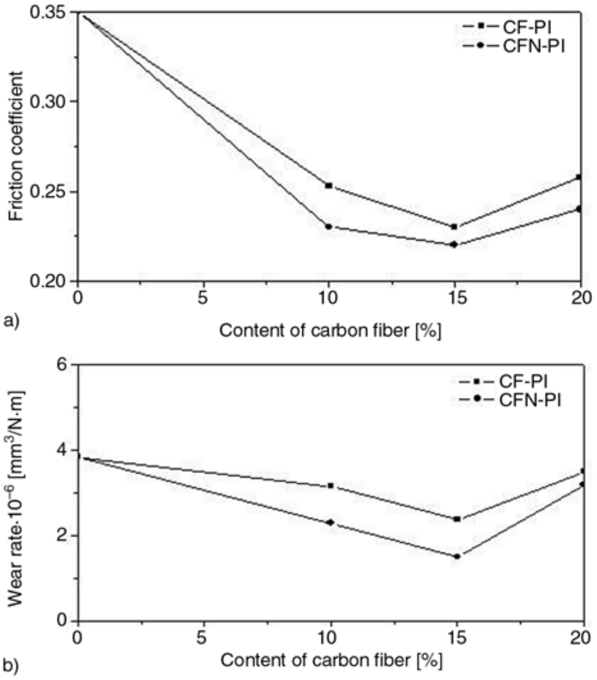

Figure 5. Variation of the friction coefficient and wear rate of the PI composites. a) friction coefficient vs. mass content of carbon fiber, b) wear rate *vs.* mass content of carbon fiber

3.4. The friction and wear properties

3.4.1. The influence of content of carbon fibers on the friction and wear properties of the PI composites

Figure 5 shows the friction coefficient and specific wear rate of four PI composites at a sliding speed of 0.431 m/s under 200 N. It was found that the small incorporation of carbon fibers can decrease the friction coefficient and improve the wear resistance of PI composites. Meanwhile, the results revealed that the reinforcement effect of the treated carbon fibers was better than that of the untreated ones. The optimum content of carbon fibers is 15 wt% when a thin and continuous transfer film was formed on the counterpart surface during the friction process. It was also found that the friction coefficient of the CFN-PI composites decreased slightly than that of the CF-PI composites, though the wear resistance improved drastically.

With increase in content, it also can be found that the friction coefficient increased slightly and the wear resistance reduced. With a high content of carbon fibers, there appeared more PI debris and broken carbon fibers fragments on the worn surface (this was supported by SEM as discussed in the subsequent section) owing to the drop out of carbon fibers from PI matrix during the friction process, which revealed that the adhesion between the carbon fibers and PI matrix decreased and there appeared more defects. This shifted the wear mechanisms from adhesive wear to abrasive wear, which reduced the wear resistance drastically and made the friction coefficient to have an increasing trend. However, the high fraction of carbon fibers made the composites stiffer, the ability of resistance against cracking improved, which made the friction coefficient decrease. So the friction coefficient of the composites increased slightly.

3.4.2. The influence of load on the friction and wear properties of the CFN-PI composites

Figure 6 shows the influence of load on the friction coefficient and specific wear rate of the CFN-PI composites. It can be seen that the friction coefficient of the pure PI decreased slightly with increasing load when the load was below 300 N. At the same time, the specific wear rates of the pure PI increased slowly. When the load beyond this range, the friction coefficient decreased drastically and the specific wear rate increased greatly owing to the micro-melting and mechanical deterioration caused by friction heat under a higher load. High temperature during friction process can cause an increase in the real contact areas and a decrease in mechanical strength of the PI composites, now, the latter takes a dominant place. As for the modified carbon fibers reinforced PI composites, both the friction coefficient and the specific wear rates of the CFN-PI composites decreased because the transfer film can form easier owing to a gradual increase of the real contact areas and the increase in adhesive force between the film and counterpart.

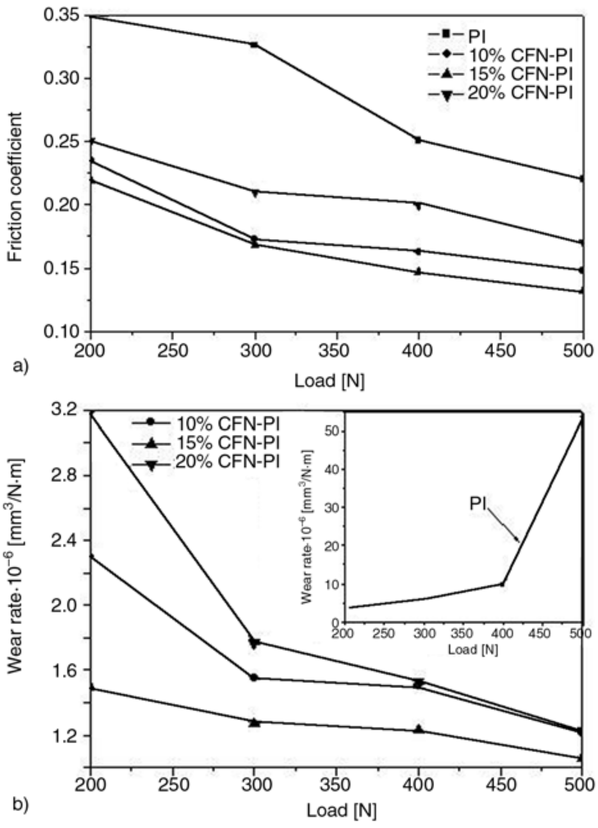

Figure 6. Variation of the friction coefficient and the wear rate of the CFN-PI composites under different load. a) Friction coefficient vs. load, b) wear rate *vs.* load

3.4.3. The influence of sliding time on the friction and wear properties of the CFN-PI composites

It can be seen from Figure 7 that the frictional process is composed of two distinct stages: the one is the running-in period and the other is the steady-state period. The friction coefficient of the running-in period was obviously higher than that of the steady-state period. It took less than 15 min to transit from the running-in period to the steady-state period. Because of the ability of self-lubricating of carbon fibers, the PI matrix transferred to the counterpart surface easier and the transfer film can form easier. After the formation and the peeling-off of the transfer film came to a balance, the friction coefficient became stable [10]. Moreover, it can be found that the time of running-in period of pure PI was obviously longer than that of the carbon fibers reinforced PI composites and the friction curve was more fluctuant, which corresponded to its poorer wear resistance under a higher load.

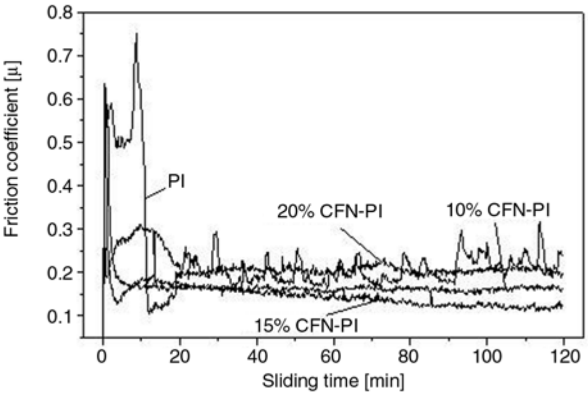

Figure 7. Typical friction coefficient variation of the CFN-PI composites with the sliding time (0.431 m/s and 400 N)

3.5. SEM analysis of the worn surfaces and the transfer films on the surface of GCr15 steel rings

Figure 8 shows the SEM morphologies of the worn surfaces of the PI composites sliding against the GCr15 steel at a sliding speed of 0.431 m/s under 200 N. The worn surface of the pure PI was characterized by severe plastic deformation and micro-cracking (Figure 8a), while a large amount of transferred PI debris were observed on the stainless steel counterpart surface and the transfer film was thick and discontinuous (Figure 9a), which correspond to its high friction coefficient of the pure PI.

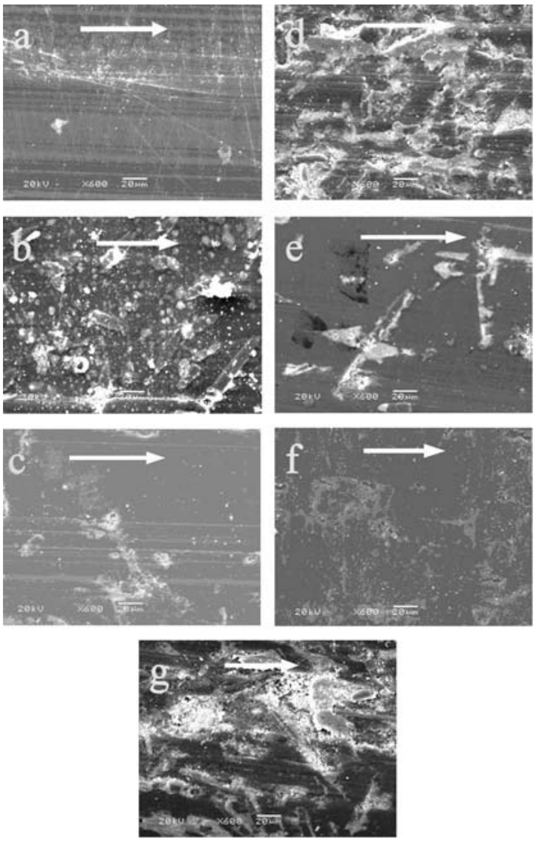

Figure 8. SEM morphologies of the worn surface of PI composites (600×); a) pure PI, b) 10% CF-PI, c) 15% CF-PI, d) 20% CF-PI, e)10% CFN-PI, f) 15% CFN-PI, g) 20% CFN-PI (L = 200 N, V = 0.431 m/s) (arrow indicates the sliding direction)

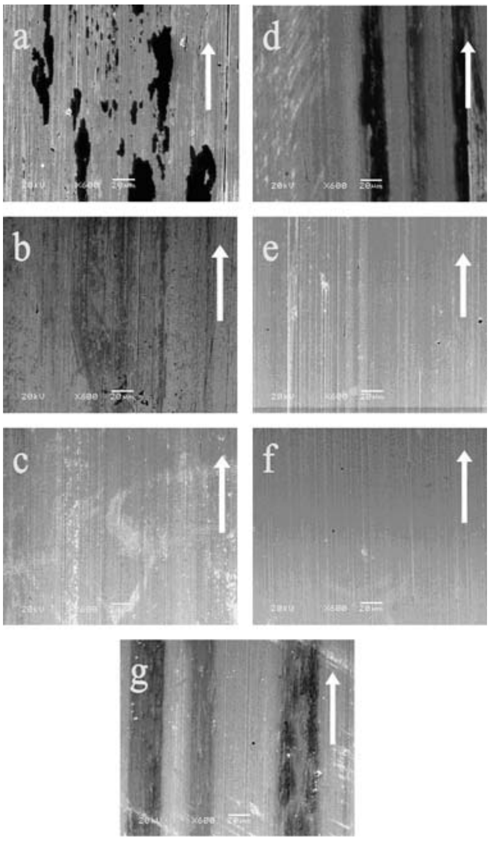

Figure 9. SEM morphologies of the transfer films on the surface of GCr15 steel counterpart (600×). a) pure PI, b) 10% CF-PI, c) 15% CF-PI, d) 20% CF-PI, e) 10% CFN-PI, f) 15% CFN-PI, g) 20% CFN-PI (arrow indicates the sliding direction)

In contrast, the 10 wt% CF-PI composite was characterized by slight scuffing and spalling and there was no obvious plastic deformation (Figure 8b) and the transfer film was thick and discontinuous (Figure 9b). The scuffing and spalling phenomena on the worn surface was significantly abated when the content of carbon fibers was 15 wt% (Figure 8c), meanwhile, the transfer film became thinner and uniform (Figure 9c). However, the worn surface of the PI composite with 20 wt% carbon fibers (Figure 8d) was characterized by many pulling-out and exposures of the carbon fibers and there were more wear debris and carbon fiber fragments, which indicated the poor adhesion between the carbon fibers and PI matrix. The drop out of the carbon fibers from PI matrix shifted the wear mechanisms from adhesive wear to abrasive wear. Meanwhile, the transfer film (Figure 9d) appeared to be thick, rough and discontinuous on the GCr15 steel counterpart surface.

It can be seen that the worn surface of the10 wt% CFN-PI composites (Figure 8e) was characterized by a few cracks and fibers fragments and the transfer film (Figure 9e) was thick and continuous. There was no PI debris and fibers fragments on the worn surface of the15 wt% CFN-PI composites (Figure 8f) and the transfer film (Figure 9f) is thinnest and continuous. It also can be seen that there were many exposures and wear debris on the worn surface of 20 wt% CFN-PI composites (Figure 8g) and the transfer film (Figure 9g) was thicker and discontinuous on the GCr15 steel counterpart surface. It can be concluded that the worn surfaces of the CFN-PI composites and the counterparts surfaces were smoother than the CF-PI composites with the same carbon fibers content and the PI matrix combined the carbon fiber better, the transfer film of 15 wt% CFN-PI composites (Figure 9f) appeared to be thinner, smoother and much more continuous, which conformed to the smaller friction coefficient and better wear resistance of the CFN-PI composites than CF-PI composites.

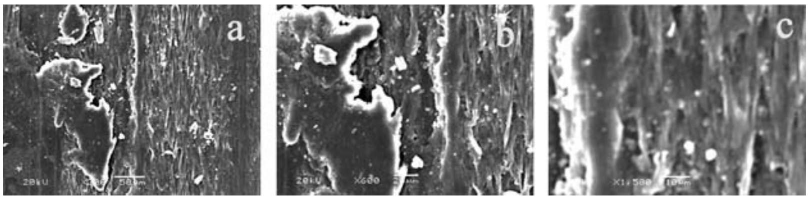

Figure 10. SEM morphologies of the worn surface of pure PI sliding under the load of 500 N and the velocity of 0.431 m/s; a) 300×, b) 600×, c) 1500×

It can be seen from Figure 10 that the pure PI might experience melting and many peeling-off on the worn surface under a higher load. The friction may produce a great deal of heat and cause the temperature between the worn surface and the counterpart increased drastically under a higher load. At a higher temperature, the pure PI molecular relaxation changed and more chains were mobile and transited from the glassy state (with high strength, high stiffness) into the rubbery state (with lower strength and lower stiffness) and easier transferred to the counterpart surface , thus a smoother worn surface and high wear rate of pure PI were observed.

4. Conclusions

(1) The incorporation of the treated and untreated carbon fibers contributed to the different change of tribological behaviors of PI composites. In the tested system regarding the friction and wear the optimum content of carbon fibers was about 15 wt%.

(2) The reinforcement of HNO_3 treated carbon fibers was better than that of the untreated ones. After treated by HNO_3, active groups or active sites for van der Waals and hydrogen bonding on the surfaces of carbon fibers increased, which can improve the interfacial adhesion between the fibers and the surrounding PI matrix and had a dominant effect on the friction and wear behaviors of polyimide composites.

(3) With increasing load, both the friction coefficient and the specific wear rates of the CFN-PI composites decreased. As for the pure PI, the friction coefficient decreased greatly, while the specific wear rate increased drastically owing to the micro-melting and mechanical deterioration caused by friction heat under a higher load.

Acknowledgements

The authors would like to acknowledge the financial support of the Innovative Group Foundation from NSFC (Grant No. 50421502) and the National Natural Science Foundation of China (Grant No.50475128).

References

[1] Donnet J. B., Bansal R. C.: Carbon Fibers, Dekker, New York (1990).

[2] Ogawa H., Satio.: Oxidation behavior of polyacrylonitrile fibers evaluated by new stabilization index. Carbon, **33**, 783–788 (1995).

[3] Wu Z. H., Pittman C. U., Gardner S. D.: Nitric acid oxidation of carbon fibers and the effects of subsequent treatment in refluxing aqueous NaOH. Carbon, **33**, 597–605 (1995).

[4] Toyoda M., Katoh H., Inagaki M.: Intercalation of nitric acid into carbon fibers. Carbon, **39**, 2231–2237 (2001).

[5] Basova Y. V., Hatori H., Yamada Y., Miyashita K.: Effect of oxidation-reduction surface treatment on the electrochemical behavior of PAN-based carbon fibers. Electrochemistry Communications, **1**, 540–544 (1999).

[6] Theodoridou E., Jannakoudakis A. D., Jannakoudakis P. D., Andonoglou P., Besenhard J. O.: Electrochemical oxidation of PAN- and pitch-based carbon fibers and deposition of palladium on the obtained materials. Synthetic Metals, **87**, 225–229 (1997).

[7] Yue Z. R., Jiang W., Wang L., Gardner S. D., Pittman C. U.: Surface characterization of electrochemically oxidized carbon fibers. Carbon, **37**, 1785–1796 (1999).

[8] Pittman C. U., Jiang W., Yue Z. R., Gardner S., Wang L., Toghiani H., Leon C. A.: Surface properties of electrochemically oxidized carbon fibers. Carbon, **37**, 1797–1805 (1999).

[9] Wu G. M.: Oxygen plasma treatment of high performance fibers for composites. Materials Chemistry and Physics, **85**, 81–87 (2004).

[10] Bahadur S., Polineni V. K.: Tribological studies of glass fabric-reinforced polyamide composites filled with CuO and PTFE. Wear, **200**, 95–104 (1996).

[11] Price D M.: Vapor Pressure Determination by Thermogravimetry. Thermochimica Acta, **367–368**, 253–262, (2001).

[12] Yudin V. E., Goykhman M. Y., Balik K., Glogar P., Gubanova G. N., Kudriavtsev V. V.: Carbonization behaviour of some polyimide resins reinforced with carbon fibers. Carbon, **38**, 5–12 (2000).

[13] Lu Z. P., Friedrich K.: On sliding friction and wear of PEEK and its composites. Wear, **181–183**, 624–631(1995).

[14] Friedrich K., Karger-Kocsis K., Lu Z. P.: Effects of steel counterface roughness and temperature on the friction and wear of PE(E)K composites under dry sliding conditions. Wear, **148**, 235–247 (1991).

[15] Li J. Q., Huang Y. D., Xu Z. W., Wang Z.: High-energy radiation technique treat on the surface of carbon fiber. Materials Chemistry and Physics, **94**, 315–321 (2005).

[16] Wu S.: Polymer interface and adhesion. Marcel Dekker, New York (1982).

[17] Jang B. Z.: Control of interfacial adhesion in continuous carbon and kevlar fiber reinforced polymer composites. Composites Science and Technology, **44**, 333–349 (1992).

eXPRESS Polymer Letters Vol.1, No.5 (2007) 326–332
Available online at www.expresspolymlett.com
DOI: 10.3144/expresspolymlett.2007.46

Improvement of thermal properties and flame retardancy of epoxy-amine thermosets by introducing bisphenol containing azomethine moiety

X. H. Zhang[1]*, *L. H. Huang*[2], *S. Chen*[3], *G. R. Qi*[1]

[1]Department of Polymer Science and Engineering, Zhejiang University, Hangzhou, 310027, P. R. China
[2]Department of Applied Biology, Shenzhen Senior Technical Institute, 518048, P. R. China
[3]College of Chemistry and Chemical Engineering, Jishou University, Jishou, 416000, P. R. China

Received 18 March 2007; accepted in revised form 2 May 2007

Abstract. A novel bisphenol 1, 4'-bis{4-[(4-hydroxy) phenyliminomethylidene] phenoxy} benzene (BHPB), which contains azomethine moiety and flexible aromatic ether linkage, was synthesized and introduced into the curing system composed of diglycidyl ether of bisphenol A (DGEBA) and diamine. The curing behavior of DGEBA/diamine changed dramatically due to the introduction of BHPB. The resultant epoxy thermosets containing BHPB had high T_gs (127–160°C), high $T_{d,5\%}$ (≥ 330°C) and high integral procedure decomposition temperature (IPDT) values (662–1230°C) and good flame retardancy because of their high Limiting Oxygen Index (*LOI*) values (above 29.5).

Keywords: *thermosetting resins, thermal stability, flame retardancy, epoxy, bisphenol*

1. Introduction

Diglycidyl ether of biphenyl A (DGEBA) is widely used for its versatile properties and low cost. However, it is thermally unstable and flammable when used in insulation materials. Introducing phosphorus element [1, 2], which is more environmental friendly than halogens, into the main chain of DGEBA via chain extension reaction is a good way to improve the flame retardancy of the resultant thermoset. But the higher the phosphorus content, the lower the thermal stability [2–4]. Nitrogen-containing epoxy thermosets are gradually attracting more attention because they exhibit good flame retardancy, thermal properties, as well as more environmental friendly.

It is well known that bisphenols containing azomethine group (Ar–CH=N–Ar), which is a rigid structure, frequently used as the mesogenic unit for liquid-crystalline epoxy themosets (LCTs) [5–7], can strengthen the thermal stability and increase the char residue when the thermosets containing of them decompose. However, the yield of azomethine-containing epoxy monomers from bisphenols is very low [7], which limited their applications. Furthermore, rigid azomethine moiety may result in brittleness of the resultant thermosets if no flexible structures were introduced. Herein, we synthesized a bisphenol, 1, 4'-bis{4-[(4-hydroxy) phenyliminomethylidene] phenoxy} benzene (BHPB), which contains both the azomethine moiety and flexible aromatic ether linkage, and introduced it directly into the backbone of epoxy-amine thermosets as a 'modifier' to improve the thermal stability and flame retardancy.

---

*Corresponding author, e-mail: xhzhang@zju.edu.cn

2. Materials and methods

Hydroquinone, *p*-chloronitrobenzene, 4-hydroxybenzaldehyde, hydrazine hydrate (85 wt% water solution), potassium carbonate and Iron (III) chloride ($FeCl_3{\cdot}6H_2O$) and $ZnCl_2$ were purchased from Sinopharm Chemical Reagent Co., Ltd. (Shanghai, China) and used without purification. Ethanol, dimethylformamide (DMF) were purchased from Hangzhou Shuanglin Chemical Reagent Co., Ltd. (Hangzhou, China), ethanol was used as received, and DMF was purified by distillation under reduced pressure over calcium hydride before use. Diglycidyl ether of biphenyl A (DGEBA, NPEL-127E) was granted kindly from Nan Ya plastics of China with an equivalent epoxy molecular weight of 180 g/eq.

Infrared spectra were recorded by using a Vector 22 FTIR spectrophotometer (400–4000 cm^{-1}, KBr pellet). ^1H NMR and ^{13}C NMR were obtained with an Avance DMX500 NMR spectrometer (Bruker, Darmstadt, Germany) at 35°C using d_6-DMSO as a solvent. Elemental analysis was performed on a Flash EA1112 CHN–O–Rapid elemental analyzer using acetanilide as a standard. Curing behavior of BAPB/BHPB/DGEBA system was carried out on a Perkin-Elmer DSC 7 thermal analyzer at a heating rate of 10°C/min at a flow rate of 40 ml/min under N_2. The temperature calculation was regularly made using In and Zn standards at each scanning rate being used. T_g determination was carried out in DSC at a heating rate of 20°C/min under N_2. Thermogravimetric analyses (TGA) were carried out on a Perkin-Elmer Pyris 1 at a heating rate of 10°C/min from 50°C to 850°C under N_2 atmosphere. *LOI* values were measured on a HC-2 *LOI* tester according to ASTM D-2863-77. The percentage in the O_2–N_2 mixture deemed sufficient to sustain the flame was taken as the *LOI*.

3. Experimental

3.1. Synthesis

The synthesis of 1, 4'-bis{4-[(4-hydroxy) phenyliminomethylidene] phenoxy} benzene (BHPB) is shown in Figure 1.

1, 4'-bis(4-nitrophenoxy) benzene, [BNPB, Figure 1, (1)] was synthesized by the reaction of hydroquinone (0.10 mol) and p-chloronitrobenzene (0.22 mol) in DMF (150 ml) in the presence of potassium carbonate (0.22 mol). The mixture was heated to 145–150°C under N_2 atmosphere, and then kept about 8–10 h. After cooled to the room temperature, the mixture was poured into the mixture of water/ethanol (1/1, v/v) and filtered to give solid product and then recrystallized from ethanol. Yield: 92%.

BNPB (0.10 mol), 1.50 g $FeCl_3{\cdot}6H_2O$, 1.50 g active carbon and 300 ml ethanol were introduced into a 1000 ml three-necked flask to which hydrazine hydrate (85 wt%, 60 ml) was added dropwise over a period of 1 h at reflux temperature, after the addition was complete, the reaction continued for about 5 h. The mixture was then filtered to remove the catalysts, after cooled to the room temperature; the product [Figure 1, (2)] was precipitated from the filter to obtain 1, 4'-bis(4-aminephenoxy) benzene (BAPB). Yield: 95 %.

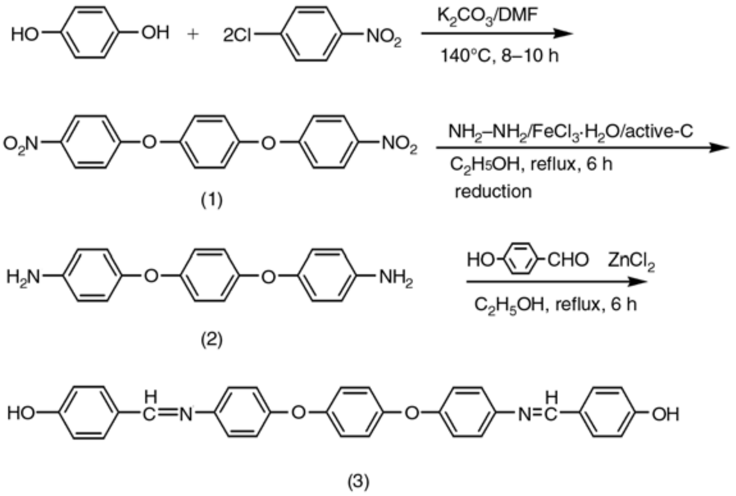

Figure 1. Synthesis routes of bisphenol BHPB. (1) 1, 4'-bis(4-nitrophenoxy)benzene (BNPB); (2) 1, 4'-bis(4-aminephenoxy)benzene (BAPB); (3) 1, 4'-bis{4-[(4-hydroxy)phenyliminomethylidene]phenoxy}benzene BHPB)

BAPB (0.10 mol), 4-hydroxybenzaldehyde (0.20 mol) and a catalytic amount of $ZnCl_2$ were dissolved in 300 ml of dry ethanol. The reaction mixture was stirred at reflux temperature for 6 h, and then was poured into water/ethanol (1/1, v/v). The product [BHPP, Figure 1, (3)] was collected by filtration and washed by deionized water and ethanol thoroughly. Yield: 97%, m.p. 278–280°C.

BHPB: IR (KBr, cm^{-1}): 3368 (Ar–OH), 1605 (HC=N), 1245 (Ar–O–Ar). ^1H NMR (500 MHz, ppm, DMSO-d_6): 10.10 (–OH), 8.47 (CH=N), 7.76, 7.78 (d, 4H), 7.26, 7.27 (d, 4H), 7.01, 7.08 (m 8H), 6.87–6.89 (d, 4H). ^{13}C NMR (500 MHz, ppm, DMSO-d_6): 116.20, 119.38, 110.16, 122.96, 128.08, 130.97, 147.81, 152.92, 155.41, 159.82, 161.06 (C=N). Elemental Analysis: $C_{32}H_{24}N_2O_4$ (500.55): Cal: C, 76.79%; H, 4.86%, N, 5.60%; Found: C, 76.64%; H, 4.98%, N, 5.63%. (The IR, NMR and Elemental Analysis data of BNPA and BAPB were omitted here for the sake of brevity.)

3.2. Preparation of epoxy thermosets

BAPB was mixed with DGEBA at an equivalent molar ratio, as BHPB could not dissolve into DGEBA very well. The hybrid curing agents BHPB/BAPB were prepared in various molar ratios (2, 1.5, 0.3 and 0.125, and denoted as B1, B2, B3 and B4, respectively), and then mixed with DGEBA at an equivalent molar ratio in DMF (weight ratio of sample/DMF is about 1:1) under 60°C, and then the mixture was vacuum dried at ambient temperature to obtain ternary systems. These samples were kept in the refrigerator (–10°C) for DSC test.

For preparing epoxy thermosets containing BHPB for *LOI* test, prepolymerization of samples is necessary. The procedure is as following: the sample was dissolved in a small quantity of DMF (weight ratio of sample/DMF is about 1:1), heated to 120°C under stirring. With the evaporation of DMF, the transparent sample was obtained. The thermosets for TGA measurement were prepared by curing the samples at 160°C for 1 h and 180°C for 2 h. Specimens for *LOI* test were obtained from the prepreg which needs pre-curing process (160°C/10 min), and then heat curing in a heat-press with the procedure of 130–160°C/0.5 h and 180°C/2 h for complete curing of the samples.

4. Results and Discussion

4.1. Synthesis

A novel bisphenol, 1, 4’-bis {4-[(4-hydroxy) phenyliminomethylidene] phenoxy} benzene (BHPB) containing rigid azomethine moiety (Ar–CH=N–Ar) and flexible aromatic ether linkage (Ar–O–Ar), was synthesized by the nucleophilic addition reaction of BAPB [Figure 1, (2)] with 4-hydroxybenzaldehyde in the presence of $ZnCl_2$ respectively. Figure 2 shows the ^1H NMR and ^{13}C NMR spectra of BHPB respectively (The IR and MS spectrum of BHPB is omitted for brevity). The chemical shifts of all protons and carbons have been labeled in Figure 2 clearly. The proton of CH=N in ^1H NMR is at 8.47 ppm, the chemical shift of Ar–OH shifts to lower field and is at 10.10 ppm due to introduction of azomethine moiety, and the carbon of CH=N in ^{13}C NMR is in 161.06 ppm. In the next, BHPB was used as a modifier for the BAPB/DGEBA system for improvement of the heat- and flame-resistance.

4.2. Curing behavior

The curing behavior of the ternary curing system containing BAPB, BHPB and DGEBA was studied by dynamic DSC method. As shown in Figure 3 curve *a*, the temperature at which the maximum conversion rate occurs in the DSC curve (T_p) of the BHPB/DGEBA system is about 213°C and higher than that of BAPB/DGEBA system (curve *f*, 184°C). This indicates that BHPB is difficult to react with oxirane group compared with BAPB. A small endothermic peak at about 275°C in curve *a* is found which is close to the melting point of BHPB. Moreover, curve *b* (the molar ratio of BHPB/BAPB is 2) exhibits no significant change compared with curve *a*. These indicate that more BHPB in the curing system may be not favorable for complete curing. When the molar ratios of BHPB/BAPB are 1.5 and 0.33 (curve *c* and *d*), two obvious exothermal peaks are found in their curves and the area of the first peak increases and their T_ps shift to higher temperature with increasing molar content of BAPB, while the endothermic peak around 275°C becomes smaller gradually, and no endothermic peak is found when the molar ratio of BHPB/BAPB is 0.125 (curve *e*). Although curves *d* and *e* are unsymmetrical, it can be seen that their T_ps are 154°C and 162°C for B3 and B4/DGEBA

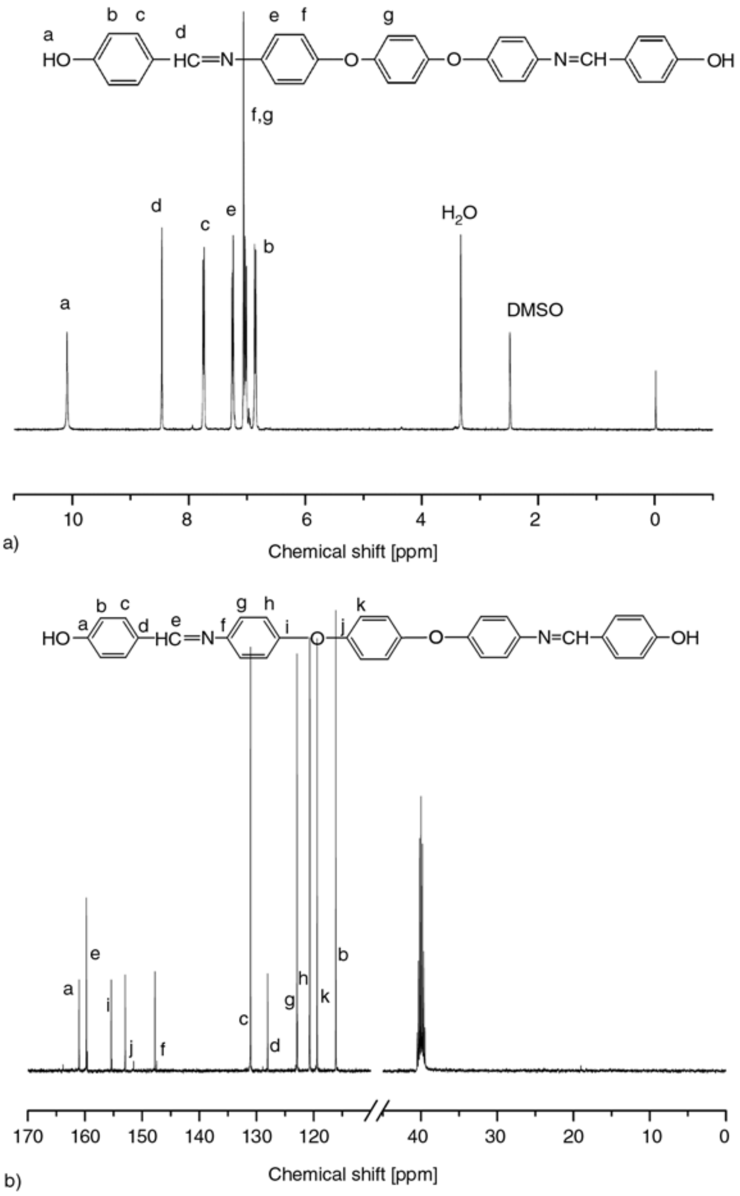

Figure 2. ^{1}H NMR (a) and ^{13}C NMR (b) spectra of BHPB

system respectively, which are obviously lower than those of BHPB/DGEBA system (213°C) and BAPB/DGEBA system (184°C). Thus, introduction of the suitable amounts of BHPB (BHPB/BAPB is about less than 0.33) into the BAPB/DGEBA system made the curing reaction of BAPB and DGEBA easier to occur.

4.3. Thermal stability and flame retardancy

The glass transition temperatures (T_gs) of all epoxy thermosets were measured by a second heating trace with DSC (Figure 4). These thermosets exhibit high T_gs in the range of 127°C to 160°C. The difference on T_g of the BAPB/DGEBA thermoset (160°C) and the BHPB/DGEBA thermoset (132°C) could be attributed to the reaction nature of amino and phenolic hydroxyl group towards oxirane group and molecular size of BHPB and BAPB [8, 9]. On the other hand, the chain segment between the crosslink points of the BHPB/DGEBA thermoset is longer on the average than those of the BAPB/DGEBA thermoset.

For the ternary thermosets (B1-B4/DGEBA), T_gs are in the range of 127–147°C and close to the T_g of the BHPB/DGEBA thermoset (132°C). Moreover, T_gs of these ternary thermosets are not all in the range of T_g of the BAPB/DGEBA thermoset and the BHPB/DGEBA thermoset as our original expectation. This reveals that BHPB with longer molecules may have more impact on the chain structure of the thermoset. Moreover, the non-sensitive relationship of T_gs towards the networking structure of these thermosets might stem from the imperfect curing technique because all samples were cured under the same conditions, which may not be the optimum condition for the realization of their potential effect.

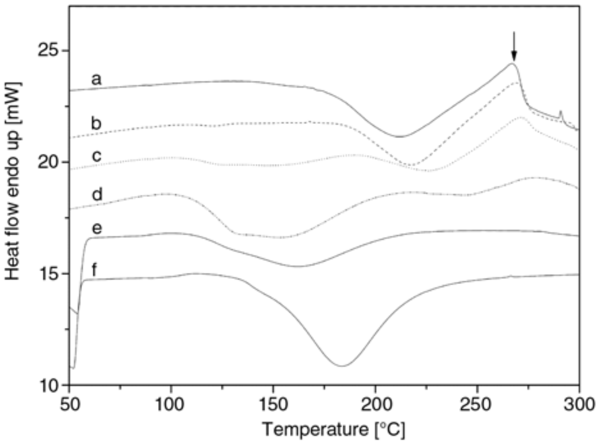

Figure 3. The DSC thermograms of DGEBA cured with a) BHPB; b) B1 (BHPB/BAPB = 2); c) B2 (BHPB/BAPB = 1.5), d) B3 (BHPB/BAPB = 0.33); e) B4 (BHPB/BAPB = 0.125) and f) BAPB under N_2 at a heating rate of 10°C/min

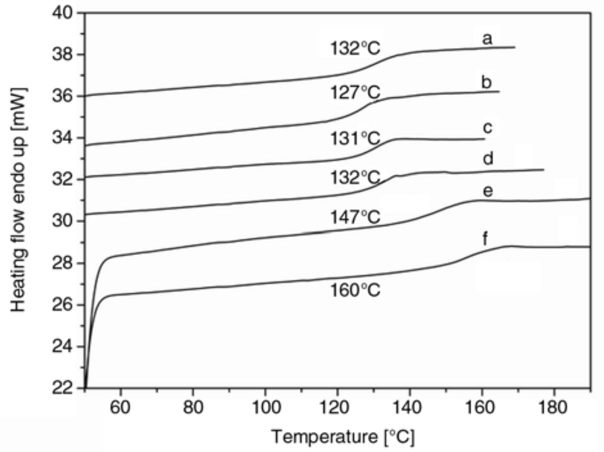

Figure 4. The T_g of BHPB/BAPB/DGEBA thermosets from a second DSC trace under N_2 at a heating rate of 20°C/min. a) BHPB/DGEBA; b) B1/DGEBA; c) B2/DGEBA; d) B3/DGEBA; e) B4/DGEBA and f) BAPB/DGEBA

Although BAPB and BHPB contain flexible aromatic ether bond, they still exhibit relatively high T_gs. So these epoxy thermosets containing azomethine moiety were potentially useful as advanced composite matrices because of high T_g as well as excellent thermal stability, which will be discussed in detail in the following.

Figure 5 shows the TGA thermograms of the BHPB/BAPB/DGEBA thermosets. The thermal parameters ($T_{d,5\%}$, and *IPDT*) of these ternary thermosets are listed in Table 1. It can be seen that the $T_{d,5\%}$ of these thermosets are all above 330°C and higher than that of DGEBA/dicyandiamide thermoset (about 290°C from our experiment). This

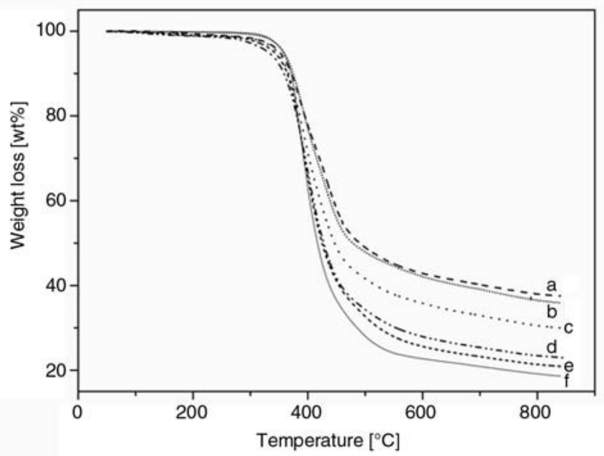

Figure 5. TGA thermograms of the ternary cured polymers, in N_2, 10°C/min. a) BHPB/DGEBA; b) B1/DGEBA; c) B2/DGEBA; d) B3/DGEBA; e) B4/DGEBA and f) BAPB/DGEBA

Table 1. Thermal stability parameters and *LOI* values of the epoxy thermosets

The epoxy thermosets	T_g [°C]	$T_{d,5\%}$[1] [°C]	Y_c% (850°C)	A^*	K^*	IPDT [°C][2]	LOI[3]
BAPB/DGEBA	160	357	18.61	0.574	1.347	662	26.0
B4/DGEBA	146	331	22.94	0.595	1.466	743	29.5
B3/DGEBA	130	350	27.70	0.634	1.734	919	31.0
B2/DGEBA	131	347	29.82	0.638	1.759	948	32.9
B1/DGEBA	127	357	35.90	0.681	2.138	1202	–
BHPB/DGEBA	132	350	37.54	0.686	2.181	1230	–

[1] 5 wt% decomposition temperature ($T_{d,5\%}$), indicates the apparent thermal stability of the epoxy thermosets;

[2] Integral procedure decomposition temperature (*IPDT*), proposed earlier by Doyle [13] can be discussed in a quantitative thermal analysis containing the char residue of the resulting thermosets at high temperature. From the TGA results, the *IPDT* is calculated by the following equation: $IPDT(°C) = A^*K^*(T_f - T_i) + T_i$, where A^* is the area ratio of total experimental curve divided by total TGA thermogram, K^* is the coefficient of A^*, T_i and T_f are the initial and final experimental temperature respectively;

[3] the B1/DGEBA and BHPB/DGEBA thermosets were not cured to that extent that the *LOI* measurement could be carried out.

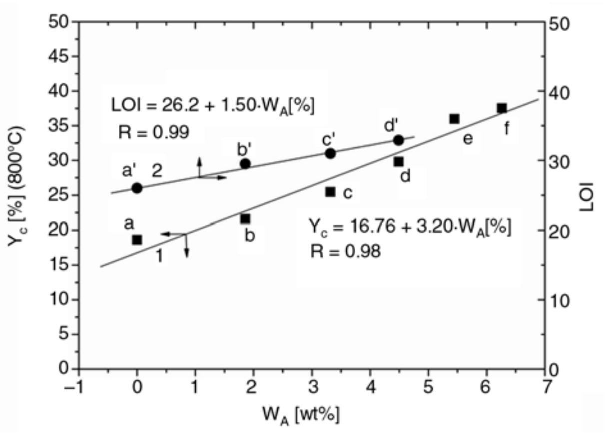

Figure 6. The relationship of char yield (Y_c) and content of azomethine in the BAPB/BHPB/DGEBA thermosets. Diamine: bisphenol = (a, a') 0:1; (b, b') 2; (c, c') 1.5; (d, d') 0.33; (e) 0.125 and (f) 1:0

indicates that they all have excellent thermal stability and can meet the requirement of 'lead-free' copper clad laminate ($T_{d,5\%} \geq 330$°C). The char yields (Y_c, wt%) of these thermosets increase with increasing molar content of BHPB for the introduction of azomethine moiety which had been proved to facilitate formation of char residue during decomposition [10, 11]. As shown in Figure 6, Y_c increases with increasing W_A (W_A, the weight percentage of azomethine in a sample) and exhibits good linearity ($R = 0.98$). According to Van Krevelen's theory [12], increase of the char formation will depress the flammability of the materials. Thus, it is rational to assess flame retardancy of these thermosets via char residue. The integral procedure decomposition temperatures (*IPDT*) of these thermosets increase dramatically with increasing molar content of BHPB from Table 1. This means that the inherent thermal stability of these thermosets was improved due to the introduction of azomethine moiety, which may be useful for improving the flame retardancy.

Limited oxygen index (*LOI*) measures the minimum oxygen concentration (in a flowing mixture of oxygen-nitrogen gas) required to support candle-like downward flame combustion [2]. A material with *LOI* of 26 or higher is rated as a flame-retardant material. It is strongly dependent on the char residue for halogen-free polymers [12] and is suitable as a semi-qualitative indicator of the effectiveness of the flame retardants in the laboratory. Herein, we found that *LOI* values (26.0–32.9) of these thermosets are beyond 26 and higher than that of the common epoxy thermoset (*LOI* of DGEBA/dicyandiamide thermoset is about 19.8) and increase linearly with increasing the content of azomethine moiety (Figure 6, line 2). This shows that the resultant thermosets were endowed with flame retardancy due to the introduction of azomethine moiety.

5. Conclusions

In summary, a novel bisphenol BHPB, which contains azomethine moiety and flexible aromatic ether linkage, was synthesized and introduced into the curing system composed of diglycidyl ether of biphenyl A (DGEBA) and diamine. The resultant epoxy thermosets containing BHPB had high thermal stability and good flame retardancy, and can be potentially applied in the electrical/electronic industries, especially can be used as the environment friendly 'green' materials.

References

[1] Wang C. S., Shieh J. Y.: Synthesis and properties of epoxy resins containing 2-(6-oxid-6H-dibenz‹c,e›‹1,2›oxaphosphorin-6-yl)1,4-benzenediol. Polymer, **39**, 5819–5826 (1998).

[2] Lu S. Y., Hamerton I.: Recent Developments in the chemistry of halogen-free flame retardant polymers. Progress in Polymer Science, **27**, 1661–1712 (2002).

[3] Zhang F., Zhang J., Wang Y. Modeling study on the combustion of intumescent fire-retardant polypropylene. Express Polymer Letters, **1**, 157–165 (2007).

[4] Toldy N., Tóth P. A., Marosi G. C.: Synthesis of phosphorus-based flame retardant systems and their use in an epoxy resin. Polymer Degradation and Stability, **91**, 585–592 (2006).

[5] Mormann W., Bröcher M., Schwarz P.: Mesogenic azomethine based diepoxides-monomers for the synthesis of 'liquid crystal' thermoset networks. Macromolecular Chemistry and Physics, **198**, 3615–3626 (1997).

[6] Castell P., Serra A., Galia M., Giamberini M., Carfagna C.: Anisotropic thermosets from liquid-crystalline azomethynic epoxy resins and primary aromatic diamines. Journal of Polymer Science Part A: Polymer Chemistry, **41**, 1–12 (2003).

[7] Mormann W., Bröcher M.: Liquid crystalline thermosets from triaromatic azomethine group containing diepoxides and 4,4'-methylenedianiline. Macromolecular Chemystry and Physics, **199**, 1935–1938 (1998).

[8] Myers G. E., Dagon J. R.: Distribution of molecular weight and of branching in high molecular weight polymers from bisphenol a and epichlorohydrin. Journal of Polymer Science Part A: Polymer Chemistry, **2**, 2631–2640 (1964).

[9] Zhang X. H., Chen S., Min Y. Q., Qi G. R.: Synthesis of novel bisphenol containing phthalazinone and azomethine moieties and thermal properties of cured diamine/bisphenol/DGEBA polymers. Polymer, **47**, 1785–1795 (2006).

[10] Mikroyannidis J. A.: Self-curing epoxy compounds. Journal of Applied Polymer Science, **41**, 2613–2624 (1990).

[11] Palaninathan K., Singaravelu R., Pachagounder S.: Synthesis and characterization of thermotropic liquid crystalline poly(azomethine ether)s. Polymer, **45**, 7895–7902 (2004).

[12] van Krevelen D. W.: Some basic aspects of flame resistance of polymeric materials. Polymer, **16**, 615–620 (1975).

[13] Doyle C. D.: Estimating thermal stability of experimental polymers by empirical thermogravimetric analysis. Analytical Chemistry, **33**, 77–79 (1961).